Nanociencias y Nanotecnología

Enhancement of Thermochromic and Electrochromic properties of MoO_3 and WO_3 thin films by RF and DC Reactive Magnetron Sputtering.

Tesis que presenta:

Michael Morales Luna

para obtener el grado de
Doctor en Ciencias
en la especialidad de
Nanociencias y Nanotecnología.

Director de Tesis: Dr. Sergio Armando Tomás Velázquez.

Dr. Jaime Santoyo Salazar.

Con mucho amor dedicada a:

- A mi bonita, mi amiga, mi pareja de vida
y mi esposa Otilia. Quien me apoya y cree en mi
todos los días.
- A mi mariposita Luhana
que me enseño a ir siempre por 5 mas.
- A mi abuelo Magdaleno
por enseñarme a ser pescador.

- ¿Y de qué te sirve? El ayuno,
por ejemplo, ¿para qué es útil?
- Es muy útil, señor. Cuando un hombre no tiene qu comer,
lo más inteligente será que ayune. Si, por ejemplo, Siddhartha
no hubiera aprendido a ayunar, ahora tendría que aceptar cualquier
empleo, en tu casa o en otra parte, pues el hambre lo impulsaría a ello.
Pero al ser como es, Siddhartha puede esperar tranquilamente, pues desconoce
la impaciencia y la necesidad; puede aguantar el asedio del hambre
largo tiempo, y encima reírse de él. Para eso, señor, sirve el ayuno.

Siddharta

Hermann Hesse

With too much love dedicated to:

- To my beautiful, my friend, my partner of life and my wife Otilia. Which supports and believe in me everyday.

- To my little butterfly Luhana which taught me to always go for 5 more.

- To my grandfather Magdaleno for teaching me to be a fisherman.

Acknowledgment

- To CINVESTAV, for the facilities that it gave me for do my PhD studies.

- To CONACyT, for the economic support that it offered to me to carry out my PhD studies.

- To my supervisors, Dr. Sergio Armando Tomás Velázquez and Dr. Jaime Santoyo Salazar, which are two researchers that I admire a lot and who always they have a word or comments that give encouragement and guidance, which always make you think beyond. Also for accepting me as student and taking the direction of my thesis, for his patience during all these years and for all his advices in the academic as well as in the personal. That without their help, I couldn't be finished this work. Sergio and Jaime thanks for all, for your time and for all your advices during these years.

- To my tutorial committee, Dr. Mauricio Ortega López, Dr. Miguel García Rocha, Dr. Orlando Zelaya Ángel and Dr. Jorge Aguilar Hernández, for the time that they dedicated each time I defended my thesis progress, as well as the time spent to the review of this thesis aside from their comments that were very helpful to improve the thesis work.

- To Claes Göran-Granqvist and Gunnar Niklasson, who were the professors

who gave me the opportunity to do my research studies in Upssala, from who I learned a lot about electrocromic materials. Thank's both professors for your patience and support during my staying.

- To Miguel Angel Arvizu Coyotzin, for giving me his sincere friendship since 2009. A friend that I owe a lot, for the academic part in the collaboration of diverse articles, in the participation of the different congresses, the help provided to be realize my staying research in Upssala and of course, in the many discussions and questions of physics that we had (always difficult to board and to answer). In the personal part he always have a hard opinion but correct. Thanks a lot for all, the funny and the bad moments. I appreciate a lot your friendship Arvizu.

- To Mario Pérez González, a great friend and partner whom I admire a lot for the great impetus that he has when he works in the laboratory, always ready to collaborate and always proposing new ideas which experiment with. Mario, good lucky with your PhD and I know that you'll have a lot of success in the future. Thanks for your help.

- To my senior father (Nicodemus Morales) for the wiser advices and unconditional help since I was a child, my beautiful mother (Luciana Luna) for all the cautions, la patient and love all these 32 years, to my sister (Lucia Morales) for those smiles that gives me every time when we see each other and for the beautiful times that I spent with her, talking about books and music and to my brother (Gesuri Morales) for all those talks about physics, politics, TV series and sports, thanks for all these lovely moments that make me a better person. Thanks family.

- To Manuel Escobedo and María del Rocío García, my parents-in-law for all the unconditional support extended to my wife and me over the years. Both always with very valuable advice and full of affection.

- To Azucena Moreno, a friend from who I thanks all the help offered me in Upssala, for orienting and guiding me in the city. Thanks for all those days with serious talks and those moments full of laughters, that made my stay more bearable.

- To my friends in Upssala Delphine, Carlos, Rodrigo, Rui-Tao, Umut, Ivar and the friends in México Vinicius, Gabriel, Matín, Jareth, Pedro y Horacio, that we made a very good academic group and with who also had laughs moments and besides I have learned a lot of things of each of them.

- To the Eng. Esther Ayala, Marcela Guerrero, Alejandra García Sotelo, for their technical support.

- To Alma and Jessica, for their secretarial support.

List of Abbreviations

EC	**E**lectro-**C**hromic
SM	**S**mart **M**aterilas
TMO	**T**ransition **M**etal **O**xide
CE	**C**oloration **E**fficiency
EPR	**E**lectron **P**aramagnetic **R**esonance
XPS	**X**-ray **P**hotoelectron **S**pectroscopy
XRD	**X**-**R**ay **D**iffraction
AFM	**A**tomic **F**orce **M**icroscopy
TEM	**T**ransmission **E**lectron **M**icroscopy
RBS	**R**utherford **B**ackscattering **S**pectroscopy
PVD	**P**hysical **V**apor **D**eposition
CVD	**C**hemical **V**apor **D**eposition
NIR	**N**ear **I**nfra-**R**ed
IR	**I**nfra **R**ed spectroscopy
APD	**A**valanche **P**hoto-**D**iode
CCD	**C**harge-**C**oupled **D**evice
SPM	**S**canning **P**robe **M**icroscopies

AES	**A**uger **E**lectron **S**pectroscopy
ESCA	**E**lectron **S**pectrocopy **C**hemical **A**nalysis
HRTEM	**H**igh-**R**esolution **T**ransmission **E**lectron **M**icroscopy
CV	**C**yclic **V**oltammetry
OCP	**O**pen **C**ircuit **P**otencial

Abstract

In the first half of this work, thermochromic molybdenum trioxide (MoO_3) thin films were deposited on glass substrates by rf reactive magnetron sputtering using a metallic molybdenum target. Thermochromism was induced by annealing the films in either argon or air at different temperatures within the range 25-300°C. Optical absorption spectra showed that the samples annealed in argon display a greater thermochromic response than the samples annealed in air. The annealing in argon at 300°C also revealed the formation of two coloration bands around 550 nm and 900 nm, which are associated with an oxygen vacancy defect state ($Mo^{5+}O_5$) and an intervalence charge transfer transition of a hexa-coordinated defect state ($Mo^{5+}O_6$), respectively. Characterizations performed by Raman spectroscopy, HR-TEM, and X-ray diffraction demonstrated that the films annealed in air predominantly exhibited the orthorhombic α-MoO_3 phase with small signs of the monoclinic β-MoO_3 phase, while the treatment in argon led to a mixture of β-MoO_3 and the Magneli phase Mo_9O_{26}. The influence of the annealing temperature on the Mo^{5+} oxidation state was analyzed by X-ray photoelectron spectroscopy (XPS). For the annealing in air, it was obtained that the Mo^{5+} signal of the Mo $3d_{3/2}$ peak increased slightly from 25 to 200°C but exhibited a steep decrease at 300°C. On the other hand, this signal showed a slight increase in the whole range for the anoxic thermal treatment. These results show that the Mo^{5+} oxidation state and the optical density display a similar

dependence on the annealing temperature, for both types of atmospheres.

In the second half of this work, the electrochromic (EC) property of tungsten-nickel-titanium oxide ($W_{1-x-y}Ni_xTi_yO_3$) thin films was investigated. These films were deposited on indium-tin oxide covered glass by dc reactive magnetron sputtering from tungsten, tungsten-titanium alloy and nickel targets. The focus of this study was on the durability and coloration efficiency (CE). Cyclic voltammetry was performed using 1 M $LiClO_4$ in propylene carbonate as electrolyte. The voltage window was chosen to induce fast degradation of the samples within 100 cycles. The best electrochromic response was found for samples of the type $W_{0.83-x}Ni_xTi_{0.17}O_3$. The explanation of this outcome is supported by results obtained by Rutherford Backscattering Spectroscopy (RBS) and X-Ray diffraction.

Resumen

En la primera mitad de este trabajo, las películas delgadas termocrómicas de trióxido de molibdeno (MoO_3) se depositaron sobre sustratos de vidrio mediante la técnica de pulverización catódica reactiva utilizando una blanco metálico de molibdeno. El termocromismo se indujo por un recocido de las películas en una atmósfera de argón o bien en presencia de aire a diferentes temperaturas en el rango de 25-300°C. Los espectros de absorción óptica mostraron que las muestras recocidas en argón muestran una mayor respuesta termocrómica que las muestras recocidas en aire. El recocido en argón a 300°C también reveló la formación de dos bandas de coloración alrededor de 550 nm y 900 nm, que están asociadas con un estado de defecto de vacancias de oxígeno ($Mo^{5+}O_5$) y una transición de transformación de la carga de intervalencia de un estado de defectos hexa-coordinado ($Mo^{5+}O_6$), respectivamente. Las caracterizaciones realizadas mediante espectroscopia Raman, HR-TEM y difraccin de rayos X demostraron que las películas recocidas en el aire presentaban predominantemente la fase ortorómbica α-MoO_3 con pequeños signos de la fase monoclínica β-MoO_3. Mientras que el tratamiento en argón condujo a una mezcla de la fase β-MoO_3 y la fase de Magneli Mo_9O_{26}. La influencia de la temperatura de recocido en el estado de oxidación Mo^{5+} se analizó mediante la espectroscopía de fotoelectrones de rayos X (XPS). Para el recocido en el aire, se obtuvo que la señal Mo^{5+} del pico Mo $3d_{3/2}$ aumentó ligeramente de 25 a 200°C pero exhibió una fuerte disminución a

300°C. Por otra parte, esta señal mostró un ligero aumento en todo el rango para el tratamiento térmico anóxico. Estos resultados muestran que el estado de oxidación Mo^{5+} y la densidad óptica muestran una dependencia similar de la temperatura de recocido, para ambos tipos de atmósferas.

En la segunda mitad de este trabajo, la propiedad electrocrómica (EC) del óxido de tungsteno-níquel-óxido de titanio ($W_{1-x-y}Ni_xTi_yO_3$). Estas tipo de películas se depositaron sobre vidrio cubierto de óxido de indio-estaño mediante también la técnica de pulverización catódica reactiva de blanco de tungsteno, de una aleación de tungsteno-titanio y de blancos de níquel. El objetivo de este estudio fue estudiar la durabilidad y la eficiencia de coloracin (CE). La voltamperometría cíclica se realizó usando 1 M $LiClO_4$ en carbonato de propileno como electrolito. La ventana de voltaje se eligió para inducir una degradación mas rápida de las muestras dentro de 100 ciclos. La mejor respuesta electrocrómica se encontró para las muestras del tipo $W_{0.83-x}Ni_xTi_{0.17}O_3$. La explicacin de este resultado es apoyada por los resultados obtenidos por Rutherford Backscattering Spectroscopy (RBS) y difraccin de rayos X.

Contents

List of Figures

List of Tables

1 Introduction

1.1 Importance of MoO_3 and WO_3

The world has been in a large and continuous scientific progress in the quest for a better quality of life. In medicine, efforts have been conducted to find appropriate treatments for high-risk diseases, such as several types of cancer, diabetes, and HIV/AIDS. In neurology, specialists have been able to construct brain mappings, defining the structure and function of the human brain. In biology, the discovery of DNA and RNA brought important information about the role played by these fundamental molecules. Without any doubt, one of the greatest remaining challenges in this area is the mapping of the human genome, which will help prevent and treat many diseases that affect humans nowadays. In chemistry and physics, the discovery of the impact of atmospheric pollutants in global phenomena, such as the stratospheric ozone depletion, was of the outmost importance. Similarly, several studies have shown that global warming is essentially caused by higher emissions of greenhouse gases, such as CO_2 and CH_4, produced mainly by countries as China, United States, and India [1]. Greenhouse gases are primarily due to the burning of fossil fuels like coal, petroleum, and natural gas intended for generating other types of energy. For instance, electricity is used for illumination purposes and to maintain comfortable temperatures in the automotive and aeronautic sectors, as well as in the building industry, *e.g.* houses, hospitals, and schools [2–4]. In the

coming years, global warming will be a serious problem for the entire population, which should encourage researchers to look for new ways of generating energy or to improve the efficient use of energy. On the one hand, there are now many studies focused on developing the power generation using renewable energy, including the use of bio-mass, geothermal energy, hydroelectric, wind energy, and solar energy, among others. In this case, one of the main disadvantages is that the practical implementation of these technologies will still take some years. With respect to the use of energy, is important to know that only three sectors are responsible for most energy consumption. Specifically, industry, transportation, and buildings consume 33%, 28%, and 39%, respectively [5]. The consumption of the building sector is mostly contributed by commercial (18%) and residential areas (21%) [6].

Numerous groups around the world investigate ways to reduce the energy consumption, since around 70% is lost in different stages [5]. Energy is greatly used to keep comfortable temperatures, either warm or cool. It is also used to maintain proper ventilation, which allows ideal indoor conditions. Several studies have shown that the major energy losses in this sector occur through windows, by energy transfer between the inside and outside of buildings [5]. A possible solution to reduce these losses is to modify the properties of the windows by modulating the transmittance of visible light or solar radiation by some special type of coating, *e.g.* inked films.

Ideally, a transparent window in warm climates should have a transmittance of 100% in the visible region, while this property should have a value of 38% to reduce the brigthness. On the other hand, it should present a transmittance of 0% for the NIR, thermal radiation, and UV regions. On the contrary, in the case of cold climates, it is necessary that the transmitance in the NIR and visible regions attain a value of 100%, while it could be 40% for the visible region to reduce the brigthness, and 0% for the thermal radiation and UV regions [1]. Fig. 1.1 shows the efficiency of materials to maintain pleasant temperature conditions in buildings as a function of the electrical energy consumption. As observed, the best material is the electrochromic one. It is therefore interesting to apply electrochromic materials

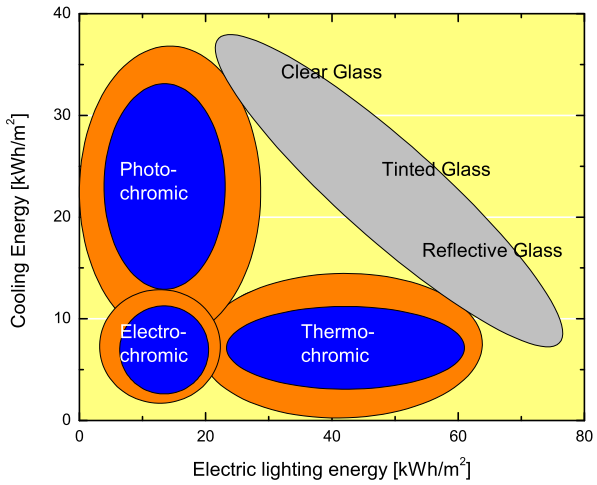

Figure 1.1: Relationship of cooling systems according to their energy consumption for different types of windows [5].

in windows with the goal of modifying their optical properties. These devices are called *smart windows* and are made of films commonly known as *smart materials* [5].

Great efforts have been conducted in the fields of Solid State Physics and Materials Sciences to investigate the properties of smart materials. It is believed that these compounds will play a very important role on sustainability and quality of life in the following years. Smart materials have a wider range of technological applications and a special type of use is called "*chromogenics*", which will be described in detail afterwards. These materials are used in areas such as the automotive industry, the manufacture of anti-reflective mirrors [7], and the fabrication of displays and storage devices [7, 8]. Other important fields of application are architecture and aeronautics [7, 8].

The *chromogenic materials* exhibit a reversible change of their optical properties, particularly the transmittance, reflectance, or absorbance, upon exposition to an external agent. Some authors also referred to them as *chamaleonic materials* [9].

The change in color has been attributed to the ability of these materials to form color centers [10]. These materials are mainly classified into four main categories: a) The *thermochromic* materials, which change color after being exposed to different temperatures [10]; they are used as thermal indicators, for instance, in faucets or in containers that display a different coloration when filled with either hot or cold liquids [7, 9]. b) The materials that change their color when excited optically are called *photochromic* [11]; they are mainly used in optical lenses, solar protection, windows, as well as in dosimetry and photography [9]. c) A third group is constituted by the *electrochromic* materials, which change their optical properties when a voltage is applied across them; these are predominantly used in screens and windows to control the solar reflectance and transmittance of visible-light [1, 5, 11, 12]. d) A fourth group is formed by materials that change their optical absorption when exposed to certain gases, specifically to the presence of hydrogen; these are called *gasochromic* materials [7, 9] and are used to detect high concentrations of hydrogen in buildings [7]. Other types of chromogenic materials include the *piezochromic*, *chemochromic*, *solvatochromic*, *hydrochromic* and *biochromic* [9]. Nevertheless, in general the first four chromogenic groups are the most interesting and the most extensively studied nowadays.

Many studies have been aimed at investigating the chromogenic properties described above. In particular, researchers have studied different compounds such as tungsten trioxide (WO_3), molybdenum trioxide (MoO_3), nikel oxide (NiO), titanium dioxide (TiO_2), and vanadium dioxide (VO_2) [5, 13–17]. These materials form part of the *transition metal oxides* (TMO), which is a group of predominantly ionic solids with outstanding physical and chemical properties that allow their use in numerous technological applications [18, 19]. Both WO_3 and MoO_3 are wide-band gap semiconductors that share a number of characteristics [20, 21]. For instance, both compounds display a perovskite-like structure (ReO_3)[i], where the metal atom, Re, shows an octahedral coordination. In other words, tungsten and molybdenum

[i]This structure is known as rhenium trioxide [19, 22].

are the elements that occupy the central region of the octahedra and are always surrounded by six quasi-equidistant oxygens atoms [12, 22]. There are different variants of this structure, with the difference essentially lying on the way the planes formed by the octahedra are stacked. One of these variants occurs when octahedra share their edges and vertices, while another configuration takes place when the octahedra only share their vertices [12, 19, 22]. These two types of configurations give rise to different structural phases, a property that will be discussed in more detail later.

As mentioned above, the chromogenic materials change their optical properties upon exposition to external agents. The optical changes are associated with the formation of a broad absorption band commonly referred to as the "*color band*" [10]. In the case of MoO_3, the color band is associated with an intrinsic property of the oxide since the value of the optical absorption coefficient is too high to be attributed to impurities in the material [10, 20]. The origin of this band has been related to different mechanisms, described within the framework of the following models: **(*i*)** *F centers model*. It was proposed by S. K. Deb to explain the coloration exhibited by molybdenum oxide when subjected to thermal treatments and light irradiation [23]. **(*ii*)** *Model of injection and extraction of electron-ion pairs*. Proposed by Faughnan, it explains the changes in coloration when a small voltage is applied across a material [24]. **(*iii*)** *Small-polaron absorption model*. It was proposed by Schirmer *et al.* to explain the electrochromism observed in tungsten trioxide [25]. At present, these are the most widely accepted models to explain the coloration induced in transition metal oxides. Other attempts to explain these phenomena have been reported elsewhere [22].

Several research groups around the world have focused on optimizing the chromogenic properties, particularly fabricating thin films for potential applications in display devices. For instance, one challenge is based on the fact that the maximum absorption in the coloration band of MoO_3 and WO_3 takes place around 1.56 and 1.4 eV, respectively [26], whereas the maximum absorption of the human eye is lo-

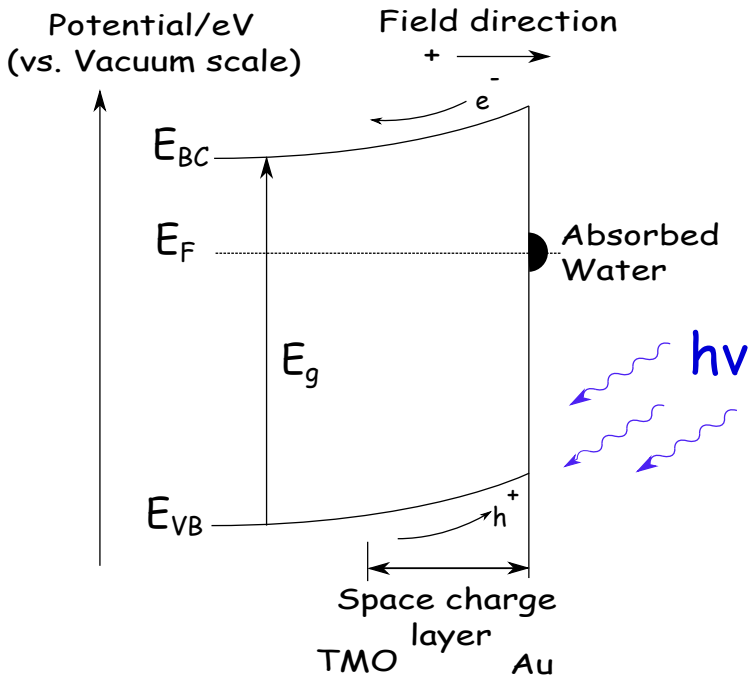

Figure 1.2: Scheme of a Schottky barrier and the process of charge transfer process at TMO/Au particles, where the TMO could be either WO_3 or MoO_3 [27].

cated around 2.25 *eV* [27]. Researchers thus look for a better overlapping between these parameters. In addition, different configurations have been reported, ranging from MoO_3 and WO_3 thin films [23–25] to hybrid configurations as MoO_3/WO_3 [26]. Other systems include heterostructures as Au/MoO_3, $Au/MoO_3/SnO_2$, and Pt/WO_3 [27–29]. In general, these works report an enhanced chromogenic response due to the formation of a *Schottky barrier* [22]. This barrier is formed at the interface between the metal and the semiconductor and facilitates the separation of the photogenerated electron-hole pairs, which produces a more efficient chromogenic material than the pristine film [27]. In Fig. 1.2, a diagram of the Schottky barrier is depicted. It is worth saying that the presence of Au and Pt on the surface of these semiconductors prevents photo-corrosion due to the Schottky barrier [27].

Other strategies have been developed to improve the chromogenic response. Particularly, in the case of molybdenum trioxide, the deposition of an intermediate II-VI semiconductor layer has been proven to be advantageous. For instance, cadmium

sulfide (CdS) has a smaller forbidden band-gap energy ($\sim 2.4\ eV$) than molybdenum trioxide. Therefore, in MoO_3/CdS systems, those photons that are not absorbed by the MoO_3 layer (photons with an energy $2.4\ eV < E < 3\ eV$) will pass through the MoO_3 layer, being absorbed by the CdS film. The electrons photogenerated in the CdS film could thus be injected into the MoO_3 matrix [30]. It motivated the study of new types of arrangements, including the preparation of MoO_3 thin films doped with zinc selenide (ZnSe), which has a forbidden band-gap energy of $2.7\ eV$ [14, 31]. This study showed that the insertion of ZnSe nanoparticles into the oxide matrix improves the chromogenic response of the reference sample (MoO_3). Another semiconductor that has been successfully implemented is Cadmium Selenide (CdSe), with a band-gap value of $\sim 1.7\ eV$ [31], in the MoO_3/CdSe/glass arrangement [20]. The accomplishment of these approaches will finally depend on the nature of the interlayer as well as on the interface between the II-VI semiconductor and the oxide [32]. As regards the growth of MoO_3 films, a number of techniques have been used for this purpose, *e.g.* thermal evaporation [10, 23], RF sputtering and reactive DC magnetron of Mo or MoO_3 targets [33–35], sol-gel technique [36, 37], spray pyrolysis [38], and electron beam evaporation [39], among others.

In the first part of this thesis, the deposition of MoO_3 thin films by reactive RF-sputtering technique, from a molybdenum target, is studied. The working pressure and the oxygen-argon concentration of the reactive atmosphere were varied in order to find the optimal conditions for the thermochromic response. The samples were then annealed at different temperatures between 25°C (room temperature) and 300°C, for 2 h, to know the maximum thermochromic response. The annealings were performed either in argon or under the presence of air. The characterization of these films involved the study of the optical properties and the analysis of the surface morphology and structural properties.

The second part of this thesis is devoted to the study of the electrochromic properties of transition metal oxides. Windows are of great importance from health and psychological points of view but, unfortunately, they are weak links in the use of

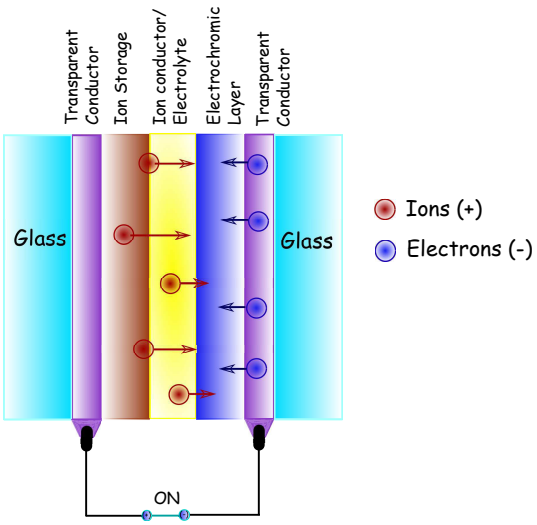

Figure 1.3: Scheme of an electrochromic smart window.

energy in buildings since they frequently let in or out energy in an uncontrolled way [5]. There are numerous ways to reduce this type of energy loss. One of the most promissory proposals involves the use of smart windows made with *electrochromic* (EC) materials. EC materials allow high modulation of the transmittance of light upon the application of a small potential difference [5, 12, 40]. An EC device is composed by several parts. It has a pure ion conductor (*electrolyte*) in the middle [12, 40, 41], which is sandwiched between two layers, one of them being the main EC thin film and the other an ion storage film that could have or not EC properties [8]. These two layers are deposited on transparent conductors where the voltage source is connected, and the entire system can be laminated between transparent glass or PET sheets [12, 42]. Among the transition metal oxides that exhibit electrochromic properties, amorphous tungsten oxide is by far the material with the best features. A scheme of a smart window is shown in Fig. 1.3.

Different deposition techniques as thermal evaporation [43, 44], sputtering [45–47], and sol-gel [48, 49], have been used to prepare EC WO_3 thin films. It is well known that WO_3 is a cathodic EC material, that is, it becomes coloured by charge insertion. An excellent choice as EC anodic storage film is nickel oxide

(NiO_x) [50–52]. NiO_x has been widely studied since the 1980's by different deposition methods [40, 53]. Recently, a number of studies have been devoted to investigate its compatibility with electrolytes used with WO_3, charge density exchange, durability, and coloration efficiency [15, 54, 55]. In particular, composites of WO_3 and NiO produced interesting results regarding their optical, structural and electrochromic properties [56, 57].

Three features are essential for smart windows technology: **(*i*)** A shorter *response time* between coloured and bleached state, **(*ii*)** a high *coloration efficiency* CE of the films and **(*iii*)** a *long-term durability* during color/bleach cycling of EC materials. An enhanced coloration efficiency has been proven in W-Ni oxides [57]. With regard to the third aspect, a good option to increase the life-time of the EC films is the addition of a certain concentration of titanium oxide (TiO_2) into the WO_3 film [58–62]. A recent study showed that the doping of WO_3 films with Ti enhances the durability even when extended voltage spans are used [13]. Other works have reported structural changes during the electrochromic testing of WO_3 films. This crystallization is mainly attributed to the degradation of tungsten oxide after lithium (Li^+) intercalation [63–65].

In the second part of this thesis it was a part of a research in Uppsala University. The principal objective of this research is to show the effects of Ti and Ni added into the WO_3 matrix. This study is focused on the coloration efficiency and the durability of EC films under harsh conditions obtained by applying a wide voltage window to accomplish electrochemical charge insertion/extraction. The thin film preparation of W oxide, W-Ni oxide and W-Ni-Ti oxide were made by reactive DC magnetron sputtering. The targets were of W, Ti and Ni with these features: W(95wt%) + Ti(5wt%) and W(90wt%) + Ti(10wt%), the Ni and W targets. Argon and oxygen gases were introduced through mass-flow controller gas inlets. The O_2/Ar ratio was set to 0.15. To obtain different concentration of W-Ni-Ti oxide, the discharge power of the targets were changed but maintaining the next relation $P_{W-Ti} + P_{Ni} = 230$ W. For studying electrochemical and optical properties, the

films were deposited onto unheated 5 × 5 cm^2 glass plates coated with transparent and electrically conducting layer of In_2O_3:Sn (ITO). Glassy carbon substrates were used for Rutherford Backscattering Spectrometry (RBS) analysis. RBS data were fitted to a model of a film-substrate system by the use of the SIMNRA program that will be explain later in the thesis. Optical transmittance was recorded in-situ during electrochemical cycling in the 400-800 nm wavelength range using optical fibers and an Ocean Optics system. Film thicknesses were measured by surface profilometry obtaining thickness around 300 nm.

Objectives

- To investigate the thermochromic properties of MoO_3 thin films deposited by rf reactive magnetron sputtering. The varied parameters include the working pressure and the ratio O_2/Ar of the reactive atmosphere in order to find the optimum thermochromic response. Thermochromism is induced by exposing the samples at different annealing temperatures and different types of atmosphere.
- To enhance the durability and coloration efficiency of electrochromic WO_3 thin films, deposited by dc reactive magnetron sputtering, by doping with titanium and nickel. The improved system is $W_{1-x-y}Ni_xTi_yO_3$.

2

Theoretical Models

To explain the theoretical models that describe the chromogenic phenomenon is necessary to portray first the crystal structure of these materials. There exist very interesting natural minerals whose properties are closely related to the materials studied in this work. These minerals show a perovskite crystal structure[i]. The composition of this structure is in general $CMeO_3$ [67], where C and Me are cations and O is the anion (usually oxygen). The ideal cubic-symmetry structure has the Me cation in 6-fold coordination, surrounded by an octahedron of anions, and the Ce cation in 12-fold coordination. Typically, Me is related to a 3d, 4d, or 5d transition metal, *e.g.* molybdenum (Mo), tungsten (W), or titanium (Ti) [68]. Metal oxides with chromogenic properties show a perovskite-like structure, whose main characteristic is the absence of the central atom C, as shown in Fig. 2.1. The metal ions occupy the corners of a primitive unit cell, while the O anions are located at mid-edges.

Molybdenum trioxide and tungsten trioxide show actually two types of crystal phases, with unit cells forming quasi-regular octahedra. The specific arrangement of these octahedra is the main difference between both phases. In the thermodynamically stable α phase, or orthorhombic structure, a layer of corner-sharing octahedra is followed by another similar layer in a way that the octahedra of subsequent layers

[i]Named in honor of the Russian mineralogist Count Perovski [66].

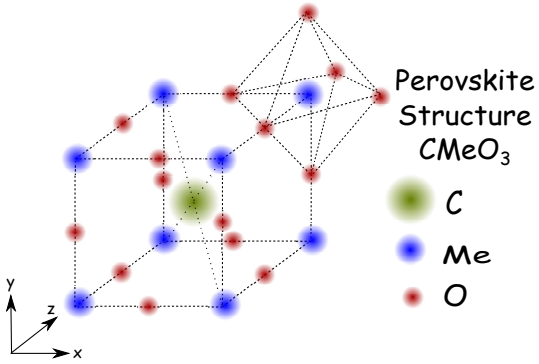

Figure 2.1: Structure of a perovskite emphasizing the octahedral symmetry.

share edges, as depicted in Fig. 2.2(a). These layers are bound by van der Waals forces [68]. As shown in 2.2(b), in the metastable β phase, or monoclinic structure, the layers consist of octahedra that only share vertices [22, 68]. Fig. 2.2(c) illustrates the unit cell. The latter arrangement gives rise to tunnels that serve as conduits for *ion-intercalation* [68]. Due to this peculiarity, it is said that amorphous films, deviated from the perovskite-like structure, present better chromogenic properties than deviations from the orthorhombic phase [14, 33].

The chromogenic properties have been explained by different mechanisms, although the most widely accepted theoretical models are: **(*i*)** *F-color centers model.* **(*ii*)** *Model of injection and extraction of electron-ion pairs.* **(*iii*)** *Small-polaron absorption model.* These models are described in the following sections.

2.1 Formation of F-color centers

Hägg and Magneli are considered the pioneers in the study of the crystalline phases of tungsten and molybdenum oxides. They characterized these materials mainly by X-ray diffraction and discovered different substoichiometric structures of the type ReO_{3-x}, where $0 < x < 1$, and Re represents the metallic element (Mo or W) [69]. Many systems show the so-called Magneli phases Re_mO_{3m-1} y Re_mO_{3m-2} ($m = 1, 2, \ldots$). Some of these phases possess metallic properties [70]. The non-

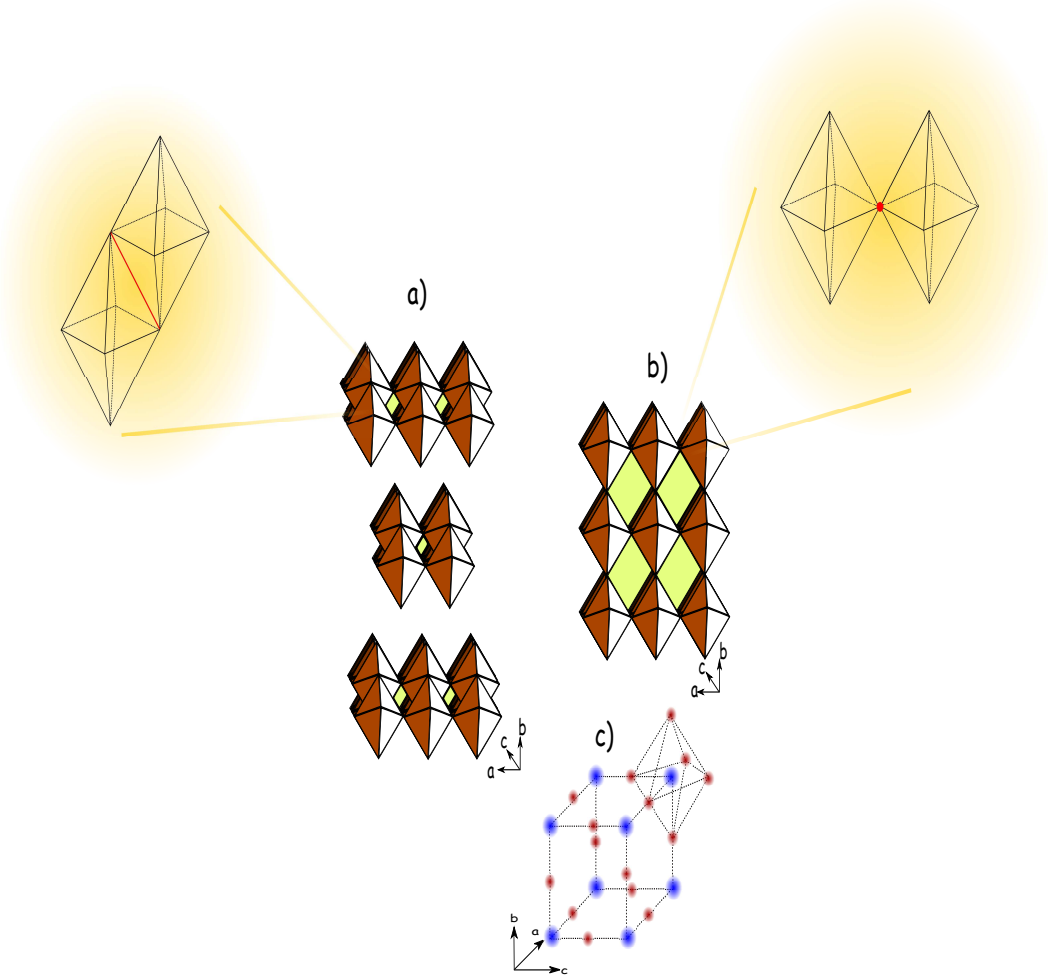

Figure 2.2: Crystal structure of molybdenum trioxide: a) α phase, b) β phase and c) unit cell of MoO_3 [22].

stoichiometric characteristic is usually associated with the formation of oxygen vacancies, which gives rise to the generation of color centers [10]. In the case of MoO_3 thin films, this material has the fundamental absorption edge slightly below 400 nm. When the films are irradiated with ultraviolet (UV) radiation, with wavelength lower than 330 nm ($\sim 3.8\ eV$), their coloration turns blue. Accordingly, the absorption spectrum changes its shape, producing a wide absorption band that extends from 500 nm to the near infrared region, known as the *coloration band*. Some authors have claimed that this band is composed by discrete absorption bands. For instance, Deb found three peaks centered at 500, 625, and 850 nm [23]. The overlap of these peaks leads to the asymmetry of the coloration band [10, 23, 71]. Deb also observed that the exposition of these materials to UV light changed the slope of the fundamental absorption edge [23]. Specifically, the absorbance increases for $\lambda > 390$ nm, whereas a decrease is noted for $\lambda < 390$ nm. Since the optical absorption coefficient becomes very high ($\alpha = 10^5 \mathrm{cm}^{-1}$), the induced coloration cannot be attributed to impurities in the material [10, 23]. Deb and Chopoorian later suggested that the change in color must be due to the formation of F-color centers[ii]. In MoO_3 films with no treatment, the optical absorption is due to the formation of excitons localized in the vicinity of defects, similarly to the coloration mechanism of the α band in the alkali halides. On the other hand, when the material is irradiated, its absorption edge is modified, in correspondence with a color change. In this case, the coloration band is similar to the β band of the alkali halides. The coloration mechanism is therefore associated with the formation of color centers [23].

Robert W. Pohl and Alexander Smakula were the first to study the photocoloration of alkali halides in the 1920's, but Jan Hendrik de Boer was the first to propose a theoretical model a few years later. This model assumes that the F-color center is a system consisting of a highly-localized electron bound to an anionic vacancy. A schematic representation of this model is illustrated in Fig. 2.3. This model assumes that the binding energy of the electron is greater than the thermal

[ii] From the german word, farbenzentrum, which means color center.

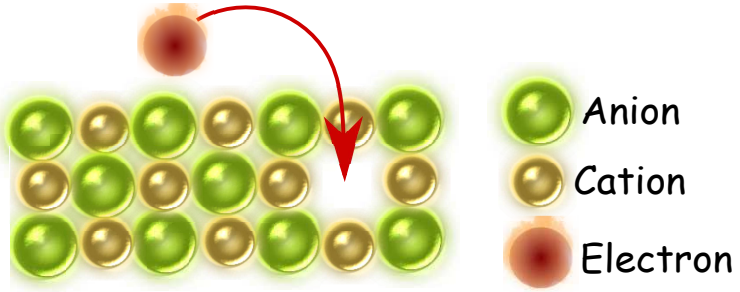

Figure 2.3: Schematic representation of the formation of F-color centers.

energy kT. Thus, the F-absorption band is associated with the excitation of an electron in the F center, from the ground state to the first excited state. The coloration of alkali halides is a reversible process, *i.e.*, it can go from the colored to the bleached state by removing the excitation source. In the case of MoO_3, reversibility is obtained by re-irradiating the sample with light corresponding to the maximum of the coloration band, which is located between the visible and near infrared regions [20, 21].

It is considered that oxygen vacancies play the role of F-color centers in the photochromic and electrochromic coloration of MoO_3 and WO_3. This statement is supported by electron paramagnetic resonance (EPR) measurements on freshly deposited MoO_3 and WO_3 films that confirm the formation of the Mo^{5+} and W^{5+} oxidation states, respectively. The density of these states increases after UV irradiation or ion intercalation [10, 72]. It is important to remark that this feature also occurs when molybdenum and tungsten bronzes are formed, which is a necessary element in the formulation of the intervalence-charge transfer and polaron absorption models, to be described later.

MoO_3 shows a resistance to bleaching because the first excited state of the F-color center is well below the conduction band, which in turn is $\gg kT$. Hence, the thermal energy of the lattice at room temperature is not enough to promote electrons to the conduction band [10]. However, when the films are thermally treated in the presence of oxygen, they can be bleached almost completely when the tem-

perature reaches $300°C$. When exposed to these conditions, the films lose all ability to be re-coloured, even under the application of other external agents. Bleaching is mainly attributed to the replenishment of oxygen vacancies, with the material recovering stoichiometry. In addition, the material shows a higher density of crystalline domains. Accordingly, samples annealed in inert atmospheres do not become bleach.

The induced coloration in MoO_3 thin films can be quantified by the Smakula's equation [73, 74]. R. Smakula proposed that the F-centers in alkali halides can be viewed as oscillating electrons. Classically, the oscillator strength f_α is the number of electrons per atom oscillating at the frequency ω_α. In the case of quantum mechanics, the oscillator strength, f_{ab}, is dimensionless and expresses the transition amplitude between the states $|a\rangle$ and $|b\rangle$, with energies E_a and E_b, respectively. Considering the electron effective mass m^* and defining $\omega_{ab} \equiv (E_a - E_b)/\hbar$, with $\hbar$ the reduced Planck constant, the oscillator strength is described by the expression:

$$f_{ab} = \frac{2m^*}{3\hbar}\,\omega_{ab}\,|\langle a|x|b\rangle|^2\,. \tag{2.1.1}$$

Smakula found a semi-empirical relation between the density of F-color centers, N_F $[cm^{-3}]$, and the absorption coefficient at the maximum of the F-band, α_{max}, expressed as follows:

$$N_F \approx 1.3 \times 10^{16} \alpha_{max} W_{\mathrm{FWHM}} \tag{2.1.2}$$

where W_{FWHM} $[eV]$ is the full width at half maximum of the F-band, considered as a Gaussian function [21].

Other authors, *e.g.*, Dexter [75] and Melvin [76], expressed Smakula's equation as:

$$N_F f_{ab} \approx \frac{m^* c}{2\pi^2 e^2 \hbar} \frac{n}{(n^2+2)^2} \alpha_{max} W_{ab}$$
$$\approx (0.87 \times 10^{17} eV^{-1} cm^{-2}) \frac{n}{(n^2+2)^2} \alpha_{max} W_{ab} \quad (2.1.3)$$

where c and e are fundamental physical constants and n is the refractive index of the film before modifying its optical density.

A rapid calculation of the density of color centers can be done by considering an optical density equal to 0.23 at a wavelength of 850 nm in a sample 80 nm thick. This gives a value of $\alpha \approx 0.063$. Now, if W_{ab} is equal to 1 eV for a refractive index equal to 2, the product $N_F f_{ab}$ is approximately equal to 3×10^{14} color centers per cm^3. In the case of the alkali halides, the value for f is 0.5, so that the density of color centers is 6×10^{14} per cm^3 [71]. Unfortunately, there is no reliable way to measure N_F independently. A relative estimate can be done for the product $N_F f_{ab}$, with a reported value close to 10^{19} cm^{-3} [10, 23].

It should be mentioned that the alkali halides not only change their coloration because of the presence of F-color centers. There exist other types of color centers with more complex nature. In these cases, electrons may be trapped by two or more neighboring anionic vacancies. For instance, the M- and R-color centers are formed by electrons bound to two and three anionic vacancies, respectively. These color centers are depicted in Fig. 2.4 [77–79]. It has been claimed that these complex color centers are associated with different types of absorption bands, as observed in the absorption spectrum of chromogenic MoO_3 and WO_3 [80–82].

Finally, it has been observed that the electrical conductivity of MoO_3 films increases upon exposition to irradiations and thermal treatments. This phenomenon has been explained in terms of the mobility of electrons promoted from the defect band to the conduction band. The gap between these bands is ~ 0.56 eV [10].

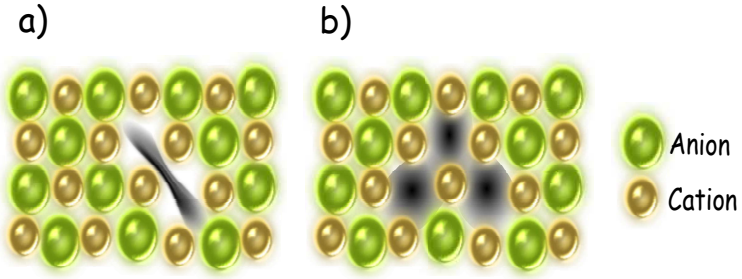

Figure 2.4: Schematic representation of different color centers (a) M-center (b) R-center.

2.2 Injection and extraction of electron-ion pairs

The F-color centers model has been used to explain all kinds of chromogenic phenomena; however, this model fails to describe electrochromism convincingly. In the 1970's, Faughnan, Crandall, and Heyman realized that the supporting evidence for the formation of F absorption bands in metal oxides was scarce, as compared to the existing documentation in alkali halides. For instance, the density of color centers in WO_3 thin films is very high ($\sim 10^{22}$ color centers per cm^3) to be related to oxygen vacancies [24, 83].

Faughnan *et al.* proposed a model based on the formation of *tungsten bronzes*, expressed as M_xWO_3, where M denotes H, Li, Na, or K, and $0 < x < 1$. Bronzes are produced by the intercalation of alkali ions and compensating electrons in the WO_3 lattice [12]. The formation of color centers is associated with the trapping of electrons by W^{6+} ions, producing W^{5+} states, as confirmed experimentally by X-ray photoelectron spectroscopy (XPS) [84]. Faughnan *et al.* claimed that these experimental results could be explained in terms of the intervalence charge transfer theory, understood as an optical transition that involves the transfer of an electron between two adjacent W^{5+} and W^{6+} states. Donors and acceptors in these transitions are weakly interacting metallic ions with various oxidation states [85, 86]. The classification of these systems considers different aspects, such as: ***(i)*** the *oxidation number difference* (ΔZ) between both ions, ***(ii)*** the *presence or absence* of bonds or bridges between ions, and ***(iii)*** the *similarity or dissimilarity* between the nuclei

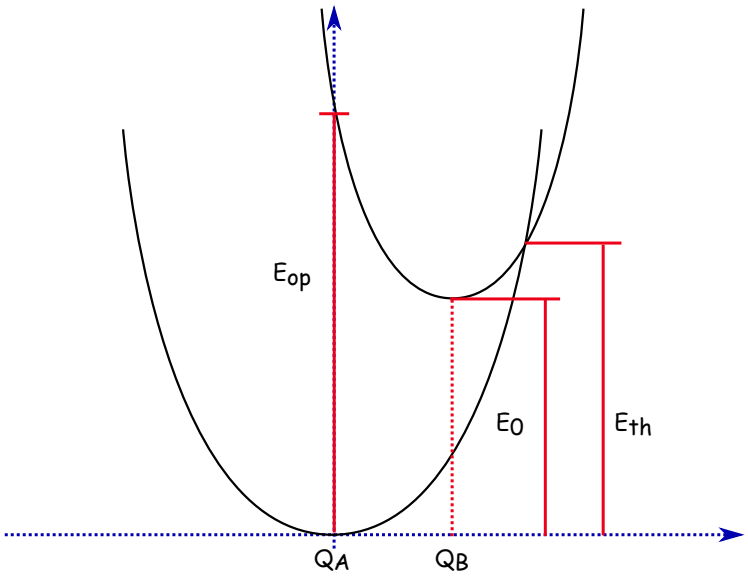

Figure 2.5: Energy diagram as a function of configuration coordinates corresponding to an intervalence charge transfer [24].

[85]. A representation of two electronic states located in the configuration sites A (W^{6+}) and B (W^{5+}) is exhibited in Fig. 2.5. Here, E_{op} is the energy at the maximum of the optical absorption band, E_{th} is the thermal activation energy needed by an electron to move from site A to site B, E_0 is the energy difference between the A and B base states, and Q_A and Q_B are the configuration coordinates of electrons at sites A and B, respectively. Using this information, Hush [86] showed the following relation:

$$E_{th} = \frac{E_{op}^2}{4(E_{op} - E_0)} \tag{2.2.1}$$

For identical sites, this relation takes the form $E_{th} = (1/4)\ E_{op}$ [24].

A detailed analysis of the absorption spectrum based on the theory of moments provides a relation between the absorption bandwidth W_{FWHM} and E_{op}. In the limit of high temperatures, the absorption band can be approximated to a Gaussian distribution, obtaining

$$W^2_{\mathrm{FWHM}} = (16kT\ln(2))(E_{op} - E_0) \approx \frac{E_{op} - E_0}{1.8} \tag{2.2.2}$$

Here, a temperature of $T = 300°\mathrm{C}$ was considered. In obtaining this expression, it was assumed that temperature is the only parameter influencing band broadening; however, it is well known that disorder in amorphous materials contributes to enhance the band broadening effect.

As a result of the optical intervalence charge transfer, the sites A and B exchange their valence states with a subsequent inversion of the electronic energy diagram, releasing the excess energy as heat [24, 87]:

$$W_A^{6+} + W_B^{5+} + h\nu_{visible} \rightarrow W_A^{5+} + W_B^{6+} + heat \tag{2.2.3}$$

Gabrusenoks *et. al* studied electrochromic WO_3 films intercalated with protons H^+ and used the intervalence charge transfer model to fit the experimental data. Unfortunately, a good agreement between the theoretical expression and the experimental data was only obtained at low energies [88] .

Although the intervalence charge transfer model was proposed to explain the electrochromic effect, it can be adapted to describe the photochromic and thermochromic properties of MoO_3 and WO_3. In these cases, neither ions are injected from an electrolyte nor compensating electrons are supplied by a transparent conductor film. Nevertheless, the formation of bronzes can still be explained by the presence of protons, H^+, obtained from H_2O molecules adsorbed on the films [22]. The model is described as follows: **(*i*)** Electron-hole pairs are photogenerated upon exposition of MoO_3 to UV irradiation, Eq. 2.2.4; the energy of the incident photon $h\nu$ must be greater than the forbidden bandgap energy E_g of the metallic oxide. **(*ii*)** Holes react with water molecules adsorbed on the film surface, producing protons and oxygen; oxygen is released to the atmosphere, Eq. 2.2.5. **(*iii*)** Protons and electrons react with MoO_3 to form hydrogen-molybdenum bronze, Eq. 2.2.6 [89]. The formation of Mo^{5+} states has been proved by XPS measurements [11, 90, 91]. **(*iv*)** Absorption of visible light gives rise to intervalence charge transfer between the

newly-formed Mo^{5+} (valence-band type) and Mo^{6+} (conduction-band type) ions, Eq. 2.2.7. ***(v)*** The model also considers adverse effects to photochromism, such as the recombination of electron-hole pairs, Eq. 2.2.8, ***(vi)*** the photo-corrosion of MoO_3, Eq. 2.2.9, and ***(vii)*** the generation of hydrogen, which is released to the atmosphere, Eq. 2.2.10 [91]. In this model, the thermochromic film bleaching can be explained as the recovery of the oxygen lost in Eq. 2.2.5.

$$\mathrm{MoO_3} + h\nu_{(\mathrm{UV})} \rightarrow e^- + h^+ \tag{2.2.4}$$

$$4h^+ + 2H_2O \rightarrow 4\mathrm{MoO_3} + 4\mathrm{H^+O_2} \uparrow \tag{2.2.5}$$

$$\mathrm{MoO_3} + x\mathrm{H^+} + xe^- \rightarrow \mathrm{H}_x\mathrm{Mo}_x^{5+}\mathrm{Mo}_{1-x}^{+6}\mathrm{O_3} \tag{2.2.6}$$

$$\mathrm{Mo}_A^{6+} + \mathrm{Mo}_B^{5+} + h\nu_{(\mathrm{visible})} \rightarrow \mathrm{Mo}_A^{5+} + \mathrm{Mo}_B^{6+} + \mathrm{heat} \tag{2.2.7}$$

$$h^+ + e^- \rightarrow \mathrm{MoO_3} + \mathrm{heat} \tag{2.2.8}$$

$$2\mathrm{MoO_3} + 4h^+ + 4\mathrm{H_2O} \rightarrow 2\mathrm{MoO}_4^{2-} + 8\mathrm{H^+} + \mathrm{O_2} \uparrow \tag{2.2.9}$$

$$2\mathrm{H^+} + 2e^- \rightarrow \mathrm{H_2} \uparrow \tag{2.2.10}$$

2.3 Small-polaron absorption model

The model described in the previous section resembles the small-polaron model to be described here. The difference lies mainly on the structural distortion caused by localized electrons and the formation of W^{5+} (or Mo^{5+}) oxidation states.

The idea that an F-color center could be modeled as a free electron trapped in a polar crystal was made by L. D. Landau in 1933 [92]. Although this idea does not explain the formation of the F-color center, it does reveal the concept of a polaron. A polaron is defined as a quasi-particle consisting of an electron and an associated deformation field. An electron moving slowly in a crystal can distort the lattice by interacting with the nearby atoms or ions. This deformation follows the electron movement through the lattice, generating in this way the polaron[iii].

[iii]H. J. Lipkin defines a polaron as an electron that creates a potential around itself, polarizing

Although polarons are found in several materials, they are mainly observed in ionic or highly polar crystals, where the Coulomb interaction between a conduction electron and the lattice ions is large.

Polarons can also be conceived as formed by a conduction electron interacting with a cloud of virtual phonons. As a result, the effective mass of the electron increases, with a consequent decreased mobility. The mobility of polarons is thus different from that of electrons. H. Fröhlich reported extensive works on the properties of polarons. This author considered polarons as an electron-phonon coupling, a central idea of the theory of superconductivity [79].

Polarons are often classified as large or small polarons. When an electron moves freely through the lattice, it is accompanied by an electrostatic field, causing the electron to have an effective mass slightly greater than the free-electron mass. It is referred to as a large polaron[iv]. In the case of small polarons[v], the associated electron is highly localized. At high temperatures, the electron moves from one place of the lattice to another by thermal activation. At low temperatures, the electron will appear as having a large effective mass [77].

In the case of amorphous MoO_3 (WO_3), not all the Mo^{6+} (W^{6+}) sites have the same energy. Therefore, conduction electrons are first trapped in sites with lower energy, polarizing the lattice and forming small polarons. After ion intercalation, molybdenum (or tungsten) bronze is formed, with Mo^{5+} (W^{5+}) becoming the natural trapping sites of the lattice.

Optical absorption in these oxides can be explained by using the small-polaron model [12]. Here, the potential energy of an electron-lattice system is considered in 1D configuration coordinates. Fig. 2.6 depicts this model, where the parabola represents the potential energy as a function of the coordinate Q connecting the sites i and j, U is the energy gained after the lattice polarization, and ϵ represents the energy difference between the mentioned sites. The optical transition is indicated

the lattice by repelling negative ions and attracting positive ions [93].

[iv] Sometimes also called Fröhlich polaron.

[v] Usually called Holstein polaron.

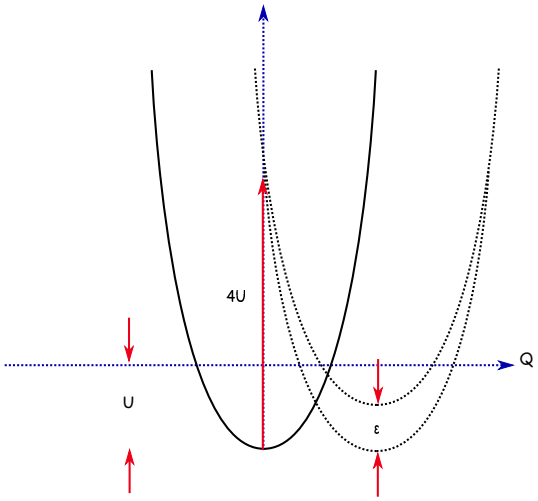

Figure 2.6: Potential energy of an electron-lattice system as a function of the configuration coordinate Q connecting the lattice sites i and j [20].

by the red thick arrow, in agreement with the Franck-Condon principle [12].

The description of this double-well system involves electronic transitions whose energy difference coincides with the photon energy. The relative intensity of these transitions obeys a Poisson distribution, although Gaussian distributions can be considered for strong electron-phonon interactions. The optical absorption coefficient is expressed as:

$$\alpha(\hbar\omega) \propto \hbar\omega g^{1/2} \exp(-g(\hbar\omega - \epsilon - 4U)^2) \tag{2.3.1}$$

where g is inversely proportional to the energy U, namely, $g^{-1} = 8U\hbar\omega_0$, with $\hbar\omega_0$ standing for the photon energy [25, 94].

In 1977, Schirmer *et al.* were the first researchers to explain the electrochromic phenomenon of WO_3 by fitting Eq. 2.3.1 to experimental data. They obtained good results only for the spectral region of low energies. The discrepancy between theory and experiment at high energies was attributed to electronic transitions to higher-energy orbitals [25].

It is important to remark that the small-polaron model is commonly used to describe the coloration mechanism in highly-disordered oxides, *e.g.*, the β-phase

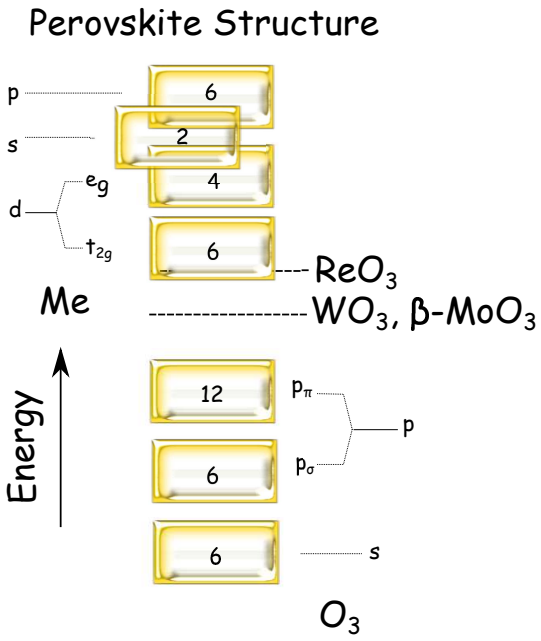

Figure 2.7: Band structure for the perovskite structural defect of MeO_3 [67].

of MoO_3 [67]. Granqvist *et al.* proposed an energy-level diagram to explain this phenomenon in MoO_3 and WO_3, as illustrated in Fig. 2.7 [12, 67, 68].

The energy-level diagram takes into account the electronic structure of molybdenum and tungsten oxides. On the one side, molybdenum and tungsten have electronic configurations given by Mo: [Kr] $4d^5$ $5s^1$ and W: [Xe] $4f^{14}$ $5d^4$ $6s^2$, respectively. On the other side, the electronic configuration of oxygen is O: $1s^2$ $2s^2$ $2p^4$. It is observed that oxygen only needs two electrons to complete its octet, which can be accomplished by obtaining one electron from each of the two Mo, or W, atoms that flank them in a rhenium oxide structure. In addition, Mo and W atoms give 6 valence electrons, one to each oxygen at the octahedron corners, to remain with a complete octet.

For a better understanding of the energy-level diagram, it is important to describe its orbitals. As shown in Fig. 2.8, the structure of *p*-orbitals resembles the shape of a peanut, with two lobes pointing in opposite directions from each other. The three *p*-orbitals in each shell are oriented at right angles to each other. It results

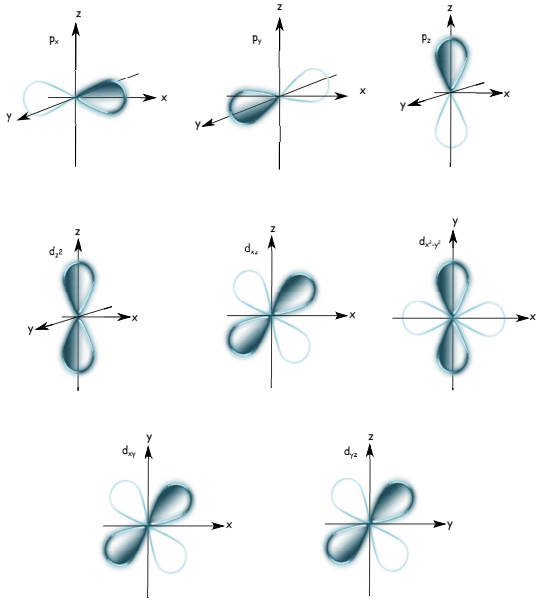

Figure 2.8: Shapes of p- and d-orbitals [21].

in preferential orientations, with a lobe pointing along each direction of the primary axes, one positive and one negative. Furthermore, four out of the five d-orbitals have a similar appearance, each with four pear-shaped lobes, and the centers of all four lying in the same plane. Three of these planes are the xy-, xz-, and yz-planes, with the lobes located between the pairs of primary axes, while the fourth has its centers along the x and y axes. The fifth d-orbital consists of a torus with two pear-shaped regions placed symmetrically on the z axis.

The d_{z^2}- and $d_{x^2-y^2}$-orbitals gives rise to the e_g orbital, which points directly to the oxygens sites; it results in a strong electrostatic repulsion between the electronic clouds. The d_{xy}-, d_{xz}- and d_{yz}- orbitals yield the t_{2g} orbital, which points to empty space; the resulting electrostatic interaction with oxygen is weaker, Fig. 2.9.

The p-orbitals of oxygen split into the p_σ- and p_π- levels. In a solid, an overlap of the orbitals gives rise to bands. A qualitative idea of the energy levels can also be drawn from Fig. 2.10. An overlap of the e_g band with the 5s and 5p bands can occur in MoO_3. The same happens with the 6s and 6p bands of WO_3. The amount of available electrons in both oxides is equal to 24. These electrons precisely fill up

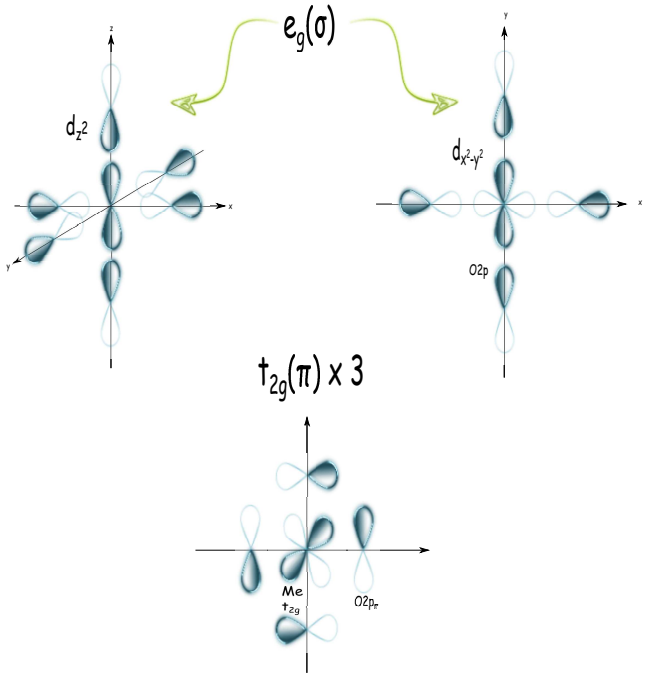

Figure 2.9: Interaction of O2p and d-orbitals in an octahedral configuration [21].

the p_π band and leave the t_{2g} band empty. The Fermi level will thus be found in the middle of the forbidden band, between the t_{2g} and p_π levels. The bandgap energy between these levels is ~ 3.0 eV, in accordance with the transparency displayed by MoO_3 and WO_3 films in the visible region.

When ions and compensating electrons are intercalated into the lattice of an oxide, the excess electrons will fill up the bottom of the t_{2g} band, lifting the Fermi level into this band. In amorphous MoO_3 (WO_3) films, electrons will be trapped in Mo (W) sites of lower energy, and small polarons will be formed. As a consequence, the polaron optical absorption will cause the bluish color of the samples. This effect is shown schematically in Fig. 2.11.

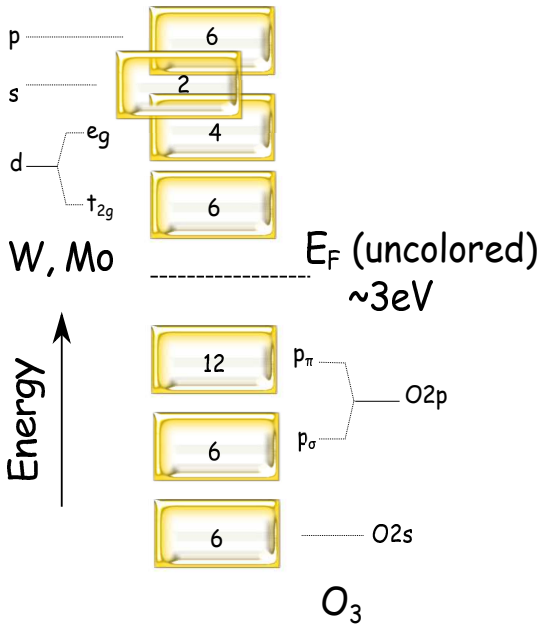

Figure 2.10: Scheme of the band structure of MoO_3 and WO_3 [68].

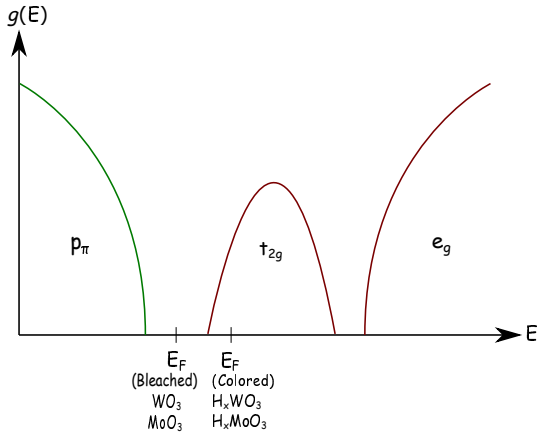

Figure 2.11: Scheme of the density of states and coloration mechanism in amorphous MoO_3 and WO_3 [21].

3

Experimental Fundamentals

The development of this chapter is intended to give a brief explanation of the thin films deposition techniques for both molybdenum oxide and tungsten oxide. In addition the characterization techniques that are useful to define the thin films properties are described below. The study of the optical properties was performed by absorption and optical transmittance for thermochromism and electrochromism, respectively. In turn it used Raman spectroscopy to identified the molecular bonds. Related to the structural properties, the employed techniques for the characterization are: X-ray diffraction (XRD), atomic force microscopy (AFM), transmission electron microscopy (TEM). Moreover, for chemical analysis X-ray photogenerated spectroscopy (XPS) was used, regarding to the chemical composition of W-Ni-Ti films a Rutherford Backscattering Spectroscopy (RBS) technique was employed.

3.1 DC and RF sputtering

The process of depositing thin films is mainly performed through three important processes. The first of them is where it render the production of molecules, ions or atoms that will form the thin film. The second step is the transport of the produced species through a medium by which these species are propagated. Finally it have the condensation process of the thin film on the substrate. Generally, the thin films deposition can be done by two chemical and physical methods. In the literature,

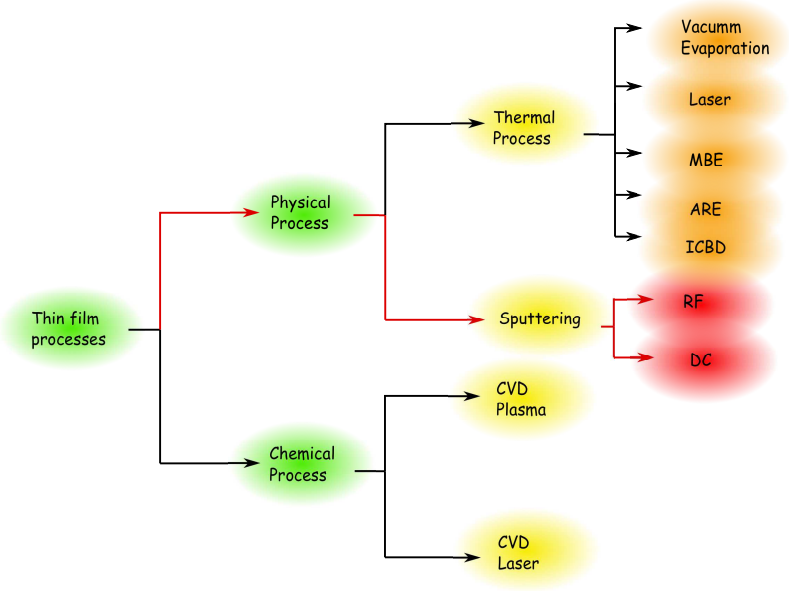

Figure 3.1: CVD and PVD process of deposits thin films.

these processes are divided into physical vapor deposition (PVD) or by chemical vapor deposition (CVD), these terms were coined by C. F. Powell, J. H. Oxley y J. M. Blocher who occupied those terms the first time in 1966 [95]. The CVD process is carried out by a chemical reaction on the substrate surface. By contrast, the PVD process is a term used mainly to describe any variety of developed methods to deposit thin films by condensation of steam of the material on a substrate. Such processes are involved different methods which are purely physicals, such as vacuum thermal evaporation and sputtering (RF or DC) method. The latest are the techniques that were used in this work to obtain MoO_3 thin films and the oxide films composed of W-Ni-Ti, respectively. Figure 3.1 is a diagram of different processes of thin films.

The sputtering system can be illustrated in a simple manner as shown in Figure 3.2. Mostly, the target (material to be synthesized) is connected to a voltage source which can be RF or DC. The substrates for thin films are placed on supports within the vacuum chamber, these supports usually are located exactly opposite of the target. For starting the erosion process[i] it is necessary to introduce a gas

[i]Sputtering (In 1852 W. R. Grove was the first person to study the sputtering technique [95]).

atmosphere which is usually argon (Ar). Such that it creates a medium in which they must obtain stable conditions for the formation of a plasma[ii]. The working pressure within the vacuum chamber is maintained in a range from few mTorr to 100 mTorr to reach the ideal conditions. When the plasma was generated, the ionized molecules are oriented to the target and start to hit the target, mainly removing the neutral atoms due to a momentum change between ionized molecules and the target. Then, these atoms stay traveling to be condensed in the substrate thereby forming the thin film. In some cases, the Ar is not the only gas that can be used, there are other inert gases like nitrogen amount others are used or an gas mixtures are used too, *e.g.* N_2, Ar-O_2. In these cases, the deposition technique is often called reactive sputtering. The purpose in this process is to synthesize compounds in which the main characteristic of the target can be metallic, *e.g.* Mo o W, to form MoO_3 and WO_3 compounds. These compounds are generated when the gas mixture Ar-O_2 is performed [96]. To highlight, that these compounds may have different stoichiometric states these could be controlled by changing the partial pressures of the inert gas and the reactive gas. In general, the main parameters that can modify the morphological and optical structure of the thin films are: **(*i*)** delivered power into the targets, **(*ii*)** the ratio partial pressure of gases (O_2/Ar), **(*iii*)** the working pressure and **(*iv*)** the temperature of the substrate. According to the last two parameters, Thornton proposes a diagram that related the structure of the deposited films according to the values of the working pressure and the temperatures ratio between the absolute temperature, the substrate temperature and the melting temperature of the deposited material T/T_m [96], see Figure 3.3. The zone 1 is mainly characterized by obtaining highly porous thin films. This can be obtained at very low temperatures and high working pressures. The T area is known as a transition zone which is mainly featured by little defined granular structures that are

[ii]Consists of gas molecules ionization, this ionization is due to the formation of a magnetic field generated by applying a potential difference that is created between the target and chamber. In the case, where the inert gas is Ar the plasma has a violet hue type.

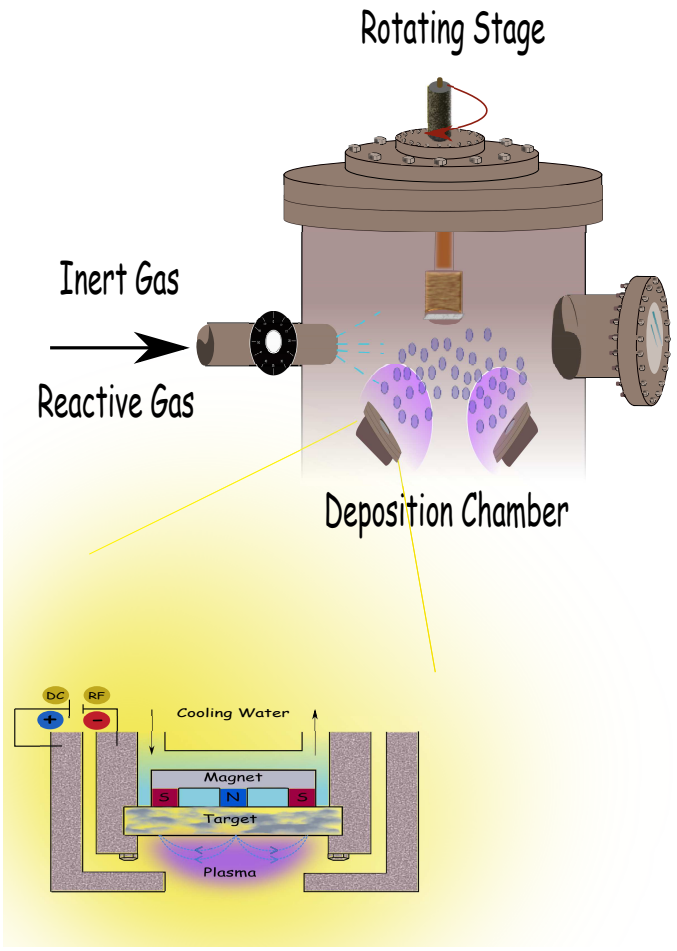

Figure 3.2: Schematic of a sputtering system.

densely packed. Zone 2 shows formations of columnar grains, due to the diffusion of atoms caused by high temperatures. Finally the zone 3 the main feature is a re-crystallization of the material that is notable for the similarity in size and shape of the grains that forms [96].

Related to the differences between the distinct sputtering techniques are: (i) for RF systems, the used source is AC type and mainly this technique is used when the target do not have good conductivity, *e.g.*, insulating material, of this way it prevents that the target it remains electrically charged. The frequencies that are occupy to generate the plasma are in the range of 5 - 30 MHz. (ii) In DC systems, the source

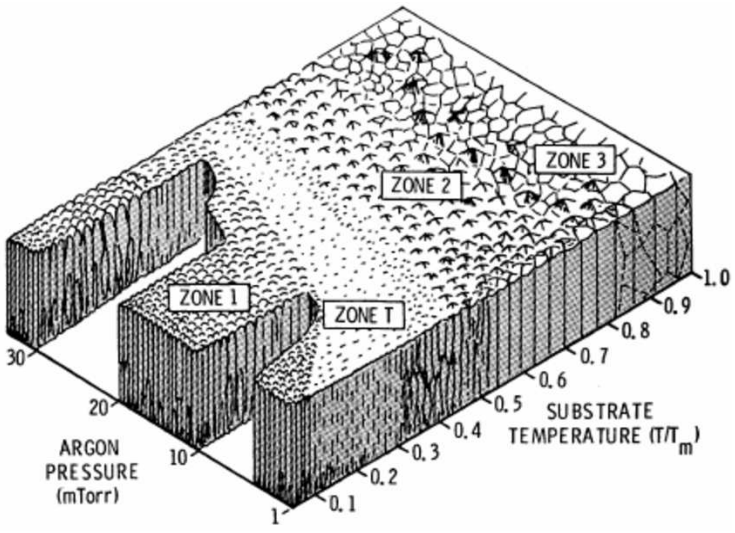

Figure 3.3: Thornton diagram for films that were made by the sputtering technique [96].

that is used is the DC type and generally are used when the targets are conductive. Often the occupied voltage is around 5 kV. The use of this technique to synthesize thin films is widely used by several research groups because of its main advantages: **(*a*)** this is a atomic level nonequilibrium process technique at which the condensates atoms in the substrate have very high energy[iii], **(*b*)** the easy way to erode alloys or compounds, **(*c*)** the erosion rate for oxides is very high and **(*d*)** the easy way to re-scaling the fabrication of films within the industry [97].

3.2 UV-Vis-NIR spectroscopy

The techniques that is used to study the optical properties of materials is the optical absorption spectroscopy, particularly in the spectral region UV-Vis-NIR[iv]. In the ultraviolet region to visible region is of particular interest because its involving energies match with the energy differences of the electronic states of molecules and atoms. The concept of this technique is based as follows: When an electromagnetic wave incised on the material, the total energy of the incident electromagnetic wave

[iii] Values much larger than $0.1eV$ which presents the method of thermal evaporation eV.

[iv] Ultra-Violet region (UV), Visible region (Vis) and Near Infra-Red Region (NIR).

is divided into a part that is transmitted, reflected and another portion is absorbed by the material. The characteristics of each material plays an important role on the energy that will be transmit, reflected or absorbed by the material. Additionally to the material properties, the incident wavelength on the material affect in how the incident wave will be propagated across materials. The manner to measure the transmittance, reflectance or the optical absorbance is done by a UV-Vis-NIR spectrophotometer, although actually there are different designs of these systems, all of them are composed basically of: **(*i*)** a radiating energy stable source as a deuterium and tungsten lamps. The sources emitting in the UV region, visible and NIR region, respectively, **(*ii*)** a monochromator which aims the selection of different wavelengths of the radiation that consist mainly by prisms, filters and diffraction gratings, **(*iii*)** holder samples, where the samples are located for the analysis, **(*iv*)** a detector, converter-amplifier of the optical and electrical signals. Finally **(*v*)** a reading and signal processing system, this type of arrangement is outlined in Figure 3.4. Its important to note that the resolution of spectrophotometers is defined by $\Delta\lambda/\lambda$, where $\Delta\lambda$ is the minimum spectral interval. Usually the spectral range of spectrophotometers is between 200 and 2500 nm.

When the sample is irradiated with a monochromatic light, what is obtained are the absorbance values that follows the law of Bougler-Lambert-Beer[v]. The law establishes the relation of radiation absorption and light-absorbing substance by the following relation:

$$A(\lambda) = \alpha(\lambda)cd \tag{3.2.1}$$

where A represents the absorbance, λ is the wavelength of the incident beam, α is the optical absorption coefficient [cm^{-1} mol^{-1}], c is the concentration [mol] and d is the thickness of the sample [cm]. If I_0 is the intensity of the incident beam and I is the transmitted intensity, then the absorbance is described as:

[v]The law was discovered independently by P. Bougler in 1729 by J. Lambert in 1760 and by A. Beer in 1852 [98].

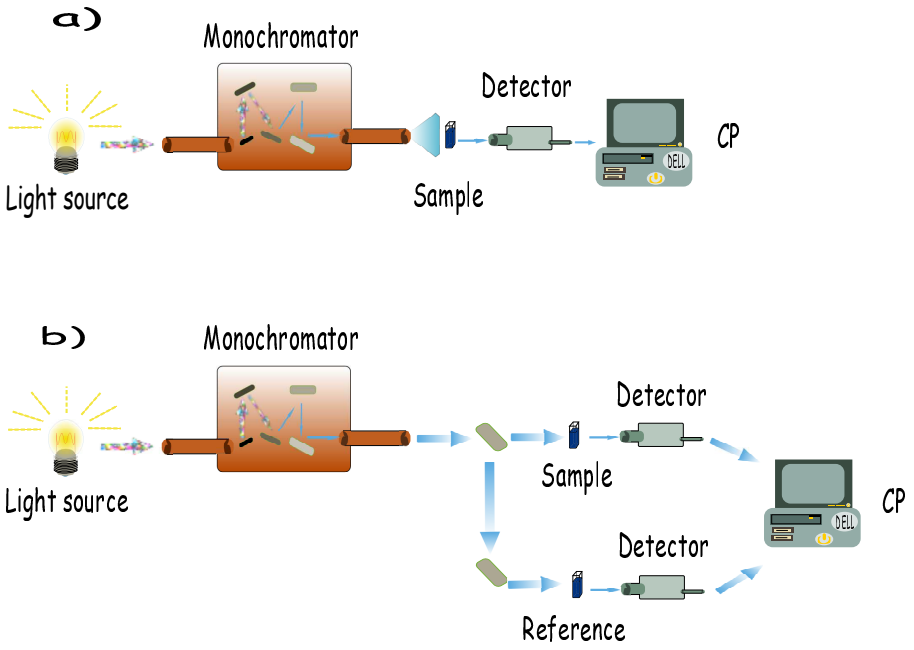

Figure 3.4: Spectrophotometers arrangement.

$$A \equiv \ln\left(\frac{I_0}{I}\right) \tag{3.2.2}$$

Combining 3.2.1 and 3.2.2 the Bouguer-Lambert-Beer law it can be written as follows:

$$I = I_0 \exp^{-\alpha c d} \tag{3.2.3}$$

hence the transmitted intensity decays exponentially.

3.3 Raman Spectroscopy

Raman spectroscopy technique is widely used in the field of chemistry to identify different types of molecules and different types of vibrational or rotational modes that are presented in the molecules. This characterization technique has its beginnings in the 20's when the physical Chandrasekhara Venkata Raman published a series of investigations into the molecular diffraction and in 1928 reported the effect that

leads his name (Raman effect), for which in 1930 he will receive the award Noble price in physics [99, 100]. The first Raman spectrometer was manufactured by Rank and Wiegand in 1942 [101]. The Raman effect is a inelastic scattering phenomenon of light wherein two different types of processes can occur; the transformation of a photon in a given phonon or vice versa. During the phonon generation may occur that the incident photon decomposes into two phonons and one of the new phonons transforms back into a photon due to this transformation one can interpret this phenomenon as a process of photons inelastic scattering, which is caused by the lattice and is accompanied by phonon absorption. To highlight that there are distinct scattering processes depending on the type of phonon that is involved in the process. These phonons it could be acoustic or optical type. Thus if the first phenomenon is carried out this process is called Brillouin's dispersion but if the phonon is an optical type its known as Raman scattering [99].

The dispersion type is used for the characterization of thin films at this work is the Raman scattering which is based on the interaction of light with the molecules. The interaction it could be by distorting or polarization of the electron cloud that is surrounding the nucleus creating a short time life that it been called virtual state. To generate this virtual state is necessary to use a monochromatic beam which intensity is high, like a laser [102]. The generated virtual state, is not stable because the photon is quickly re-irradiated. Notably that the energy of these states also depends in the excitation source wavelength. So at room temperature most of the molecules are in the lowest energy level [103]. Among these, the most likely processes that it is presented is the so called Rayleigh scattering, where the majority of photons that are scattered not involve any energy change and thus the incident photons on the material, returns to the same energy state, *i.e.*, when most of the molecules return to their ground state, a light is emitted with the same wavelength as the incident light. Thus, changing the photon energy becomes a direct measure of the energy of the optical phonons because different situations with the absorbed energy or photon emission may occur. However, when the energy of the re-emission

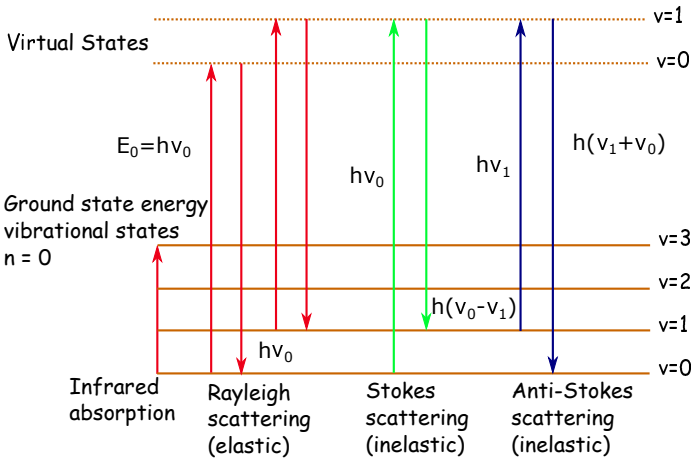

Figure 3.5: Scattering Process of Raman, Rayleigh, Stokes and anti-Stokes types [20].

photon is emitted in the phonons emission process, is lower than the energy of the incident photon to this process that is carried out it is known as Stokes-Raman scattering type. The case when the re-emitted photon energy is greater than the energy of the incident photon it is called scattering type anti-Stokes, see Figure 3.5.

The relative intensities depend on the temperature and the population of the different states of the system. For the latter two types of dispersion it is important to emphasize that the anti-Stokes scattering in compared to the Stokes scattering is much lower in probability to occur. Figure 3.6 shows a Raman spectrum where it can be seen that in the case of Rayleigh scattering there is no shift in the wavelength unlike in the Stokes scattering wherein the shift is positive. Importantly that the intensities that corresponds to these two dispersion processes are much bigger than the intensities that display in the anti-Stokes scattering. Actually this spectrum is amplified in Fig. 3.6 in order to be able to compare better with the other two scattering types.

The Raman spectroscopy is a method that complements other characterization techniques as the infrared region (IR) spectroscopy in which you can measure from 4000 to 400 cm^{-1} [102]. Hence it would be appropriate to write a little of this spectroscopy type. IR spectroscopy is a method that consists principally in excite a

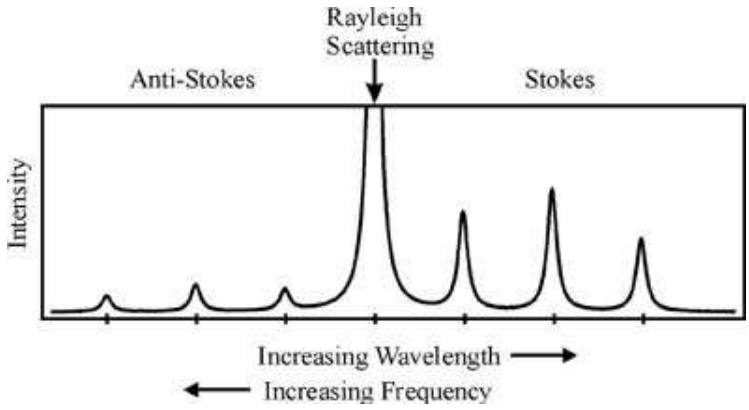

Figure 3.6: Typically signal of Raman, Rayleigh, Stokes and anti-Stokes scattering [104].

photon such that its energy matches precisely with the energy difference between the ground state and the excited state. As the IR region span fundamental vibrations of atoms, all the incident photon energy in the sample can be interpreted as an increase in the vibrational state of the lattice. Therefore, whenever have an vibrating atoms the information of how these atoms are absorbing the infrared energy that impinges on the atoms is obtained, *i.e.*, different absorption bands atributed to the IR absortion are be observed. Therefore this is the way a photon can be absorbed without any re-emission of another photon.

A spectrophotometer Raman is constituted by the components, such as: (i) a radiation or excitation source, which generally the lasers are used, (ii) a lighting systems and light receptors, (iii) detection system and automated control and finally (iv) the spectrometer. The most common spectrometers are the confocal. These essentially consist of a optical microscopy system that allow us to study in detail some interest regions. In Figure 3.7, two types of detectors are shown, one of them is an avalanche photo-diode (APD) whose purpose is the rapid Raman image acquisition also it can appreciate a device of interconnected cameras, Charge-Coupled Device (CCD), that it used to produce images with better resolution of the Raman spectrum. A very important component in the Raman device is the Notch filter system to select and remove the corresponding Rayleigh scattering signal which is

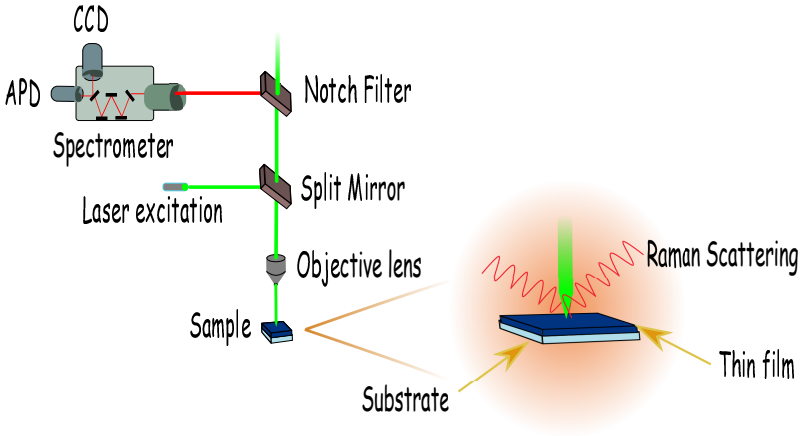

Figure 3.7: The confocal Raman spectrophotometer diagram.

very important when such scattering information is not require.

3.4 X-ray diffraction

The crystal structure of the materials is usually determined experimentally by studying the diffractions of the charactheric wavelength in a material. These studies have been done since the discovery of the X-ray diffraction effect in the materials, which were performed by M . Von Laue and his collaborators W. Friedrich and P. Knipping in 1912. Where not only the periodicity of the crystal structure is tested but also the wave nature of X-rays [105]. The crystal structure analysis requires that the irradiation wavelength is of the order of the inter-atomic crystal space. Usually, most of the crystals have an inter-atomic spacing on the order of a few Å's (1 Å = 10^{-8} cm) [106]. Laue established that atoms of a material produce a diffracted X-ray beam, leading a lot of diffracted beams whose directions and intensities depend on the structure and the composition of the crystal. The simplest method to study the X-ray diffraction is due to W. L. Bragg. He proposed that material is consisted of a different successive planes that will cause a specular reflection where the incident angle is equal to reflection angle. Furthermore it is assumed that the radiation is elastically dispersive, *i.e.*, the incident and reflected wave have the same wavelength.

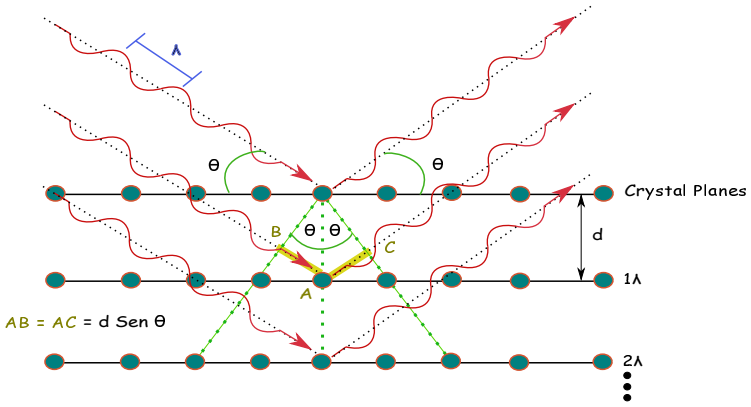

Figure 3.8: Depiction of Bragg's X-ray diffraction [20].

The maximum diffraction, only are going to find for those incidence and reflection directions such that reflections from neighbour planes interfere constructively, this can only occur when the length difference in the path between the reflected beams is equal to an integer (n) of the X-rays wavelengths (λ), see Figure 3.8. Clearly, this condition is satisfied when:

$$2d\sin(\theta) = n\lambda \tag{3.4.1}$$

where d is the interplanar distance and θ is the angle between the incident beam and the crystal planes. This equation is called Bragg's law [106]. Therefore, the strongly diffracted beams are propagated outside the crystal in directions such that satisfies the Bragg relation [107]. Thus, the diffracted beam carries the information either of the internal or surface structure of the crystal.

Generally, they have adopted many experimental methods to study X-ray diffraction; among the most prominent are: ***(i)*** Laue method, where the incident radiation includes a large number of wavelengths, ***(ii)*** Bragg method, where the incident radiation is monochromatic and the measurement is susceptible to the rotations around a fixed axis, also called rotatory crystal method. Finally ***(iii)*** Debye-Scherrer or powder methods, here the radiation as in the above method it is monochromatic but the difference is that the material to be studied is replaced by a pulverized

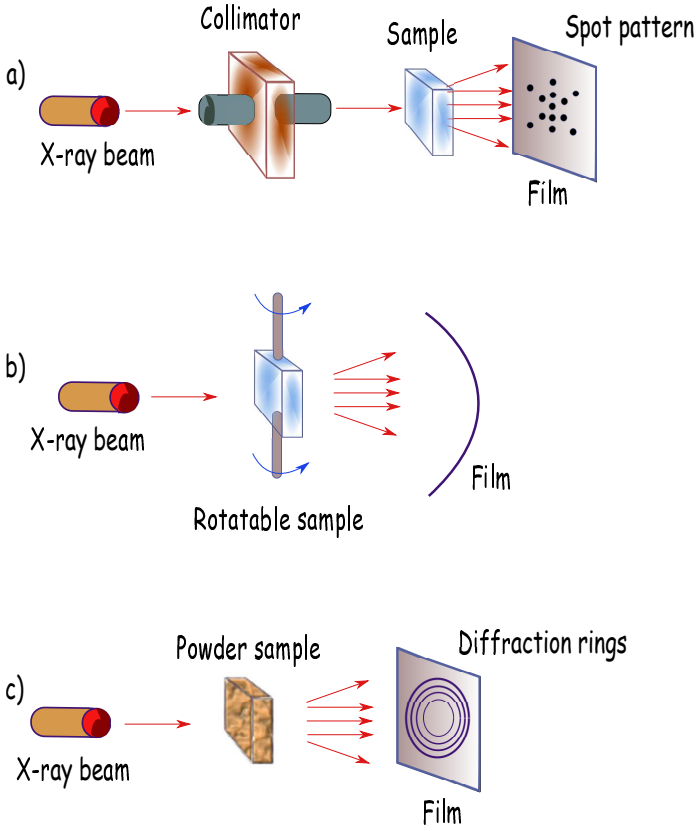

Figure 3.9: Experimental methods for obtaining diffraction patterns.

material. Some of the micro-crystals of the powder samples will be oriented in a particular diffraction angle for a specific set of planes [107, 108], see Figure 3.9. This type of radiation is generated when the atoms are accelerated across to a difference potential that is in a range from 20 to 50 kV, these atoms collide with a metal anode causing that the anode emits a continuous spectrum of white light [109].

Nowadays the X-ray tubes operates at high vacuum, the filaments will be found within these tubes. The filaments used are copper or molybdenum. The filament plays a role as a source of electrons that are generated when the filament is heated[vi], these electrons are accelerated due to the potential difference between the filament and target where electrons are impacting, these are the cathode and anode,

[vi] This effect is called thermionic effect.

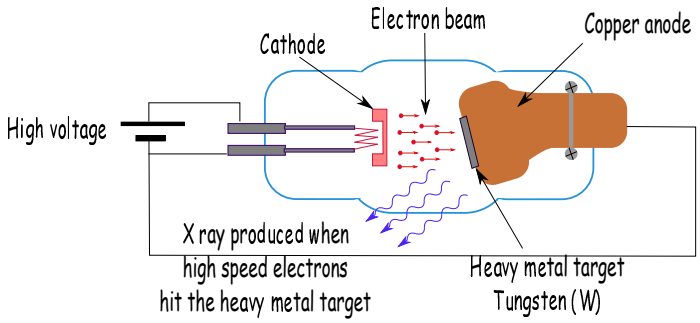

Figure 3.10: X-ray generator.

respectively. A diagram of an X-ray generator is presented in Figure 3.10.

3.5 Atomic Force Microscopy

The topography of thin films was studied with AFM. It is an optical mechanical system which has been developed as a useful tool for direct measurement of intermolecular forces [110]. So it is very useful for application in many areas of research such as electronics, semiconductors and many other areas. This microscopic technique allows the sensing in real time and in a scale on the order of nanometers so it has great advantages when compared with other microscopy systems such as transmission electron microscopy (TEM) that this microscopy technique will be explained in *Section 3.7*. The AFM technique is a part of scanning probe microscopies (SPM), *i.e.*, the acquired images of the material surface are obtained by a physical probe that measure the interest region. This system uses a very thin tip to explore directly the surface of the sample through a mechanical scanning using piezoelectric crystals which expand or contract through a electric current. The system operation is based on scanning the surface with the tip which has dimensions of approximately a few microns in length and at least 100 Å of diameter. The tip is located at the end of a plate (*cantilever*) which have a length between 100 and 200 microns, in turn, this plate is located on a piezoelectric device. So the main idea of an AFM system is to obtain three-dimensional images of samples. These images are obtained by mechan-

ical interaction between the forces that are detected at the sample and the tip that is mounted on the cantilever. The sample is placed on a piezoelectric scanner that will allow the three-dimensional location with high accuracy at a nanometer scale. The deviation or vertical inclination of the cantilever can be measured because the system used a laser beam which is focus in a free part of the cantilever and is reflected in a photo-diode. During scanning, the tip over the sample, the interatomic force between the tip atoms and the surface atoms, produce a bending movement on the cantilever. This bending is detected by a sensor denominated photo-detector so the signal will be recorded on a computer. To determine the height of the tip over the sample so that the bending of the cantilever keeps constant, a piezoelectric actuator is used. Once determined this point is possible to draw a topographical map of the sample. When the tip is very close to the sample, here the system gives us an approximation of the value of the interatomic force. During this process the tip is oscillated vertically about the sample, while information is obtained when the cantilever is bent. It exists between atoms a repulsive force and an attractive forces when the interatomic distance decreases. Interaction forces come to zero, when the distance between atoms reaches a few angstroms and will challenge-repulsive when atoms are in contact, the schematization of a atomic force microscope can be seen in Figure 3.11.

The atomic force microscopy is a versatile system that allows the user to change the operation mode and among the most important it have:

- *Non-contact Mode:* This operation mode is characterized by vibrating tip of the cantilever that is near the resonant frequency, so that the tip vibrates near the sample surface at a distance between 10 -150 Å above the sample surface. Thus it is possible to detect the attractive Van der Waals force which is acting between the tip and the sample. When the tip goes over the sample surface, the attractive force causes a decrease in the oscillation frequency. However, the system corrects the distance from the tip to the surface in order to keep constant the oscillation in the cantilever.

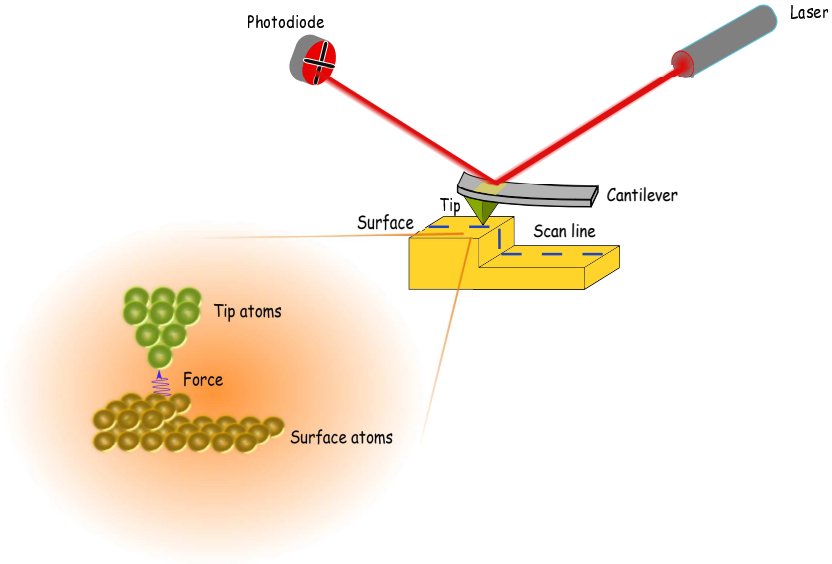

Figure 3.11: The representantion of atomic force microscopy.

- *Tapping Mode:* One of the big problems that have the atomic force microscopy, is the deterioration of samples but thanks to this technique it is possible to solve the problem. This model is very similar to the previously presented mode, the main difference is in the tip oscillation amplitude and the cantilever which are very large between 100 and 200 nm, in this region the force is repulsive and attractive type.

3.6 X-ray photoelectron spectroscopy

The electron spectroscopy is a technique that uses the characteristic electrons emission (photoelectrons) of a material for elemental analysis. The characteristic electrons exhibit characteristic energy levels that reveal the nature of the chemical elements of the studied materials. The photoelectrons can only escape from the top of atomic layer of the material[vii] due that the energies are relatively low (20 - 2000 eV). Therefore, this type of spectroscopy is a surface chemical analysis technique [111]. Ther are two types of electron spectroscopy: **(*i*)** Auger electron spectroscopy

[vii] 10 nm in depth or less.

(AES) and ***(ii)*** X-ray photoelectron spectroscopy (XPS) however this electron spectroscopy is also referred to the chemical analysis (ESCA) [112]. This work will be focussed only in XPS technique. The Swedish physicist Kai Siegbahn built an instrument able to detecting the emission of core photoelectrons with a sufficiently high resolution energy which allowed the specific analysis of elements, so in 1981 he was awarded with the Nobel Prize in Physics by the development of this system [112]. The popularity that has taken the XPS analysis lies mostly in the ability to: ***(i)*** identify and quantify the elemental composition of any element that is at least at 10 nm depth from the surface. It is significant to remark that for that the amount of the element be identifiable the element composition must be > 0.05 at.%. ***(ii)*** The chemical information is obtained as oxidation states, molecular orbitals among many other features and ***(iii)*** obtaining data are relatively easy since the preparation for the analysis of the sample is not complicated as compare with TEM [112]. The production of photoelectrons can be described simply in one step as a process in which an electron was initially attached to an atom that is extracted from different electron shells that was containing in the atom. This is performed when a photon is absorbed from X-rays. Figure 3.12 is the diagram of the photoelectron emission X-ray spectroscopy. Therefore, when the incident X-ray photon energy is large enough ($\sim h\nu$) to extract an electron from an inner electron shell, this is ripped from the surface as a photoelectron. These photoelectrons are collected and analysed by an XPS spectrometer, which is responsible for measuring the kinetic energy of the photoelectron E_k. The binding energy of the photoelectron that belong to the atom E_B can be calculated if the kinetic energy E_k is known, so this type of energy is related to the following equation:

$$E_B = h\nu - E_k - \phi \tag{3.6.1}$$

where the ϕ parameter represents the required energy by an electron to escape from the surface material, better known as the work function that depends on two parameters such as material and the spectrometer [111–113]. The spectrometer

systems consist by a X-ray gun for XPS analysis. The operation of these guns is very similar to X-ray tube that is used for X-ray diffraction. The X-ray photons are generated when electrons with a very high energy hit a metallic anode which are commonly of aluminum (Al) (AlK_α 1.4866 keV) or magnesium (Mg) (MgK_α 1.2536 keV), being these energies very lower than the energies used in X-ray diffraction which are 8.04 and 17.44 keV for CuK_α (copper) and MoK_α (molybdenum) [111]. Therefore the XPS spectrum is characterized as a function of the peak intensity *vs.* binding energy where in each peak corresponds to a certain electronic level. The XPS spectra displays three types of peaks: **(*i*)** peaks that are due to photoemission near to core electronic levels, **(*ii*)** photoemission due to valence levels and **(*iii*)** Auger emission due to the excitation of the X-ray. The peaks of the generated photoelectron of closest levels to the core are the main peaks in the elemental analysis. The generated peaks in the valence levels are found in lower binding energies (0 - 20 eV) are mostly used to study the electronic structure of the materials. The Auger peaks are caused by the excitation of X-rays in a Auger process generally also be used in chemical analysis. One of the main problems to quantify elements on an XPS spectrum is the signal analysis that is called baseline (background) which has a shape of stepwise type which is originated by many sources but especially is attributed to inelastic scattering of electrons. The non-discrete energy loss resulting from inelastic scattering[viii], produces a very broad base line in the low kinetic energies region. Commonly three different routines to describe and remove the background in the peaks of interest are used: **(*i*)** Linear, which as its name suggests it draws a linear function between two points located on the ends of the XPS signal, **(*ii*)** Shirley, this routine is where a function such as "S" in area of interest is assumed, this form is defined by the trend observed in the peaks intensity on the sides of lowest and highest energy of each signal. Finally **(*iii*)** Tougaard method this is the only routine that tries to calculate the background subtraction doing a simulation of the inelastic scattering. Figure 3.13 displays these three types of background subtraction

[viii] Energy lost by the electrons within the solid with its surroundings.

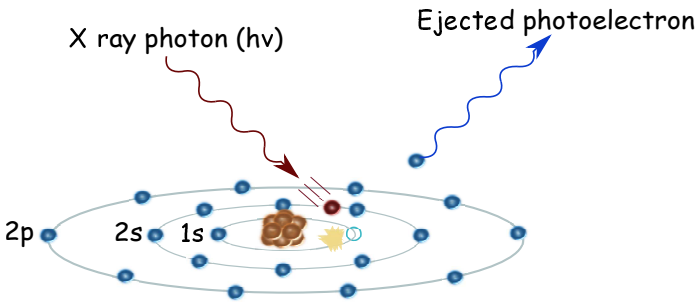

Figure 3.12: XPS photoelectron emission process.

methods.

3.7 Transmission electron microscopy

This technique is used primarily to obtain information on the morphology and microstructure of a material [114]. The technique consists of forming images obtained from the interaction of electrons that achieved to be transmitted through the material with a thickness between 5 and 100 nm [115]. These electrons are generated by a filament which is heated by the thermionic effect[ix] by Schottky effect[x] or field emission[xi] [114, 115]. Besides this, the filament is in vacuum; subsequently the generated electrons are accelerated by a potential difference in a range of 80-300KV, whose speed is about $v = 4.2\times10^6$ m/s and its wavelength is $\lambda \sim 0.0027$ nm at 200KV [116]. Therefore, the electron's wavelength is comparable with atomic dimensions so that the electrons will be strongly diffracted by the periodic arrangement of atoms that are on the crystal surface.

This phenomenon was first studied in 1927 by Davisson and Germer [116]. When electrons reach an accelerating potential around 50 kV, these will acquire very high energies so they can penetrate to a few micrometers into the material. However if the material has crystalline properties the electrons are diffracted by

[ix] Tungsten filament (W) and lanthanum hexaboride filament (LaB_6).
[x] Zirconium oxide filament (ZrO) and W filament.
[xi] W filament.

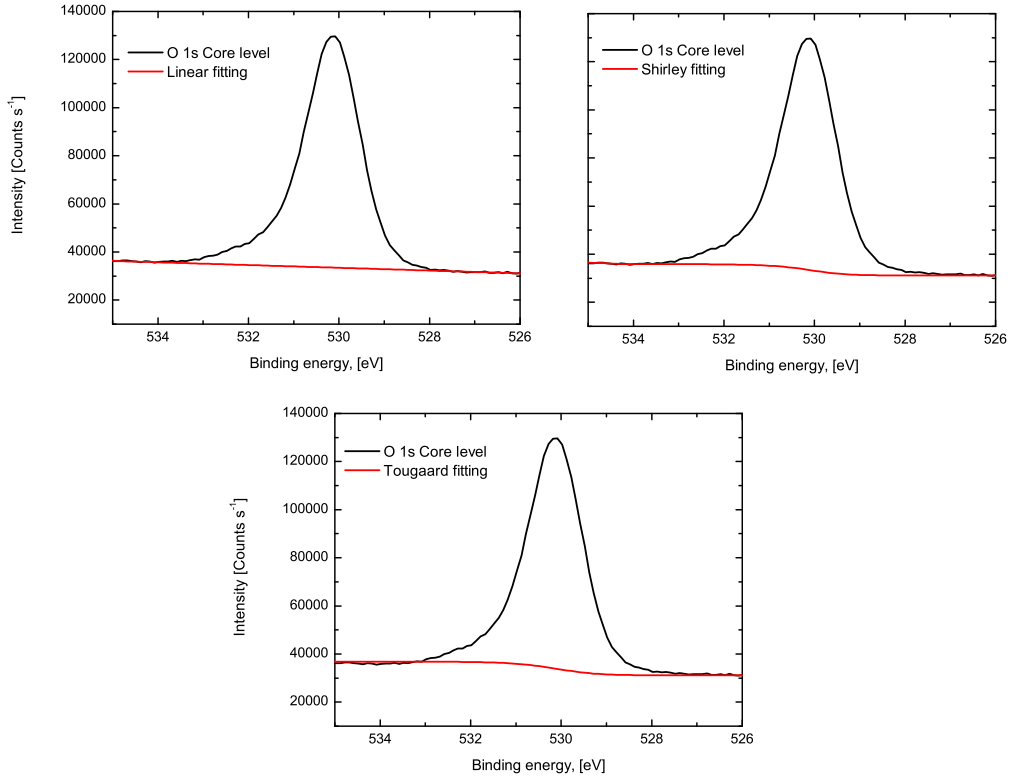

Figure 3.13: Types of routines for background subtraction. The labels indicate the fitting.

the atomic planes that is within the material. Thus it is possible to generate an electron diffraction pattern of the transmission electron when going through the material. This was demonstrated by G. P. Thomson in 1927 [116]. Later in this year it was observed that the transmitted electrons could be focused. Thus allowing to generate images with a much better spatial resolution than a conventional optical microscope. The need for TEM imaging approach is achieved through the condense lens systems, as shown in Figure 3.14. The image can be collected directly on a photographic film or on a plate screen within the vacuum chamber or digitally via a fluorescent screen coupled to a CCD camera [115]. The transmission electron microscopy technique is also a useful tool for obtaining information from the crystal

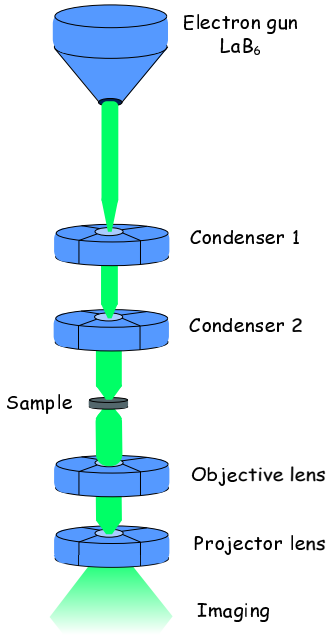

Figure 3.14: TEM system.

planes of a material by the high-resolution transmission electron microscopy (HR-TEM). The high resolution can be obtained from electron diffraction patterns which can be compared with the diffraction patterns obtained by XRD and the information of preferential planes of the material. A diagram of a TEM apparatus is shown in Figure 3.14.

3.8 Rutherford Backscattering Spectroscopy

The first experiments with backscatter alpha particles were done about hundred years ago in the years 1909 to 1911 by Ernest Rutherford [117]. The RBS is a technique used to measure the depth distribution of elements found in the surface or within studied material to an one micrometer depth. The technique is basically based on elastic scattering of ions between a large energetic light ions beam and the atoms that are near to the material surface [118, 119]. Generally the ions that are the most used in spectroscopy are of $^4He^+$ which are generated in an accelerator

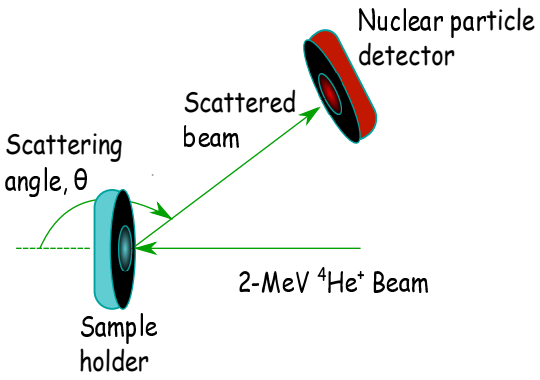

Figure 3.15: Schematic illustration of a RBS configuration system.

with an energy range between 1-2 MeV [117–119]. When these ions penetrate the material, the energy is loses and many of them are scattered by electrons and a partial fraction of the electrons will be strongly scattered by the atom's core that it integrate the material [118]. The core-ion collisions are normally an elastic collisions in which the core of the ions simply bounce off in the atom core of the material due to the electrostatic repulsion between the electric charges that have both cores [118]. In a typically RBS measurement the geometry is an important parameter because of this, the energy detector is located at an angle of 150° or 170° and the surface of the sample is placed perpendicular to the direction of the incident beam [117], as shown in Figure 3.15.

Figure 3.16 shows a typical spectrum of RBS of $W_{0.46}Ni_{0.37}Ti_{0.17}O_3$ sample deposited on a carbon substrate where it can be observed that the position of each peak represents a specific atom type. The relative height of these peaks provides the atomic concentration of the element in the sample. The thickness of the thin film is related to the peak width. It is outstanding to note that in each measurement the system is calibrated by measuring knowing elements the most used are: platinum (Pt), silver (Ag) and copper (Cu). The biggest disadvantage of this technique is the limited sensitivity to detect and quantify small masses ($<$ 20 atomic mass) and light elements such as hydrogen. A further drawback is the depth resolution that is about 20 nm. The RBS experimental data are adjusted by a substrate-film model using of

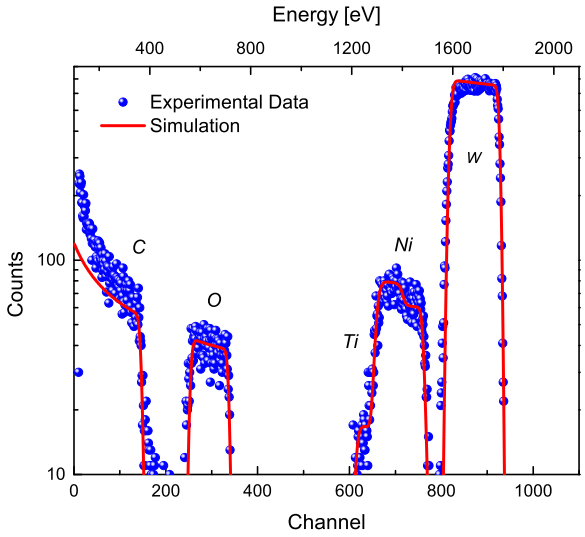

Figure 3.16: RBS spectrum of $W_{0.46}Ni_{0.37}Ti_{0.17}O_3$ sample, deposited on a carbon substrate. The x-axis are in logarithmic scale to observed the contribution of Ti and Ni.

SIMNRA program [120].

3.9 Cyclic voltammetry

The electrochromic effect is induced by the insertion of ions and electrons into the thin film a representation of the electrochromic phenomenon is shown in Figure 3.17. The intercalation and de-intercalation of ions and electrons is performed by a process of cyclic voltammetry (CV) in order to study the electrochemical properties of materials. The electrochemical process is responsible for studying the reactions involved in the electron transfer process through two electrodes submerged in a solution and wherein the electron transfer reaction changes the material by a oxide-reduction process (redox) [42]. The redox process in an electrochemical experiment which is accomplished by applying a potential $V_a \neq V_{cell}$[xii]. This potential could be indicated the location of the Fermi level in the band structure of the deposited

[xii] V_{cell} which is a equilibrium potential before applying of a potential or an external current difference. It is also known as open circuit potential (OCP).

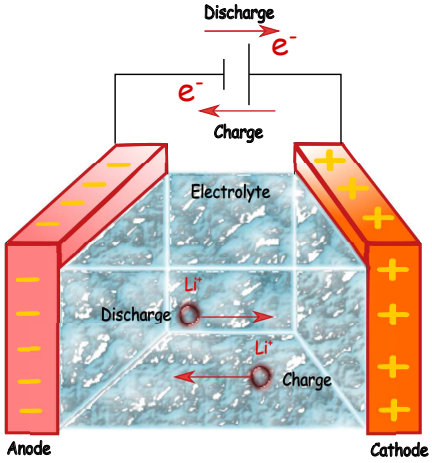

Figure 3.17: Ion intercalation process and the electrons charge balance in a electrochromic thin film.

film [121]. In the system, a charge flow is the responsible for activating the redox process. The reduction process is performed when the value of the applied potential is below the equilibrium potential so that the oxidation process is performed when the applied potential is above this same potential [42].

In this work three electrodes types are used (working, reference and counter electrode) that were immersed in an electrolyte which will talked about in results section, see Figure 3.18. The potential applied between the working electrode and reference causes an increase in the ions mobility from the electrolyte to the electrochromic film. Therefore the induced current can be measured per time unit and directly proportional to the electron charge Q between the counter electrode and the working electrode as:

$$I = \frac{dQ}{dt} \tag{3.9.1}$$

however what it is commonly report is the total charge Q inserted-extracted per square centimeter obtained by integrating the current over time.

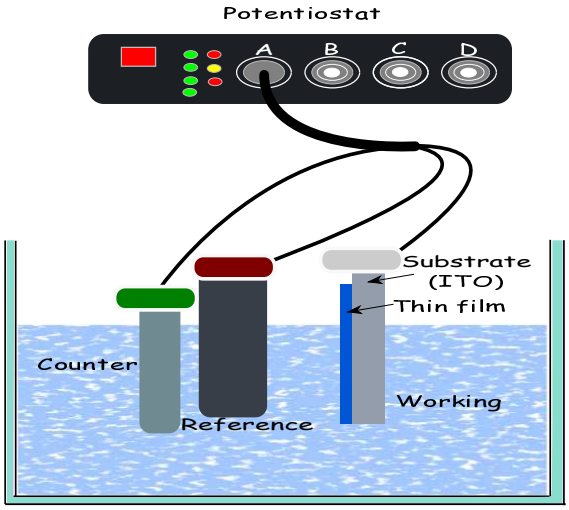

Figure 3.18: Scheme of the arrangement of three electrodes immersed in an electrolyte.

4

Experimental Development

In this chapter the experimental methods for cleaning substrates and MoO_3 and $W_{1-x}Ni_xTi_yO_3$ thin films deposition are described. The RF or DC deposit conditions are defined, respectively. The experiments of thermochromic and electrochromic properties were done. Obtained nanostructured materials were analyzed by different characterization techniques such as: optical absorption spectroscopy, Raman spectroscopy, X-ray diffraction (XRD), X-ray photoelectron spectroscopy (XPS), atomic force microscopy (AFM), transmittance electron microscopy (TEM), backscattering spectroscopy, cyclic voltammetry.

4.1 MoO_3 samples for thermochromic experiments

4.1.1 Substrate cleaning

The MoO_3 thin films were deposited with the RF-sputtering technique on glass substrates (*Corning-7059*). These substrates were treated previously to their deposition to a cleaning treatment which consist of:

- The substrates were placed in a Teflon holder, it were immersed successively in solvents such acetone, ethanol and iso-propane, to be subjected to an ultrasonic treatments each one for 20 min.
- The substrates were subjected to a drying process being exposed to a moderate

nitrogen gas flow N_2.

- After substrates drying, they were placed in Petri boxes and storage in a desiccator until the time of thin film deposition.

4.1.2 MoO_3 growing

The MoO_3 were deposited on Corning-7059 glass substrates by reactive RF sputtering technique at room temperature in a deposition system based on a Intercovamex-V1. The target was 5-cm-diameter plate of metallic molybdenum with a purity of 99.95% Cathay Advanced Materials Limited. The deposition chamber reached a vacuum level of $2.5\times\ 10^{-5}$ Torrs before entering a gas mixture of argon and oxygen at a O_2/Ar ratio equal to 0.18. The working pressure was maintained during deposition at $4.5\times\ 10^{-3}$ Torrs and the discharge power int the target was maintained at 35 Watts with a deposition rate 0.2 Å/min. The film thickness was determined by quartz crystal oscillator. The typically thickness of the Mo_3 sample was $\sim$50 nm.

4.1.3 Thermochromic effect induction

The thermochromic effect of MoO_3 thin films was studied exposing the samples to two types of atmospheres, in the case of air a conventional furnace was used, the annealing temperature was varied in the range of 25-300°C holding these temperatures for 2 hrs. A second set of samples were exposed to an argon-rich atmosphere created by passing an argon flux trough a quartz tube at rate of 5 lt/hr during 30 min before the start heating of the samples. The flux was kept during the annealing, using the same temperatures as the air treatments for 2 hrs. The samples cooling took place with a constant flux argon.

4.1.4 Characterization techniques

The optical absorption spectra were obtained using an UV-Vis-NIR spectrophotometer Perkin-Elmer Lambda-2 in a range between 300 to 1100 nm. The XRD analysis of

the samples were obtained with a D5000 Siemens diffractometer using the radiation from the excitation line CuK_α ($\lambda = 1.54$ Å). The information about the structure of the MoO_3 thin films as well as their morphology were performed by high resolution transmission electron microscope (HR-TEM), JEOL JEM-2010 at 200 kV. The Raman spectra were obtained on a Horiba Jobin Yvon microRaman spectrometer using 632.8 nm as an excitation line from a He-Ne laser whose output power is 20 mW. The XPS analysis were obtained by using a K-Aplha equipment, the excitation line was the Al K_α (1487 eV), in all the measurements was used an energy step size of 0.10 eV, the pass energy of 50 eV and the spot size around 400 μm. Finally, the nano-topography structure was acquired by AFM, JSPM-5200 Environmental Scanning Probe Microscope in tapping mode with silicon tip cantilevers.

4.2 $W_{1-x-y}Ni_xTi_yO_3$ samples for electrochromic experiments

4.2.1 Substrate cleaning

The $W_{1-x-y}Ni_xTi_yO_3$ thin films were deposited with the DC sputtering technique in a deposition system based on a Balzers UTT 400 unit, on transparent and electrically conducting layers of In_2O_3:Sn (ITO) with an electrical sheet resistance of 40Ω per □. These substrates were treated previously to the deposition to a cleaning treatment which consist of:

- The substrates were placed in a holder it were immersed successively in solvents such acetone, ethanol and iso-propane, to be subjected to an ultrasonic treatments each one for 20 min.
- The substrates were subjected to a drying process being exposed to a moderate nitrogen gas flow N_2.
- After substrates drying, they were placed in Petri boxes and storage in a desiccator until the time for thin film deposition.

4.2.2 $W_{1-x-y}Ni_xTi_yO_3$ growing

Thin films of W oxide, W-Ni oxide and W-Ni-Ti oxide were prepared by reactive DC magnetron sputtering in a deposition system based on a Balzers UTT 400 unit. Targets were 5-cm-diameter plates of W, Ni, W(95 wt%) + Ti(5 wt%), and W(90 wt%) + Ti(10 wt%) (Plasmaterials), all with 99.99% purity. The sputter system was first evacuated to $\sim 1.7 \times 10^{-7}$ Torrs. Argon and oxygen, both of 99.997% purity, were then introduced through mass-flow-controlled gas inlets. The O_2/Ar gas flow ratio was set to 0.15 and the pressure was 3×10^{-2} Torrs; these parameters were chosen on the basis of previous studies [122] and are known to yield porous films with good EC performance. Films of W-Ni-Ti oxide were obtained by co-sputtering from either of the W-Ti targets and the Ni target and setting the sum of the two target powers, denoted P_{W-Ti} and P_{Ni}, respectively, to 230 W. The deposition rate was for W $\approx$ 0.6 nm s^{-1} for Ni $\approx$ 0.3 nm s^{-1} and W-Ti(10 wt%) $\approx$ 0.25 nm s^{-1}. Some films of W-Ni oxide were prepared by use of the Ni target with $P_W + P_{Ni} = 230$ W [122]. Film thicknesses were $\sim$ 300 nm as measured by surface profilometry using a Bruker DektakXT instrument. Most films were studied in as-deposited state, but some samples were heat treated at 400°C for 2 hrs in air in order to induce crystallization.

4.2.3 Electrochromic effect induction

The W-oxide-based films were investigated by CV using a computer-controlled ECO Chemie Autolab/GPES interface in a three-electrode electrochemical cell with the sample as working electrode and Li foils serving as reference and counter electrodes. The electrolyte was 1 M $LiClO_4$ in propylene carbonate (Li-PC). All measurements took place inside a glovebox with inert argon atmosphere. The voltage range and sweep rate were 1.7-4 V *vs.* Li/Li^+ and 10 mV/s, respectively. This voltage range was chosen in order to produce rapid degradation of the films.

4.2.4 Characterization techniques

Optical transmittance T was recorded in-situ at a mid-luminous wavelength of 550 nm during CV cycling, using an Ocean Optics fiber-optic instrument, for the various W-oxide-based films. Structural characterization was accomplished by XRD using a Siemens D5000 instrument operating with CuK_α radiation at a wavelength of 0.154 nm. Elemental compositions were determined by RBS performed at the Uppsala Tandem Laboratory using 2 MeV $^4He^+$ ions backscattered at an angle of 170°.

5

Results and Discussion

In this chapter, the experimental results for the thermochromic MoO_3 thin films as well as for the electrochromic $W_{1-x-y}Ni_xTi_yO_3$ thin films are discussed. On the one side, the thermochromic response of MoO_3 thin films was mainly characterized by UV-Vis-NIR spectroscopy, with complementary analysis performed by X-ray diffraction, transmission electron microscopy, atomic force microscopy, Raman spectroscopy, and XPS. On the other side, the W-Ni-Ti oxide thin films were mostly characterized by cyclic voltammetry and UV-Vis-NIR, obtaining the optical modulation change, the charge density insertion-extraction, the coloration efficiency, and durability. The structural and elemental composition of these films were obtained by X-ray diffraction and the RBS technique.

5.1 Thermochromic effect of MoO_3 thin films

5.1.1 XRD of MoO_3 thin films

Molybdenum trioxide thin films were deposited by rf reactive magnetron sputtering with an average thickness on the order of 250 nm. Displayed in Fig 5.1 are the XRD patterns for the as-deposited MoO_3 sample and the set of MoO_3 films annealed in either air or argon atmospheres at 300°C for 2 h. As expected, the diffractogram for the as-deposited sample shows the characteristics of an amorphous material.

The amorphous nature of MoO_3 thin films has been usually observed in samples synthesized at room temperature by other techniques, for instance, by thermal evaporation in vacuum [14, 123]. It is noted that the samples subjected to the air annealing undergo crystallization, with intense diffraction peaks at $2\theta = 12.84°$, 23.40°, 25.90°, and 39.14° assigned to the (020), (110), (040), and (060) crystallographic planes of the thermodynamically stable orthorhombic α-MoO_3 phase, respectively (JCPDS-ICDD card 05-0508) [34]. In addition, less intense peaks were recorded at 40.66°, 46.58°, and 59.10°, identified with the (-103), (013), and (014) planes of the metastable β-phase of this oxide (JCPDS-ICDD card 01-085-2405). Therefore, a mixture of the two most common crystal structures of this material were found for samples annealed in air. Other less frequent phases of MoO_3 have been previously reported, although their synthesis is typically carried out at high pressures and high temperatures [124, 125]. The crystallite size, d, was determined from the Scherrer's equation

$$d = \frac{0.9\lambda}{\beta \cos\theta} \tag{5.1.1}$$

where λ is the wavelength of the X-ray radiation, β is the full width at half maximum (FWHM) of the XRD peak, and θ is the Bragg angle. By using data of the most intense peak, associated with the (040) plane, a size of about 8 nm was obtained for the crystallites. The annealing in argon also led to a mixture of phases, although in this case the film consisted of the β-MoO_3 phase and the Magneli phase Mo_9O_{26}. Indeed, on the one side, the peaks recorded at $2\theta = 33.60°$, 40.66°, 53.16°, 55.30°, and 58.94° are ascribed to the planes (110), (-103), (004), (120), and (014) of the monoclinic β-MoO_3 phase (JCPDS-ICDD card 01-085-2405). On the other side, the diffraction peaks at $2\theta = 21.18°$, 22.96°, and 33.02° correspond to the (400), (401), and (014) planes of the Magneli phase Mo_9O_{26} (JCPDS-ICDD card 05-0441). In agreement with our measurements, this phase shows a distinctive "violet-bluish" coloration and its synthesis has been attributed to an incomplete oxidation of molybdenum oxide [126]. The lattice parameters a, b, c and the interplanar distance d_{hkl}

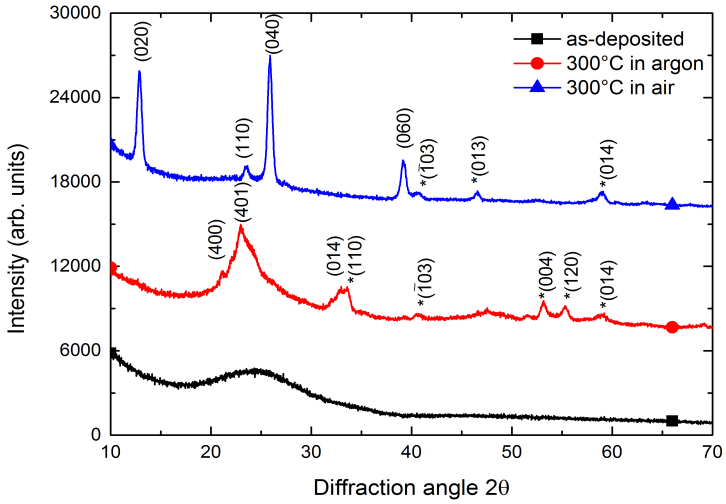

Figure 5.1: X-ray diffraction patterns of MoO_3 thin films, (black-square) as-deposited, (red-circle) annealed in argon, and (blue-triangle) annealed in air.

for an orthorhombic structure were determined from the relation

$$d_{hkl} = (h^2/a^2 + k^2/b^2 + l^2/c^2)^{-1/2} \tag{5.1.2}$$

where (hkl) are the Miller indices corresponding to the diffraction planes shown in Fig. 5.1. The obtained values were $a = 3.94$ Å, $b = 13.78$ Å, and $c = 3.70$ Å, while the interplanar distance for the most intense plane (040) resulted $d = 3.45$ Å. These values are in good agreement with the values reported on the JCPDS-ICDD card 05-0508, namely, $a = 3.96$ Å, $b = 13.85$ Å, $c = 3.69$ Å, and $d = 3.46$ Å.

5.1.2 HR-TEM of MoO_3

Exhibited in Fig. 5.2 is a HR-TEM image of a MoO_3 film annealed in air at 300°C. It is observed that the thermal treatment gives rise to crystalline domains immersed in the original amorphous structure. These domains reveal different crystallographic orientations and the crystallite size is slightly lower than 10 nm, in close agreement with the results obtained by the Scherrer's equation. The (040) planes of the α-

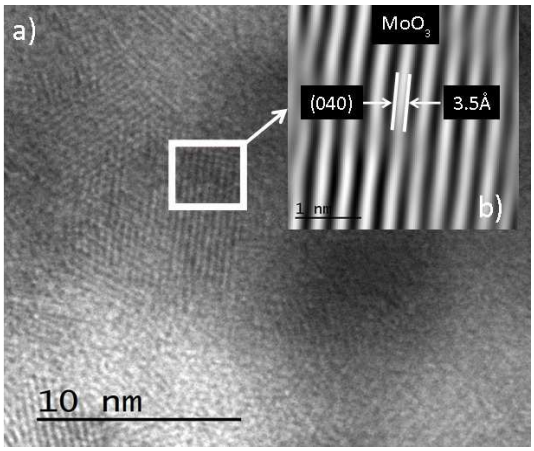

Figure 5.2: (a) HR-TEM image of a representative MoO_3 thin film annealed in air at 300°C. (b) An extended view of the image is shown in the inset.

MoO_3 phase are depicted in the inset of Fig. 5.2, where an interplanar distance of 3.5 Å is indicated.

5.1.3 Raman spectroscopy of MoO_3

The Raman spectra of representative MoO_3 thin films exposed to air, at different annealing temperatures, are presented in Fig. 5.3. In particular, the as-deposited sample and the films treated at 100 and 200°C share a number of features (see Fig. 5.3a). The peak centered at 995 cm^{-1} is associated with the Mo^{6+}=O stretching mode of terminal singly-coordinated oxygen atoms in the α-phase. These bonds have been claimed to be responsible for the layered structure of the α-MoO_3 phase [34]. As the annealing temperature increases, another shoulder emerges slightly at around 950 cm^{-1}. While this feature is also linked with terminal oxygen bonds, it has been ascribed to the breaking of Mo_2-O bonds at the corner-shared oxygens [127]. In addition, the peak at 663 cm^{-1} is related to the Mo_3-O stretching mode of the triply-coordinated oxygen atoms, which are shared by three octahedra [128]. Moreover, Lee *et al.* have assigned the peak at 400 cm^{-1} to vibrational bonds between Mo^{5+} and oxygen. Fig. 5.3b depicts the Raman spectra for the sample treated at 300°C in air and for the glass substrate. The intense peak at 819 cm^{-1}

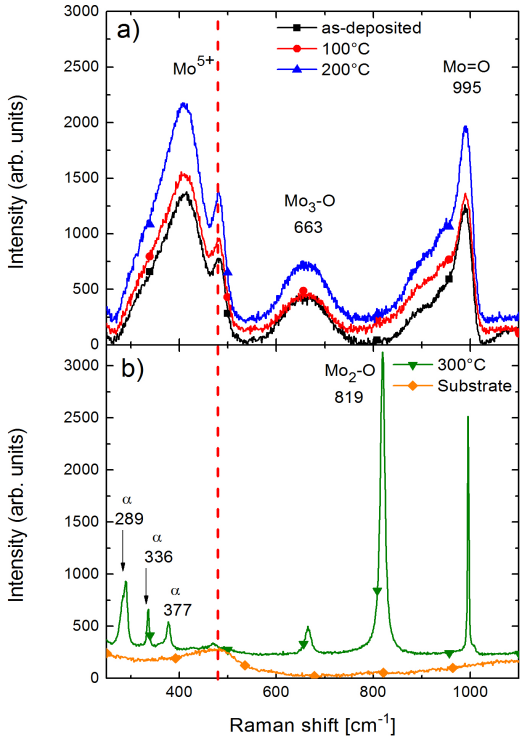

Figure 5.3: Typical Raman spectra for MoO_3 thin films treated in air at (a) 25 (as-deposited), 100, and 200, and (b) 300°C. The Raman spectrum of the substrate is also included.

is associated with the doubly coordinated oxygen (Mo_2-O) stretching mode and indicates a partial transition from β-MoO_3 to α-MoO_3 [129]. In the same spectrum, there are well-defined peaks within 280-380 cm^{-1} due to Raman-active bending modes, all of which are ascribed to the α-MoO_3 phase [124, 130, 131]. It is worth noting that the sample annealed at 300°C displays a high crystallinity, in accordance with our XRD measurements.

Fig. 5.4a displays the Raman spectra for the as-deposited films and for samples annealed in argon at 100 and 200°C. In essence, these spectra have similar characteristics as those of samples treated in air at corresponding temperatures. The main difference is observed in Fig. 5.4b, where the spectrum for the film annealed in argon at 300°C shows no well-defined peaks. In this case, the peak centered at 950

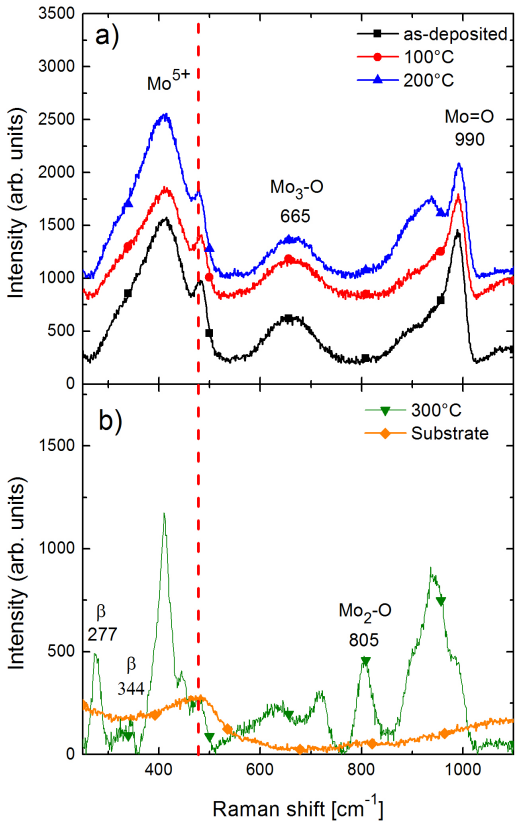

Figure 5.4: Typical Raman spectra for MoO_3 thin films treated in argon at (a) 25 (as-deposited), 100, and 200, and (b) 300°C. The Raman spectrum of the substrate is also included.

cm^{-1} becomes more intense than the peak at 995 cm^{-1}, indicating a decrease in singly-coordinated oxygens in the α-MoO_3 phase. Similarly, the peak at 805 cm^{-1} reveals a significant contribution from the doubly-coordinated oxygen stretching mode, whereas the weak peaks at 277 and 344 cm^{-1} are identified only with the β-MoO_3 phase [131–133].

5.1.4 AFM of MoO_3

Fig. 5.5 shows the surface morphology of MoO_3 thin films obtained by AFM. The changes in topography were caused by the thermal treatments. These changes were

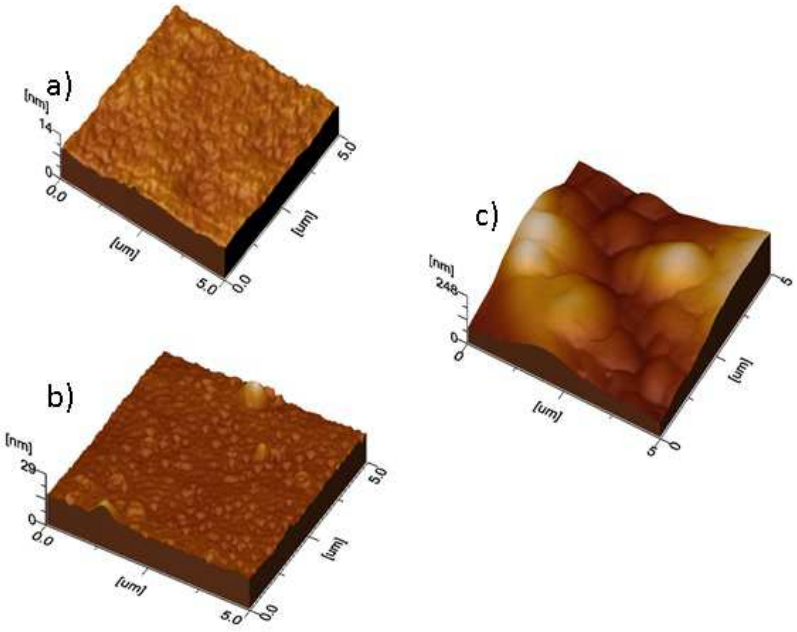

Figure 5.5: (a) AFM image of MoO_3 films deposited by reactive RF sputtering without heat treatment. (b) AFM image of MoO_3 films annealed at 300°C in argon. (c) AFM image of MoO_3 films annealed at 300°C in air.

quantified by using the WSxM 5.0 software. The average value for the RMS roughness and height were, respectively: ***(i)*** 0.85 nm and 3.56 nm, for the as-deposited film, ***(ii)*** 1.93 and 6.95 nm, for the film annealed in argon at 300°C, and ***(iii)*** 57.6 and 135.18 nm, for the film annealed in air at 300°C. This analysis confirms that the thermal treatments modify the topography of the MoO_3 thin films. In particular, the samples treated in air show a higher roughness than the samples treated in argon for identical annealing temperatures. These results are in agreement with results previously reported by our group [14].

5.1.5 UV-Vis-NIR spectroscopy of MoO_3

The optical absorption spectra for molybdenum oxide films annealed in air are illustrated in Fig.5.6a. These spectra show the fundamental absorption edge of MoO_3 around 400 nm besides the typical wide band extended from 500 nm to 1100 nm

associated with color center formation [14]. The coloration band increases with the annealing temperature and reaches a maximum when the treatment is carried out at 200°C; at this temperature, the films attain the so-called saturation state. In this range, the films turn dark blue. With further increase in temperature, the intensity of the coloration band decreases, in correspondence with a marked film bleaching. This outcome is related to the replenishment of anionic vacancies by oxygen supplied by the ambient and takes place along with a crystallization process [14]. Fig. 5.6b depicts the optical absorption spectra for MoO_3 films annealed in argon. In the temperature range 25-200°C, these spectra disclose a similar behavior as the spectra of samples treated in air; however, there is a noticeable difference when samples are exposed at higher temperatures in argon. Indeed, the coloration band remains essentially unaltered between 200 and 250°C, but it is greatly accentuated at 300°C, even revealing two different local maxima centered at approximately 550 and 900 nm. Additionally, the films annealed in argon above 250°C get a slight violet coloration, a distinctive property of the monoclinic Magneli phase Mo_9O_{26} films as indicated in the JCPDS-ICDD card 05-0441. The thermochromic response of the films was further evaluated by analyzing the evolution of the absorbance at a fixed wavelength (820 nm), close to the maximum of the coloration band, as a function of the annealing temperature. Shown in Fig. 5.6c are the results obtained for both types of annealing. As explained above, starting from the as-deposited materials, the absorbance grows as the temperature increases irrespective of the annealing atmosphere; however, the main difference occurs at temperatures over 200°C, where only the samples maintained in air become bleached.

The presence of discrete bands composing the broad coloration band has been previously studied by different authors. Indeed, upon irradiation of MoO_3 films with UV-light, Deb noted peaks at 500, 625, and 770 nm and attributed them to different color centers [10]. Hiruta et al. studied electrochemically-colored MoO_3 films and found that the coloration band consists of two different components: a) the so-called G-band, displayed at around 820 nm, which is the only component present in the

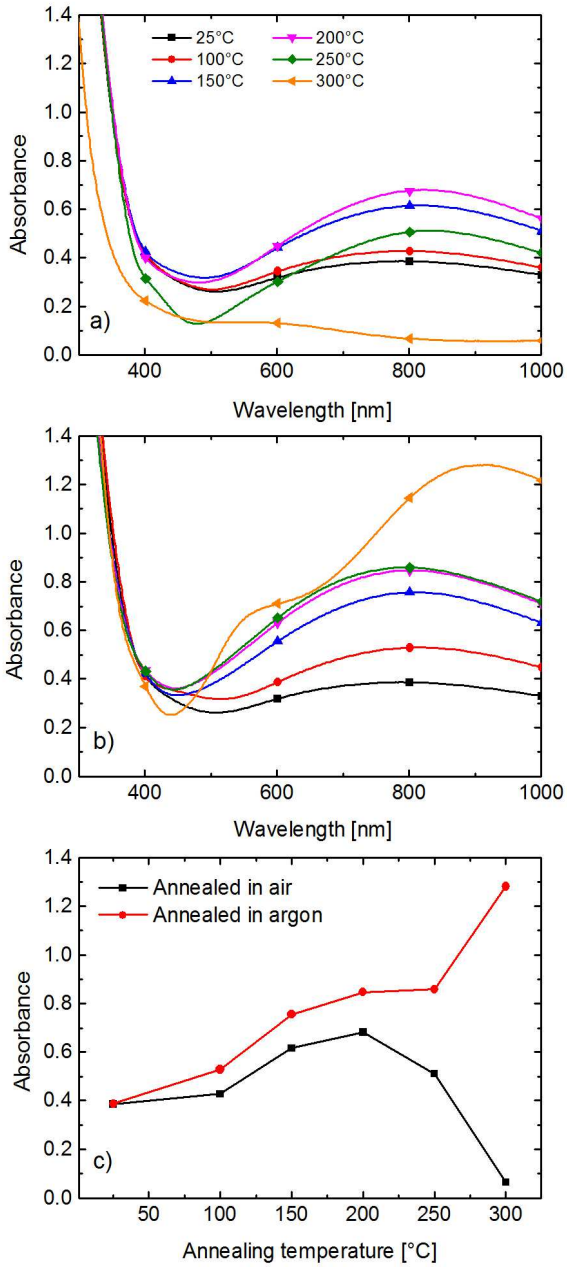

Figure 5.6: (a) Optical absorption spectra for MoO_3 thin films thermally treated in air. (b) Optical absorption spectra for MoO_3 thin films thermally treated in argon. (c) Absorbance values at 820 nm as a function of the annealing temperature for both atmospheres.

case of small charge insertion, and b) the second feature, known as T-band, appears at higher amounts of inserted charge and emerges as a shoulder between the G-band and the fundamental absorption band [134]. Dieterle *et al.* produced MoO_{3-x} samples under different temperature and gas atmosphere conditions and measured a combined coloration band; they accredited the constituent bands to ligand to metal charge transfer, d-d transitions, and intervalence charge transfer transitions [135]. Based on this information, we carried out a more detailed analysis of the coloration band using deconvolution methods. The coloration band was deconvolved assuming Gaussian band shapes for three different components ranging from 500-600, 800-900, and 900-1100 nm. These components were denoted as Peak 1, Peak 2, and Peak 3, respectively. Fig. 5.7a shows the results for the as-deposited MoO_3 film, indicating that the major contribution to the coloration band arises from Peak 2. This peak can be identified with an intervalence charge transfer transition of a hexacoordinated defect state labeled as $Mo^{5+}O_6$ [135]. The corresponding analysis for the sample annealed in argon at 300°C is included in Fig. 5.7b. In this case, the main contributions come from Peak 1 and Peak 2, with Peak 1 being ascribed to an oxygen vacancy defect state named as $Mo^{5+}O_5$. In both cases, Peak 3 had a negligible contribution to the convolved band. According to Dieterle **et al.**, the higher symmetry of the $Mo^{5+}O_6$ defect implies an energetically more favorable state due to a better charge compensation than the lower symmetry of $Mo^{5+}O_5$. This might be the reason why the band displayed in the near infrared region was the most intense component. Moreover, the appearance of a second band when samples are annealed in argon at 300°C is due to the presence of oxygen vacancies, which are not replenished as in the case of thermal treatments in air. It is known that disordered and amorphous materials produce localized states in the band gap resulting in an exponential absorption tail, *i.e.* Urbach tail, given by

$$\alpha = \alpha_0 \ \exp(\frac{h\nu}{E_e}) \tag{5.1.3}$$

where α_0 is a constant and E_e is an energy often interpreted as the tail width of

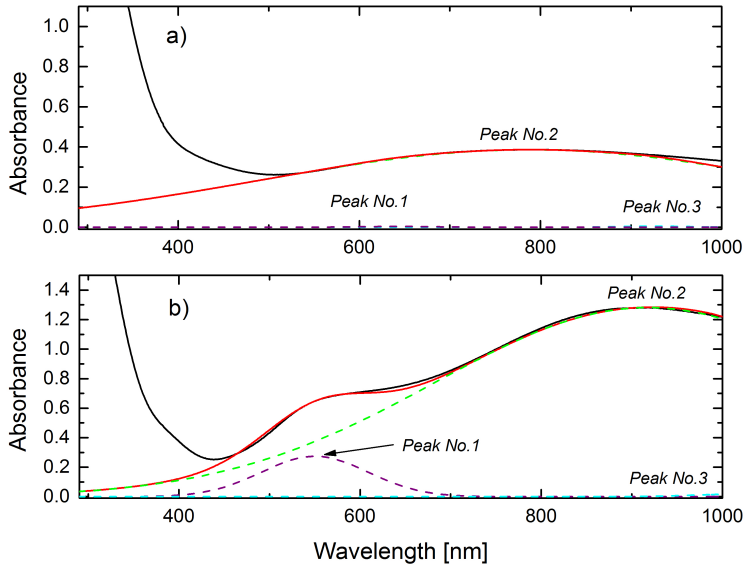

Figure 5.7: Optical absorption spectra of (a) a typical as-deposited MoO_3 film and (b) a MoO_3 film annealed at 300°C in argon. The plots also show the fitted curve (solid red line) and the resulting deconvolved peaks (dotted lines).

localized states in the forbidden band gap. From Urbach data, it is found that the Urbach slope decreases from 0.28 down to 0.25 eV^{-1} for the annealing in air, whereas for the annealing in argon the value 0.28 eV^{-1} remains approximately constant even at 300°C. These changes are associated with a decrease in disorder, in good agreement with the XRD data.

Shown in Fig. 5.8 are some parameters obtained from the deconvolution analysis. In particular, Fig. 5.8(a) depicts the position of the peak center as a function of the annealing temperature. All the peaks remain practically at the same wavelength up to 250°C; however, at 300°C, Peak 2 and Peak 3 move in opposite directions, being shifted towards higher and lower wavelengths, respectively. Fig. 5.8(b) displays the evolution of the area under the peak. A marked increase with the annealing temperature is observed for Peak 2. Finally, the evolution of the maximum absorbance for each peak is displayed in Fig. 5.8(c). Here, the steep increase of Peak 2 is again in accordance with data presented in Fig. 5.6(c).

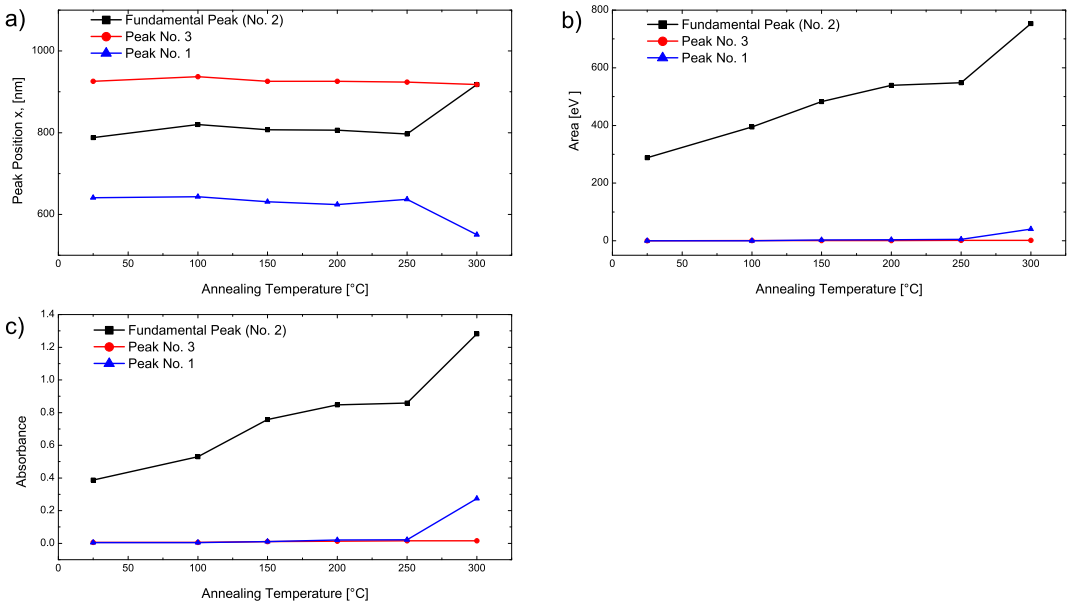

Figure 5.8: Deconvolution parameters as a function of the annealing temperature. (a) Position of the peak center. (b) Area under the curve. (c) Maximum absorbance.

5.1.6 XPS analysis of MoO_3

The film surface chemistry was analyzed by X-ray photoelectron spectroscopy. Exhibited in Fig. 5.9a is the high resolution XPS spectrum of the Mo 3d state for the as-deposited MoO_3 sample. This spectrum shows the spin-orbit splitting characteristic of Mo 3d levels. The Mo 3d core level spectrum was deconvolved into two doublets, each of them related to a specific oxidation state. The binding energies for the Mo $3d_{5/2}$ and Mo $3d_{3/2}$ peaks of the most intense doublet are 232.74 and 235.87 eV, respectively. The Mo $3d_{3/2}$ - Mo $3d_{5/2}$ separation is 3.13 eV and is associated with the Mo^{6+} oxidation state [90, 91, 136–141]. For the weaker doublet, the binding energies for the Mo $3d_{5/2}$ and Mo $3d_{3/2}$ peaks are 231.62 and 234.95 eV, respectively. In this case, the resulting energy separation was 3.33 eV, which is identified with the Mo^{5+} oxidation state [141]. It is important to remark that the intensity of the deconvolved Mo $3d_{5/2}$ and Mo $3d_{3/2}$ peaks of each doublet essen-

tially satisfied the theoretical ratio for their corresponding spin-orbit splitting, *i.e.* 3:2 for the 3d orbital [139]. Specifically, the values determined for the intensity ratio of the Mo^{6+} and Mo^{5+} oxidation states were 1.54 and 1.45, respectively, in agreement with values reported in the literature [139]. Fig. 5.9b shows XPS data for the sample annealed in air at 300°C. For this treatment, the doublet peaks identified with the Mo^{6+} oxidation state had an energy separation of 3.16 eV and an intensity ratio of 1.57. Corresponding values for the Mo^{5+} oxidation state were 3.33 eV and 1.53, respectively. Finally, the high resolution XPS spectrum for the film exposed to argon at 300°C is exhibited in Fig. 5.9c. In this case, the values determined for the energy separation for the doublet peaks of the Mo^{6+} and Mo^{5+} oxidation states were 3.13 and 3.29 eV, respectively. Furthermore, the respective intensity ratio was 1.55 and 1.59, respectively [139, 140]. As observed from these values, special attention has to be paid to the evolution of the Mo^{5+} oxidation state as the annealing temperature increases. To complement the XPS analysis, the position of the valence band maximum (VBM) was calculated by a linear extrapolation of the low binding energy of the valence band spectrum, as shown in Fig. 5.9d. The position of the VBM was 2.73 eV below the Fermi level, which is in agreement with previous reports [140, 142]. Fig. 5.10 displays the evolution of the ratio $A_i(T)/A_{25°C}$ as a function of the annealing temperature, T, where $A_i(T)$ is the area of the Mo^{5+} $3d_{3/2}$ component for a sample annealed at T and $A_{25°C}$ is the area of the corresponding peak for the as-deposited sample (T = 25°C). On the one hand, for the samples annealed in air, it is observed that the Mo^{5+} signal of the Mo $3d_{3/2}$ peak increases with the annealing temperature in the range 25 - 200°C, but it steeply decreases after this point. On the other hand, for the annealings in argon, a different behavior is found, since the Mo^{5+} oxidation state increases slightly in the whole analyzed range. These results are associated with a low disposal of oxygen vacancies in the film when the samples are thermally treated in air [137]. It is thus stated that the increase in the optical absorption is linked to the formation of the Mo^{5+} oxidation state.

The binding energies, obtained by deconvolution, for the Mo $3d_{5/2}$ and Mo

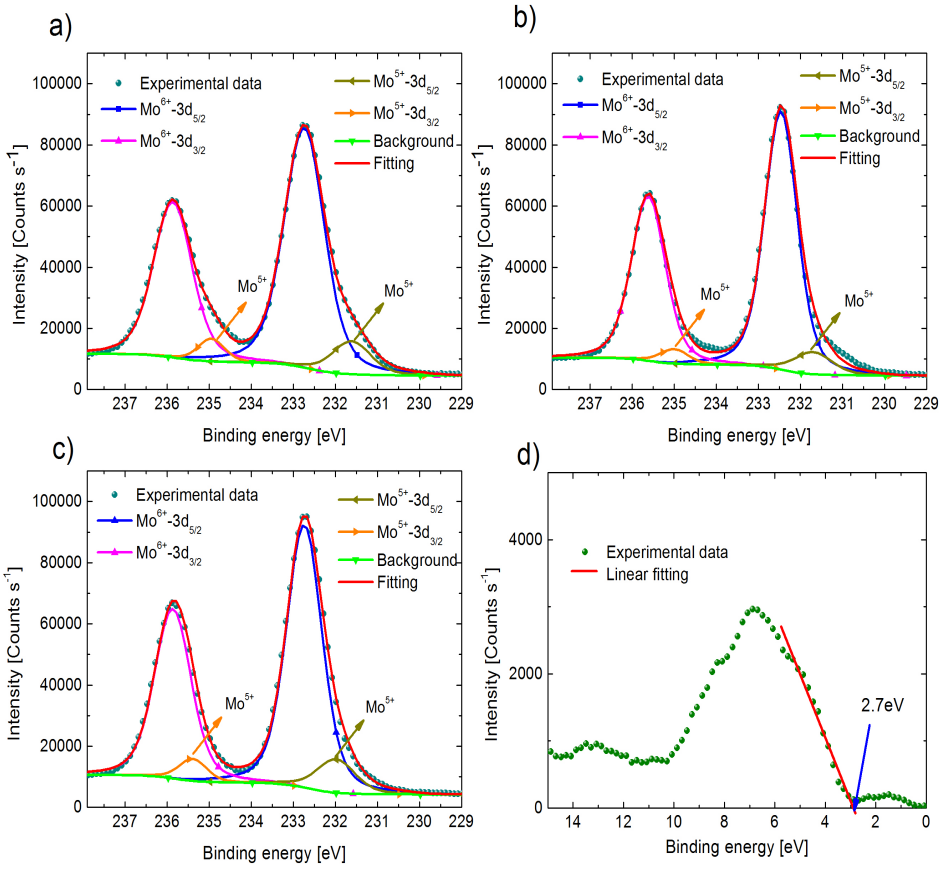

Figure 5.9: High resolution XPS spectra of the Mo 3d state showing the spin-orbit splitting. The deconvolved peaks associated with the $3d_{3/2}$ and $3d_{5/2}$ orbitals are also indicated. (a) as-deposited film, (b) sample annealed at 300°C in air, (c) sample annealed at 300°C in argon, and (d) valence band spectrum for a typical as-deposited film.

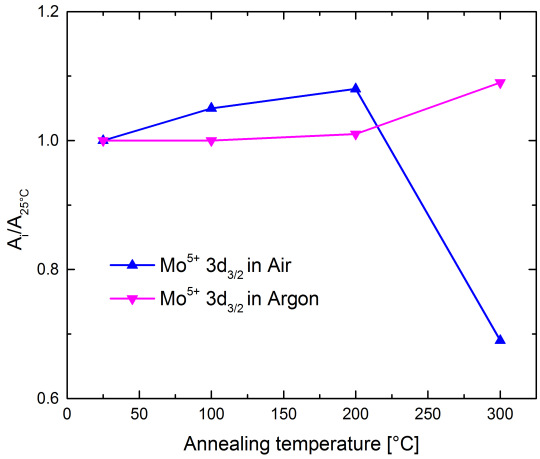

Figure 5.10: Evolution of the ratio $A_i(T)/A_{25°C}$ as a function of the annealing temperature. $A_i(T)$ is the area of the Mo^{5+} $3d_{3/2}$ component for a sample annealed at a given temperature and $A_{25°C}$ is the area of the corresponding peak for the as-deposited sample.

$3d_{3/2}$ orbitals corresponding to the Mo^{6+} and Mo^{5+} oxidation states are presented in Table 5.1.

In summary, it is shown that the evolution of the Mo^{5+} oxidation state is closely linked to the optical density, since both properties display the same dependence on the annealing temperature, irrespective of the investigated atmospheres.

5.2 Electrochromic effect of $W_{1-x-y}Ni_xTi_yO_3$ thin films

5.2.1 Elemental composition

Elemental compositions were determined by RBS performed at the Uppsala Tandem Laboratory using 2 MeV ^{4}He ions backscattered at an angle of 170°. Fig. 5.11 shows RBS spectra for two films prepared with different values of P_{Ni}/P_W and P_{Ni}/P_{W-Ti}. These data were fitted to a model of a film-substrate system by use of the SIMNRA

		Mo^{6+}		Mo^{5+}	
Condition	**Temperature**	**Mo3d$_{5/2}$**	**Mo3d$_{3/2}$**	**Mo3d$_{5/2}$**	**Mo3d$_{3/2}$**
	[°C]	[eV]	[eV]	[eV]	[eV]
As-deposited	25	232.74	235.87	231.62	234.95
	100	232.64	235.76	231.77	235.07
Air	200	232.75	235.89	231.79	235.12
	300	232.46	235.62	231.70	235.00
	100	232.81	235.97	231.80	235.10
Argon	200	232.75	235.89	231.88	235.10
	300	232.74	235.87	231.90	235.19

Table 5.1: Position of the different oxidation states Mo^{6+} and Mo^{5+} for the Mo $3d_{5/2}$ and Mo $3d_{3/2}$. Obtained by a deconvolution analysis.

program [120]. It is apparent that spectral features can be unambiguously assigned to various elements and that the films' compositions are uniform over their cross-sections. Specifically, the two films are reported on in Fig. 5.11 (a) and (b) and consisted of $W_{0.88}Ni_{0.12}O_{2.94}$ and $W_{0.46}Ni_{0.37}Ti_{0.17}O_{2.87}$, respectively.

Film composition was investigated as a function of P_{Ni}/P_{W-Ti} ratio and Fig. 5.12 shows values of x and δ of samples represented as $W_{0.83-x}Ni_xTi_{0.17}O_{3-\delta}$. It is apparent that the Ni content is $0 < x < 0.4$ depending on sputter conditions and, expectedly, grows monotonically as P_{Ni}/P_{W-Ti} is increased. The oxygen content can be described by the magnitude of δ which is seen to increase from ∼0.05 to ∼0.2 as x goes from zero to ∼0.4. Thus the metal/oxygen atomic ratio stays rather close to 3 and our data justify that, for the sake of simplicity, the specific value of δ is suppressed in the following discussion of our films.

5.2.2 XRD of $W_{1-x-y}Ni_xTi_yO_3$ thin films

Structural characterization was accomplished by x-ray diffraction (XRD) using a Siemens D5000 instrument operating with CuK_α radiation at a wavelength of 1.54

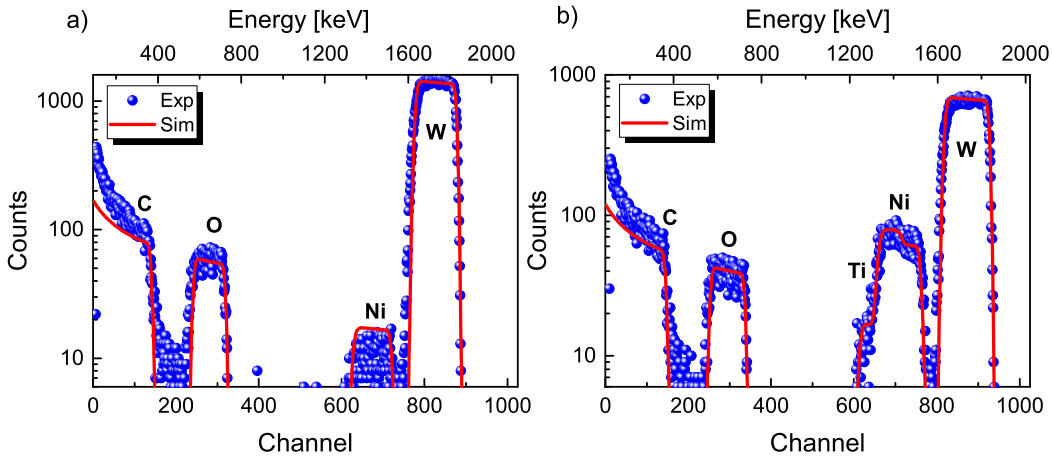

Figure 5.11: RBS spectra, showing number of counts per energy channel, for ∼300-nm-thick films of (a) W-Ni oxide and (b) W-Ni-Ti oxide made by sputter deposition with $P_{Ni}/P_W \approx 0.3$ and $P_{Ni}/P_{W-Ti} \approx 0.78$, respectively. Symbols denote experimental (exp) data and curves were simulated (sim) from the SIMNRA program. The various peaks were assigned to the shown elements.

Å. Fig. 5.13(a) displays XRD data for as-deposited and annealed WO_3 films. The as-deposited film showed nothing but peaks due to the ITO layer and no evidence was found for features associated with any crystalline phase of tungsten oxide. Hence this film is amorphous. The annealed sample, on the other hand, formed a crystalline monoclinic structure. Fig. 5.13(b) reports on a $W_{0.67}Ni_{0.16}Ti_{0.17}O_3$ film in as-deposited and annealed states and proves that the sample remains amorphous after annealing. Similar results were found for all of the W-Ni-Ti oxides studied in this work. The fact that Ti addition tends to stabilize an amorphous structure in W-oxide-based films is consistent with previous results [13, 64].

5.2.3 Electrochemical experiments of $W_{1-x-y}Ni_xTi_yO_3$ thin films

The W-oxide-based films were investigated by cyclic voltammetry (CV) using a computer-controlled ECO Chemie Autolab/GPES interface in a three-electrode electrochemical cell with the sample as working electrode and Li foils serving as reference and counter electrodes. The electrolyte was 1 M $LiClO_4$ in propylene carbonate (Li-

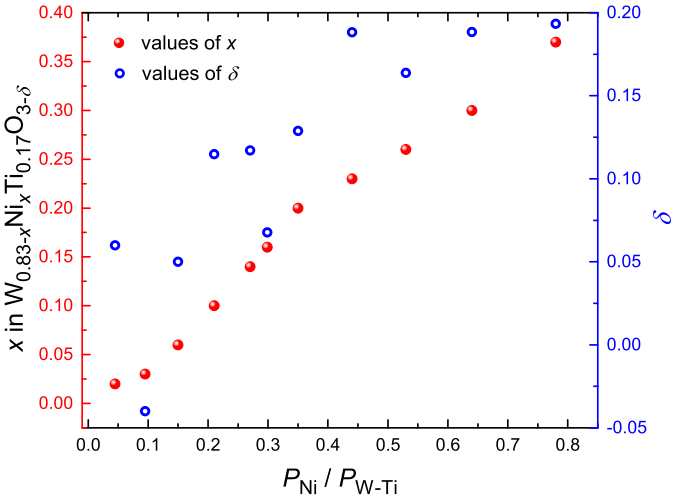

Figure 5.12: Nickel content x (red dots, left-hand scale) and oxygen sub-stoichiometry δ (blue circles, right hand scale) in thin films of $W_{0.83-x}Ni_xTi_{0.17}O_{3-\delta}$ prepared by sputter deposition from targets of Ni and W-Ti at the shown power ratios P_{Ni}/P_{W-Ti}.

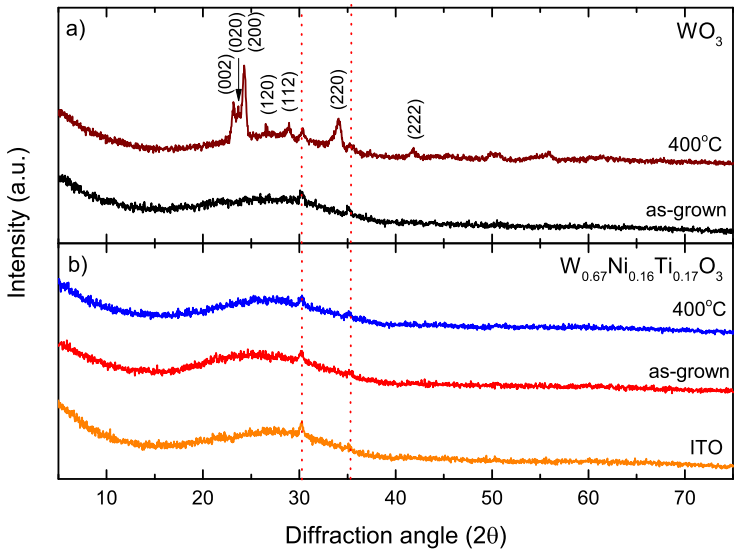

Figure 5.13: X-ray diffractograms for films of the shown compositions in as-deposited and after annealing at 400°C. (a) correspond to pure tungsten oxide and (b) for $W_{0.67}Ni_{0.16}Ti_{0.17}O_3$. The (**hkl**) indices match to the monoclinic phase of WO_3. The dotted line indicate the diffraction peaks due to ITO.

PC). All measurements took place inside a glovebox with inert argon atmosphere. The voltage range and sweep rate were 1.7-4 V *vs.* Li/Li^+ and 10 mV/s, respectively. This voltage range was chosen in order to produce rapid degradation of the films. Fig. 5.14 shows CV data for films with various compositions at selected cycle numbers. The films of WO_3, $W_{0.88}Ni_{0.12}O_3$ and $W_{0.88}Ni_{0.12}Ti_{0.10}O_3$ display poor electrochemical stability during 100 CV cycles, whereas the $W_{0.67}Ni_{0.16}Ti_{0.17}O_3$ sample clearly was more durable. Quantitative information on the degradation was obtained by plotting extracted and inserted charge density Q as a function of the number of CV cycles. This evolution is illustrated in Fig. 5.15(a) which confirms that the $W_{0.67}Ni_{0.16}Ti_{0.17}O_3$ sample retains its charge capacity to a higher degree than the other films, at least after the first 40 CV cycles. It is also illustrative to show the modifications in the charge capacity by plotting the cycle-dependent difference between extracted and inserted charge density $\delta Q = Q_{inserted} + Q_{extracted}$, with $Q_{inserted} < 0$ and $Q_{extracted} > 0$, as reported in Fig. 5.15(b). The Ti-free samples display pronounced peaks in δQ, whereas no such feature is apparent for the other films.

5.2.4 Optical transmittance of $W_{1-x-y}Ni_xTi_yO_3$ thin films

Optical transmittance T was recorded in situ at a mid-luminous wavelength of 550 nm during CV cycling, using an Ocean Optics fiber-optic instrument, for the various W-oxide-based films. Fig. 5.16(a) shows transmittance in bleached and colored states denoted T_b and T_c, respectively, for the same selected CV cycles as in Fig. 5.15. The WO_3 film suffers an abrupt decrease of its transmittance modulation, defined as $\Delta T = T_b - T_c$, as depicted in Fig. 5.16(b). This tendency is similar, albeit less marked, for the W-Ni oxide film. The Ti-containing films have lower values of ΔT during the initial CV cycles, but the cycle-dependent decline of ΔT is less rapid than for the other films, and the $W_{0.67}Ni_{0.16}Ti_{0.17}O_3$ sample shows the largest optical modulation after ~ 60 CV cycles.

The color of the CV cycled films is an important feature for practical ap-

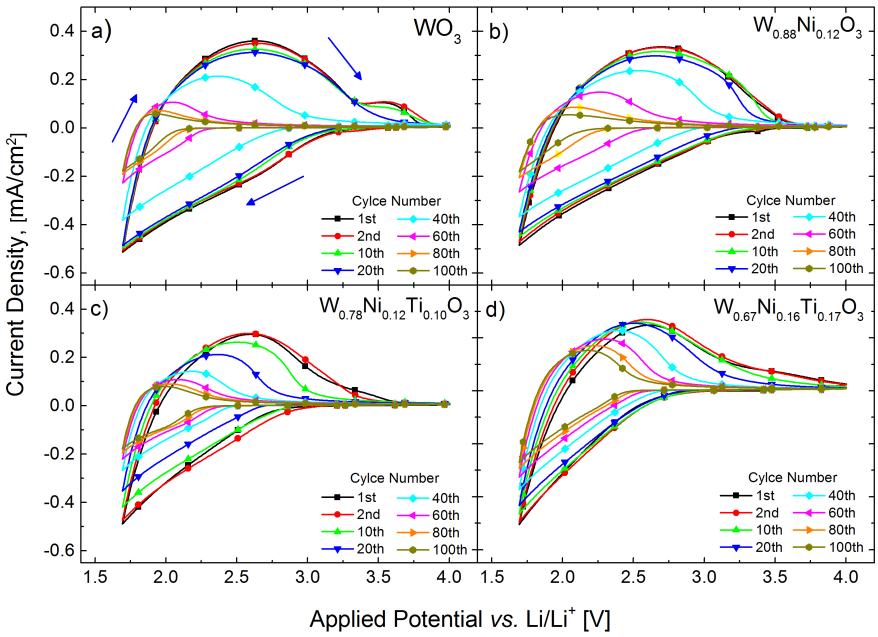

Figure 5.14: Cyclic voltammograms for (a) W oxide, (b) W-Ni oxide, and (c)-(d) W-Ni-Ti oxide films of the shown compositions immersed in 1M Li-PC. Data were taken after the indicated numbers of cycles for the voltage sweep range 1.7-4.0 V *vs.* Li/Li^+. Arrows indicate the direction of insertion and extraction of charge.

plications. This color was found to be brownish-yellowish, which is typical for samples that have undergone several CV cycles in a large potential voltage window in a Li-PC electrolyte [13]. Interestingly, this tint was less marked for the $W_{0.67}Ni_{0.16}Ti_{0.17}O_3$ sample than for the other films. As a complement to the optical and electrochemical characterization, we calculated the coloration efficiency defined by $\eta = \ln(T_b/T_c)/\Delta Q$, where ΔQ is the inserted charge density. Fig. 5.17 shows data on η as a function of cycle number and indicates that W-Ni oxide gives superior results thereby confirming results in a previous article [57]. Ti incorporation into W-Ni oxide lowers η, but it is important to keep in mind that a sufficient Ti content produces superior electrochemical durability and color rendering. A trade-off might be reached with regard to the composition, and to this end we now consider the

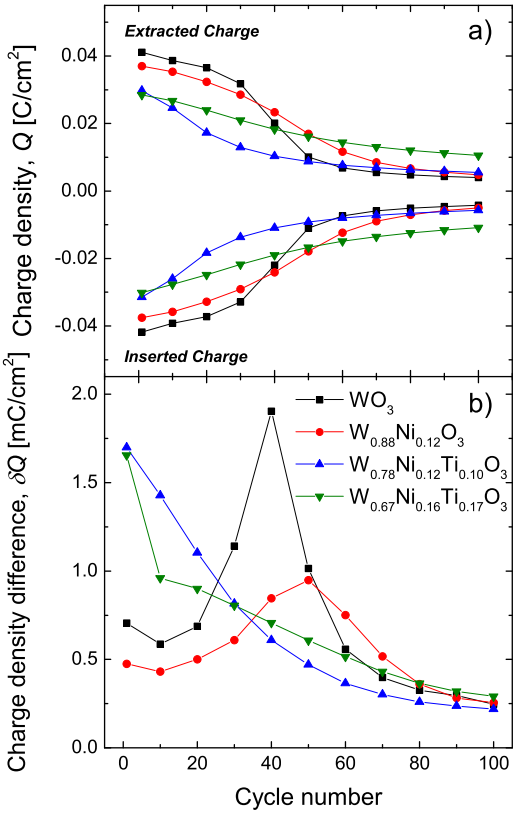

Figure 5.15: (a) Extracted and inserted charge density during voltammetric cycling of films with the shown compositions, and (b) difference in charge density for successive charge extractions and insertions. Symbols indicate data and lines were drawn for convenience.

effect of varying Ni contents in films of $W_{0.83x}Ni_xTi_{0.17}O_3$.

5.2.5 Enhancement of CE and durability of $W_{0.83-x}Ni_xTi_{0.17}O_3$

Fig. 5.18 displays CV data for films of $W_{0.83-x}Ni_xTi_{0.17}O_3$ with six values of x in the range $0.02 \leq x \leq 0.37$ and using the earlier potential range and voltage scan rate; data for $x = 0.16$ (*i.e.*, for $W_{0.67}Ni_{0.16}Ti_{0.17}O_3$) were presented above. As before, the charge capacity drops monotonically when the cycle number is increased. Furthermore, the cyclic voltammograms alter their shapes, especially for $x \geq 0.2$,

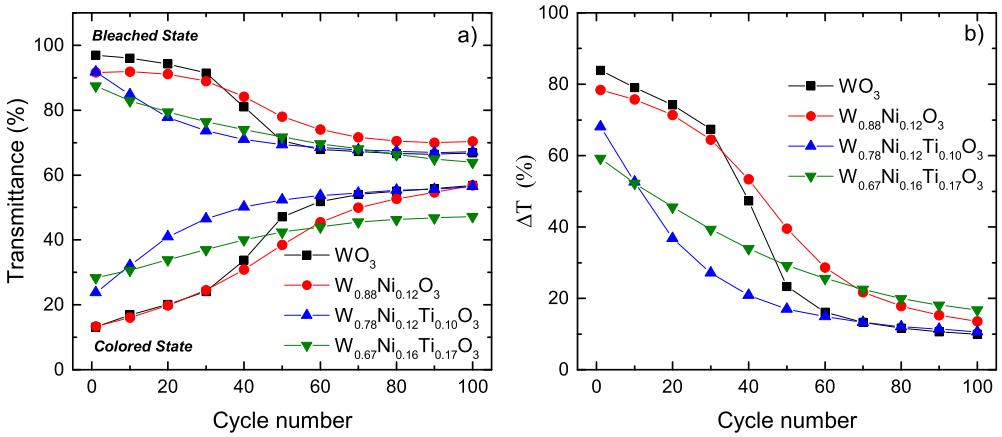

Figure 5.16: (a) Evolution of transmittance at the wavelength 550 nm in the bleached and colored states for films with the shown compositions. (b) Evolution of $\Delta T = T_b$-T_c as a function of cycle number, where T_b is the bleached state and T_c is the colored state with the shown compositions. The films were immersed in 1M Li-PC and studied as a function of cycle number.

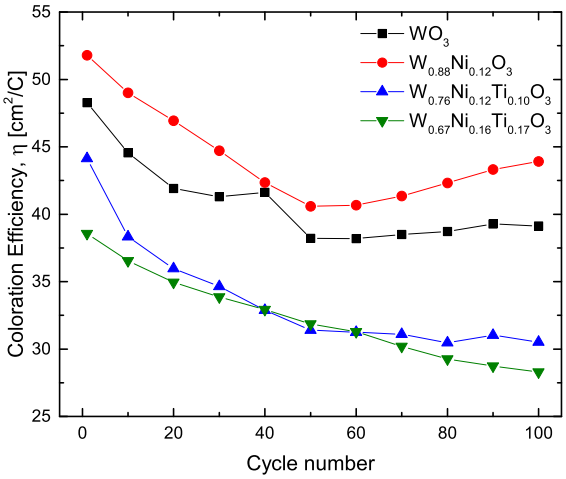

Figure 5.17: Evolution of coloration efficiency at the wavelength 550 nm from as-deposited films with the shown compositions during voltammetric cycling in a Li-PC electrolyte. Symbols indicate data and were joined by lines for convenience.

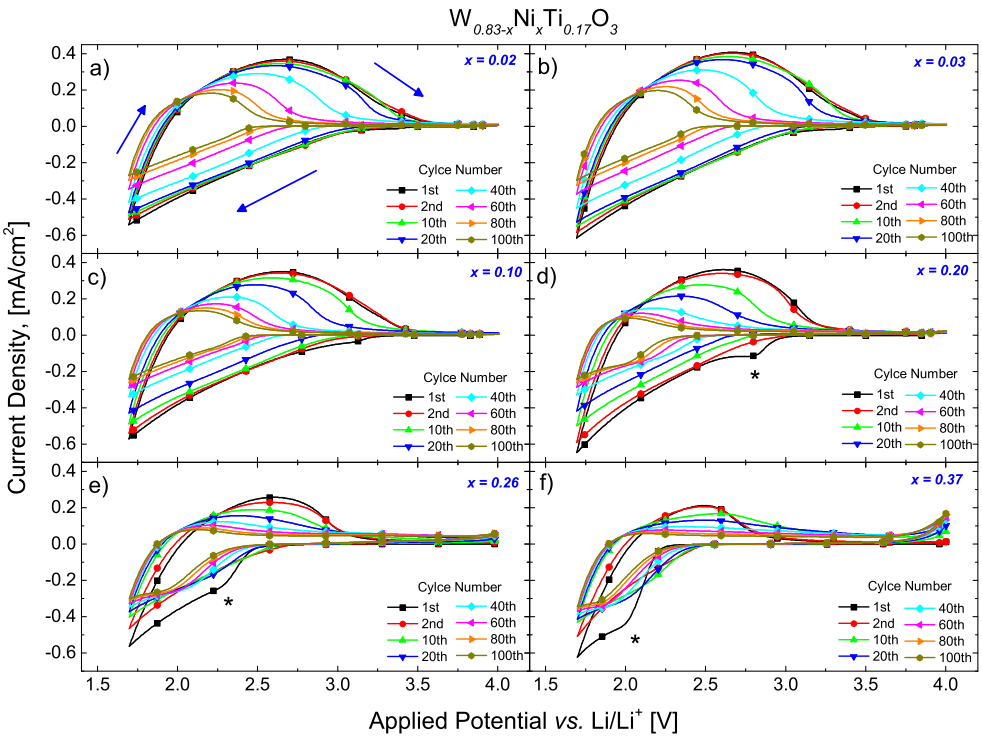

Figure 5.18: Cyclic voltammograms for (a)-(f) W-Ni-Ti oxide films of the shown compositions immersed in 1M Li-PC. Data were taken after the indicated numbers of cycles for the voltage sweep range 1.7-4.0 V *vs.* Li/Li^+. Arrows indicate the direction of insertion and extraction of charge. Asterisks mark "shoulders" in the data.

and a "shoulder" develops for the sweep towards lower potentials as marked with asterisks in Fig. 5.18(d)-(f). This "shoulder" is conspicuous only in the first cycle and shifts towards lower potentials as the Ni content is raised. It is hence evident that an irreversible reaction occurs during the first coloration cycle.

The onset of optical absorption depends on x in an interesting way, as elaborated in Fig. 5.19 for the four first CV cycles, and the lowering of T commences in sweeps towards lower potentials at voltages that occur at a progressively smaller value as x is increased. Strikingly, the potential for the onset of optical absorption during the first CV cycle seems to coincide with the position of the "shoulder" in

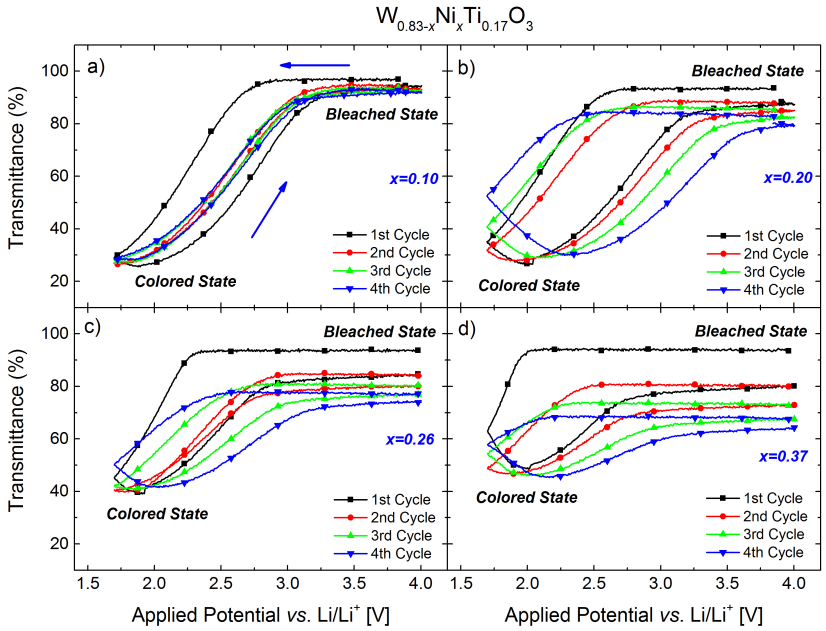

Figure 5.19: Evolution of transmittance as a function of applied potential for W-Ni-Ti oxide films of the shown compositions immersed in 1M Li-PC. Data were taken during the first cycle for the voltage sweep range 1.7-4.0 V *vs.* Li/Li^+. Arrow on the top indicated the direction of insertion charge and arrow on bottom indicated the extraction of charge.

the CV data. These data point at major changes of the electronic structure when the Ni content is increased, but the results do not permit an in-depth analysis on this matter. Fig. 5.19 also highlights that the potential sweeps towards higher values is unable to fully restore the initial transparent states of the films when $x > 0.1$. The transmittance modulation is small for $x \geq 0.20$ and these samples gradually lose their high bleached-state transmittance which indicates that irreversible electrochemical processes continue to occur.

Fig. 5.20 is analogous to Fig. 5.15, and panels (a)-(b) display the capacity for charge insertion and extraction as a function of cycle number for $W_{0.83x}Ni_xTi_{0.17}O_3$ films with different contents of Ni, while panels (c)-(d) show the difference in charge density between successive charge insertions and extractions. It is evident that, after

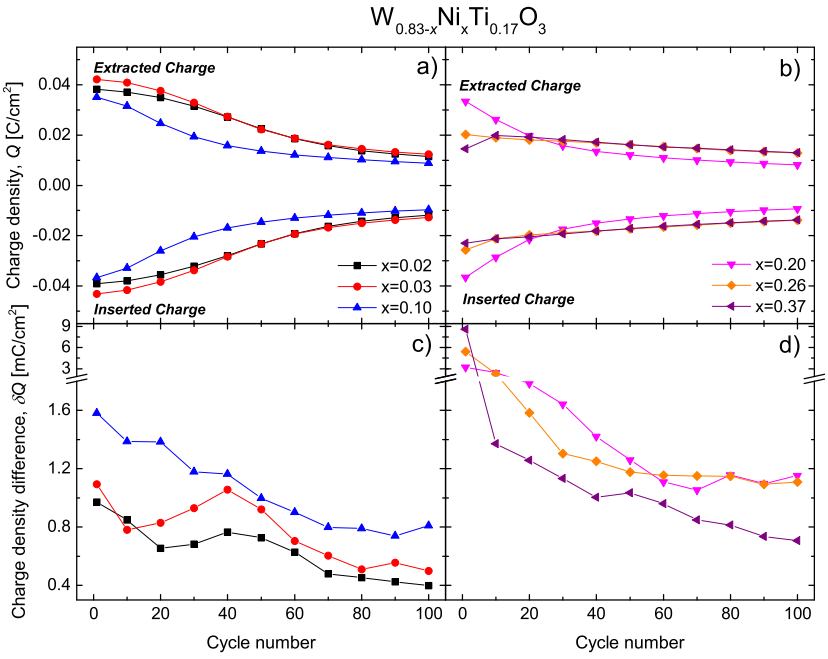

Figure 5.20: (a) Extracted and inserted charge density during voltammetric cycling of films with the shown compositions, and (b) difference in charge density for successive charge extractions and insertions. Symbols indicate data and lines were drawn for convenience.

a rapid initial evolution of δQ, this parameter stabilizes at ~ 1 mC/cm^2 after some 60 CV cycles for the approximate range $0.1 < x < 0.3$.

The degradation of the films is also manifested in their optical properties, as evident from Fig. 5.21, which is analogous to Fig. 5.16 above. Expectedly, the optical modulation is largest for small Ni contents, and it is seen that $\Delta T < 10\%$ after 60 CV cycles for $x > 0.20$.

Fig. 5.22 delineates the coloration efficiency for $W_{0.83x}Ni_xTi_{0.17}O_3$ thin films as a function of the number of CV cycles in the same fashion as in Fig. 5.17. Again, we note that the magnitude of x is of great importance and, generally speaking, η drops when x is increased. Specifically, we find that $\eta < 20$ cm^2/C after 40 CV cycles for $x > 0.20$.

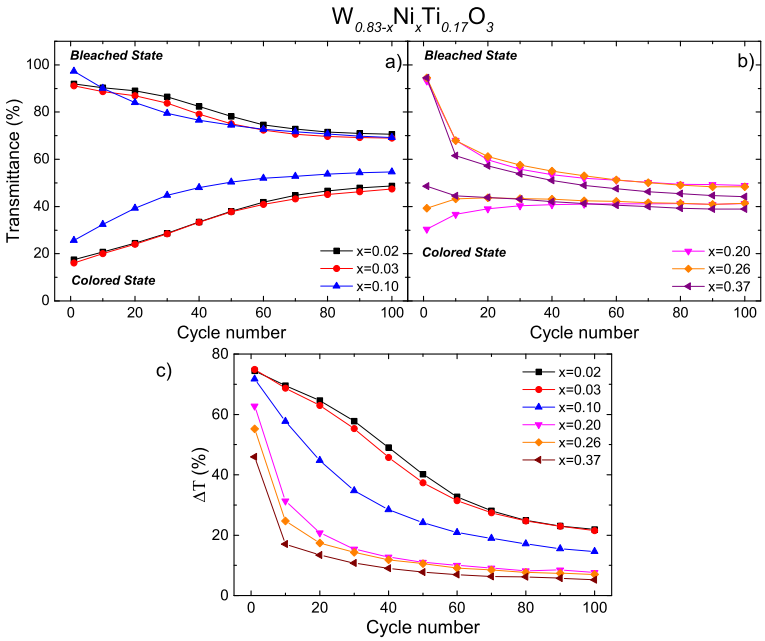

Figure 5.21: (a) Evolution of transmittance at the wavelength 550 nm in the bleached and colored states for W-Ni-Ti oxides at Ni content ∼2, ∼3 and ∼10at.%, (b) Evolution of transmittance at the wavelength 550 nm in the bleached and colored states for W-Ni-Ti oxides at Ni content ∼20, ∼26 and ∼37at.%, (c) Evolution of $\Delta T = T_b - T_c$ as a function of cycle number, where T_b is the bleached state and T_c is the colored state with the shown compositions.

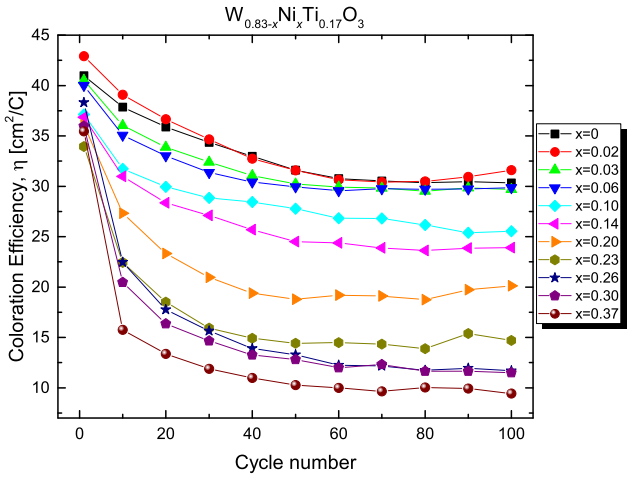

Figure 5.22: Evolution of coloration efficiency at the wavelength 550 nm for films with the shown compositions. The films were immersed in 1M Li-PC and studied as a function of cycle number.

6

Conclusions

MoO_3 thin films were deposited by rf reactive magnetron sputtering from a metallic target of molybdenum. The thermochromic response of the films showed a dependence on the annealing temperature and atmosphere. When films were thermally treated in argon, the films formed color centers even at 300°C. On the contrary, the films annealed in air reached a saturated coloration at around 200°C and become bleached at higher annealing temperatures. Raman spectroscopy allowed to identify the formation of Mo^{5+} oxidation states. In addition, it was found that treatments in different atmospheres cause distinct structural features in the material. As confirmed by HRTEM, samples treated in air showed a preferred orientation of the planes (*0k0*), while films treated in argon showed a preferred orientation of the planes (110) and (111). The XPS analysis showed the evolution of the Mo^{5+} oxidation states as a function of the annealing temperature, in agreement with the findings by Raman spectroscopy.

With regard to the electrochromism of W and W-Ni oxide thin films, these materials suffered clear deterioration in their electrochromic properties after 50 voltammetric cycles in a wide voltage range (1.7-4 V *vs.* Li/Li^+) but an addition of ∼17at.% of Ti improves the stability considerably. On the other hand, the Ti content diminished the coloration efficiency. The second part of this study successfully identified the range of nickel concentrations where films exhibited the highest durability. More-

over, it was possible to increase the coloration efficiency of the $W_{0.83-x}Ni_xTi_{0.17}O_3$ sample.

7

Articles list

1. M.A. Arvizu, M. Morales-Luna, S. A. Tomás, P. Rodríguez, and O. Zelaya-Angel. Photochromism and thermochromism of MoO_3 thin films doped with ZnSe.*AIP Conference Proceedings* **1420**:151-156 (2012).

2. M.A. Arvizu, S.A. Tomás, M. Morales-Luna, J. Santoyo-Salazar, J.O. García-Torija and O. Zelaya-Angel. Effect of a ZnSe layer on the thermochromic properties of MoO_3 thin films. *Int. J. Thermophys* **33**:20352040 (2012).

3. M. Pérez-González, S.A. Tomás, M. Morales-Luna, M.A. Arvizu and M.M. Tellez-Cruz. Optical, structural, and morphological properties of photocatalytic TiO_2-ZnO thin films synthesized by the sol-gel process. *Thin Solid Films* **594**:304 309 (2015).

4. R.-T. Wen, M.A. Arvizu, M. Morales-Luna, C.G. Granqvist and G.A. Niklasson. Ion trapping and detrapping in amorphous tungsten oxide thin films observed by real-time electro-optical monitoring. *Chem. Mater.* **28**:4670-4676 (2015).

5. M. Morales-Luna, M.A. Arvizu, C.G. Granqvist and G.A. Niklasson. Sputter deposited $W_{1-x-y}Ni_xTi_yO_3$ thin films: Electrochromic properties and durability. *Journal of Physics* **682**:012021-6 (2016).

6. M. Morales-Luna, M.A. Arvizu, C.G. Granqvist, G.A. Niklasson. Electrochromic properties of $W_{1-x-y}Ni_xTi_yO_3$ thin films made by DC magnetron sputtering. *Thin Solid Films* **615**:292299 (2016).

7. M.A. Arvizu, M. Morales-Luna, M. Pérez-González, E. Campos-Gonzalez, O. Zelaya-Angel, S.A. Tomás. Influence of thermal annealings in argon on the structural and thermochromic properties of MoO_3 thin films. *Int. J. Thermophys* **38**:51 (2017).

8. M. Pérez-González, S.A. Tomás, J. Santoyo-Salazar, M. Morales-Luna. Influence of deposition conditions on the photocatalytic activity of TiO_2-ZnO thin films deposited by dc reactive magnetron sputtering. *Ceramics International* **under review**.

9. M. Morales-Luna, S.A. Tomás, M.A. Arvizu, M. Pérez-González, E. Campos-Gonzalez. The evolution of the Mo^{5+} oxidation state in the thermochromic effect of MoO_3 thin films deposited by rf magnetron sputtering. *J. Alloys Compd.* **under review**.

Bibliography

[1] G.B. Smith and C.G. Granqvist. *Green Nanotechnology*. CRC-Press, 2011.

[2] B. Metz, O. Davidson, H.C. de Coninck, M. Loos, and L.A. Meyer (eds.) IPCC. *IPCC Special Report on Carbon Dioxide Capture and Storage. Prepared by Working Group III of the Intergovernmental Panel on Climate Change*. Cambridge University Press, 2005.

[3] S. Pacala and R. Socolow. *Strong influence of substrate temperature on the growth of nanocrystalline MoO_3 thin films. Science*, **305**:968–972, (2004).

[4] C.G. Granqvist. *Stabilization Wedges: Solving the Climate Problem for the Next 50 Years with Current Technologies. Thin Solid Films*, **564**:1–38, (2014).

[5] C.G. Granqvist, S. Green, G.A. Niklasson, N.R. Mlyuka, S. von Kræmer, and P. Georén. *Advances in chromogenic materials and devices. Thin Solid Films*, **518**:3046–3053, (2010).

[6] UNEP. *Buildings and Climate Change: Summary for Decision-Makers*. United Nations Environment Programme, 2009.

[7] C.M. Lampert. *Chromogenic Smart Materials. Materials Today*, **7**:28–35, (2004).

[8] C.G. Granqvist. *Electrochromism and smart window design. Solid State Ionics*, **53-56**:479–489, (1992).

[9] M. Ferrara and M. Bengisu. *Intelligent design with chromogenic materials. Journal of the International Colour Association*, **13**:54–66, (2014).

[10] S.K. Deb and J.A. Chopoorian. *Optical Properties and Color-Center Formation in Thin Films of Molybdenum Trioxide. Journal of Applied Physics*, **37**:4818, (1966).

[11] R.J. Colton R. J., A.M. Guzman, and J.W. Rabalais. *Photochromism and Electrochromism in Amorphous Transition Metal Oxide Films. Accounts of Chemical Research*, **11**:170–176, (1978).

[12] C.G. Granqvist. *Handbook of Inorganic Electrochromic Materials.* Elsevier, 1995.

[13] M.A. Arvizu, C.A. Triana, B.I. Stefanov, C.G. Granqvist, and G.A. Niklasson. *Electrochromism in sputter-deposited W-Ti oxide films: Durability enhancement due to Ti. Solar Energy Materials & Solar Cells*, **125**:184–189, (2014).

[14] S.A. Tomas, M.A. Arvizu, O. Zelaya-Angel, and P. Rodríguez. *Effect of ZnSe doping on the photochromic and thermochromic properties of MoO_3 thin films. Thin Solid Films*, **518**:1332–1336, (2009).

[15] S. Green, J. Backholm, P. Georén, C.G. Granqvist, and G.A. Niklasson. *Electrochromism in nickel oxide and tungsten oxide thin films: Ion intercalation from different electrolytes. Solar Energy Materials & Solar Cells*, **93**:2050–2055, (2009).

[16] P.C. Lansåker, J. Backholm, G.A. Niklasson, and C.G. Granqvist. *$TiO_2/Au/TiO_2$ multilayer thin films: Novel metal-based transparent conductors for electrochromic devices. Thin Solid Films*, **518**:1225–1229, (2009).

[17] C.N.R. Rao. *Transition Metal Oxides. Annu. Rev. Phys. Chern.*, **40**:291–326, (1989).

[18] L.E. Orgel. *Introduction to Transition-Metal Chemistry: Ligand-Field Theory.* Methuen & Co. LTD, 1966.

[19] P.A. Cox. *Transition Metal Oxides.* Oxford, 1992.

[20] M. Morales Luna. *Efecto de una Intercapa de CdSe en las Propiedades Cromogénicas de Películas Delgadas de MoO_3. M.Sc. Thesis (in Spanish).* CINVESTAV-IPN, 2011.

[21] M.A. Arvizu. *Synthesis and characterization of MoO_3 and WO_3 thin films. Study of their chromogenic properties. PhD Thesis.* CINVESTAV-IPN, 2014.

[22] T. He and J. Yao. *Photochromism of molybdenum oxide. Journal of Photochemistry and Photobiology C: Photochemistry Reviews*, **4**:125–143, (2003).

[23] S.K. Deb. *Physical properties of a transition metal oxide: optical and photoelectric properties of single crystal and thin film molybdenum trioxide. Proccedings of the Royal Society of London A*, **304**:211–231, (1968).

[24] B.W. Faughnan, R.S. Crandall, and P.M. Heyman. *Electrochromism in WO_3 amorphous films. RCA Rev*, **36**:177–197, (1975).

[25] O.F. Schirme, V. Wittwer, G. Baur, and G. Brandt. *Dependence of WO_3 Electrochromic Absorption on Crystallinity. J. Electrochem. Soc.: Solid state science and technology*, **124**:749–753, (1977).

[26] B.W. Faughnan and R.S. Crandall. *Optical properties of mixed oxide WO_3/MoO_3 electrochromic films. Appl. Phys. Lett.*, **31**:834, (1977).

[27] T. He and J. Yao. *Photochromism in composite and hybrid materials based on transition-metal oxides and polyoxometalates. Progress in Materials Science*, **51**:810–879, (2006).

[28] J.N. Yao and B.H. Loo. *Improved Visible-Light Photochromism in Au/MoO_3SnO_2 Thin Films. Solid State Communications*, **105**:479–480, (1998).

[29] M. Fujii, T. Kawai, H. Nakamatsu, and S. Kawai. *Photoinduced Colour Transformation in WO_3 Particles. J. Chem. Soc. Chem. Commun.*, **105**:1428, (1983).

[30] M.A. Quevedo-Lopez, R. Ramirez-Bon, R.A. Orozco-Teran, O. Mendoza-Gonzalez, and O. Zelaya-Angel. *Effect of a CdS interlayer in thermochromism and photochromism of MoO_3 thin films. Thin Solid Films*, **343-344**:202–205, (1999).

[31] G. Perna, V. Capozzi, M. Ambrico, V. Augelli, T. Ligonzo, A. Minafra, L. Schiavulli, and M. Pallara. *Structural and optical characterization of Zn doped CdSe films. Applied Surface Science*, **233**:366–372, (2004).

[32] C. Sanchez, B. Lebeau, F. Ribot, and M. In. *Molecular Design of Sol-Gel Derived Hybrid Organic-Inorganic Nanocomposites. Journal of Sol-Gel Science and Technology*, **19**:31–38, (2000).

[33] J. Scarminio, A. Lourenco, and A. Gorenstein. *Electrochromism and photochromism in amorphous molybdenum oxide films. Thin Solid Films*, **302**:66–70, (1997).

[34] P.F. Carcia and E.M. McCarron III. *Synthesis and properties of thin film polymorphs of molybdenum trioxide. Thin Solid Films*, **155**:53–63, (1987).

[35] A.F. Jankowski and L.R. Schrawyer. *Reactive sputtering of molybdenum. Thin Solid Films*, **193**:61–71, (1990).

[36] M.I. Yanovskaya, I.E. Obvintseva, V.G. Kessler, B.Sh. Galyamov, S.I. Kucheiko, R.R. Shifrina, and N.Ya. Turova. *Hydrolysis of molybdenum and*

tungsten alkoxides: sols, powders and films. J. Non-Cryst. Solids, **124**:155–166, (1990).

[37] Y. Zhang, S. Kuai, Z. Wang, and X. Hu. *Preparation and electrochromic properties of Li-doped MoO_3 films fabricated by the peroxo sol-gel process. Applied Surface Science*, **165**:56–59, (2000).

[38] A. Bouzidi, N. Benramdane, H. Tabet-Derraz, C. Mathieu, B. Khelifa, and R. Desfeux. *Effect of substrate temperature on the structural and optical properties of MoO_3 thin films prepared by spray pyrolysis technique. Materials Science and Engineering B*, **97**:5–8, (2003).

[39] W.-Q. Yang, Z.-R. Wei, X.-H. Zhu, and D.-Y. Yang. *Strong influence of substrate temperature on the growth of nanocrystalline MoO_3 thin films. Physics Letters A*, **373**:3965–3968, (2009).

[40] G.A. Niklasson and C.G. Granqvist. *Electrochromics for smart windows: thin films of tungsten oxide and nickel oxide, and devices based on these. J. Mater. Chem.*, **17**:127–56, (2007).

[41] C.G. Granqvist. *Electrochromic materials: Out of a niche. Nature Mater.*, **5**:89–90, (2006).

[42] P.M.S. Monk, R.J. Mortimer, and D.R. Rosseinsky. *Electrochromism and electrochromic Devices*. Cambridge University Press, 2007.

[43] E. Ozkan, S.-H. Lee, C.E. Tracy, J.R. Pitts, and S.K. Deb. *Comparison of electrochromic amorphous and crystalline tungsten oxide films. Sol. Energy Mater. Sol. Cells*, **79**:439, (2003).

[44] S.-H. Lee, M.J. Seong, H.M. Cheong, E. Ozkan, E.C. Tracy, and S.K. Deb. *Effect of crystallinity on electrochromic mechanism of $Li_x WO_3$ thin films. Solid State Ionics*, **156**:447–452, (2003).

[45] L. Berggren and G.A. Niklasson. *Influence of sputtering conditions on the solar and luminous optical properties of amorphous Li_xWO_y thin films. Sol. Energy Mater. Sol. Cells*, **85**:573, (2005).

[46] J. Scarminio. *Stress in photochromic and electrochromic effects on tungsten oxide film. Sol. Energy Mater. Sol. Cells*, **79**:357–368, (2003).

[47] R.-T. Wen, C.G. Granqvist, and G.A. Niklasson. *Eliminating degradation and uncovering ion-trapping dynamics in electrochromic WO_3 thin films. Nature Mater.*, **14**:996–1001, (2015).

[48] U.O. Krasovec, A.S. Vuk, and B. Orel. *Comparative studies of all sol-gel electrochromic windows employing various counter-electrodes. Sol. Energy Mater. Sol. Cells*, **73**:2137, (2002).

[49] G. Leftheriotis, S. Papaefthimiou, and P. Yanoulis. *The effect of water on the electrochromic properties of WO_3 films prepared by vacuum and chemical methods. Sol. Energy Mater. Sol. Cells*, **83**:115, (2004).

[50] E. Avenda no, H. Rensmo, A. Azens, A. Sandell, G. de M. Azevedo, H. Siegbahn, G.A. Niklasson, and C.G. Granqvist. *Coloration mechanism in proton-intercalated electrochromic hydrated NiO_y and $Ni_{1x}V_xO_y$ thin films. J. Electrochem. Soc.*, **156**:P132–P138, (2009).

[51] R.-T. Wen, C.G. Granqvist, and G.A. Niklasson. *Anodic electrochromism for energy-efficient windows: Cation/Anion-Based surface processes and effects of crystal facets in Nickel Oxide thin films. Adv. Funct. Mater.*, **25**:3359–3370, (2015).

[52] R.-T. Wen, C.G. Granqvist, and G.A. Niklasson. *Cyclic voltammetry on sputter-deposited films of electrochromic Ni oxide: Power-law decay of the charge density exchange. Appl. Phys. Lett.*, **105**:163502, (2014).

[53] J.S.E.M. Svensson and C.G. Granqvist. *Electrochromic hydrated nickel oxide coatings for energy efficient windows: optical properties and coloration mechanism. Appl. Phys. Lett.*, **49**:1566–1568, (1986).

[54] R.-T. Wen, C.G. Granqvist, and G.A. Niklasson. *Anodic Electrochromic Nickel Oxide Thin Films: Decay of Charge Density upon Extensive Electrochemical Cycling. ChemElectroChem*, **3**:266–275, (2016).

[55] S.V. Green, M. Watanabe, N. Oka, G.A. Niklasson, C.G. Granqvist, and Y. Shigesato. *Electrochromic properties of nickel oxide based thin films sputter deposited in the presence of water vapor. Thin Solid Films*, **520**:3839–3842, (2012).

[56] S.V. Green, A. Kuzmin, J. Purans, C.G. Granqvist, and G.A. Niklasson. *Structure and composition of sputter-deposited nickel-tungsten oxide films. Thin Solid Films*, **519**:2062–66, (2011).

[57] S.V. Green, E. Pehlivan, C.G. Granqvist, and G.A. Niklasson. *Electrochromism in sputter deposited nickel-containing tungsten oxide films. Sol. Energy Mater. Sol. Cells*, **99**:339–44, (2012).

[58] S. Hashimoto and H. Matsuoka. *Lifetime of electrochromism of amorphous WO_3-TiO_2 thin films. J. Electrochem. Soc.*, **138**:2403–2408, (1991).

[59] S. Hashimoto and H. Matsuoka. *Prolonged lifetime of electrochromism of amorphous WO_3-TiO_2 thin films. Surf. Interface Anal.*, **19**:464–468, (1992).

[60] J. Göttsche, A. Hinch, and V. Wittwer. *Electrochromic mixed WO_3-TiO_2 thin films produced by sputtering and the sol-gel technique: A comparison. Sol. Energy Mater.Sol.Cells*, **31**:415–428, (1993).

[61] F.S. Manciu, Y. Yun, W.G. Durrer, J. Howard, U. Schmidt, and C.V. Ramana. *Comparative microscopic and spectroscopic analysis of temperature-dependent*

growth of WO_3 and $W_{0.95}Ti_{0.05}O_3$ thin films. J. Mater. Sci., **47**:6593–6600, (2012).

[62] C.V. Ramana, G. Baghmar, E.J. Rubio, and M.J. Hernandez. *Optical constants of amorphous, transparent titanium-doped tungsten oxide thin films. ACS Appl. Mater. Interfaces*, **5**:4659–4666, (2013).

[63] P.K. Biswas, N.C. Pramanik, M.K. Mahapatra, D. Ganguli, and J. Livage. *Optical and electrochromic properties of sol-gel WO_3 films on conducting glass. Materials Letters*, **57**:4429–4432, (2003).

[64] F. Lin, J. Cheng, C. Engtrakul, A.C. Dillon, D. Nordlund, R.G. Moore, T.-C. Weng, S.K.R. Williams, and R.M. Richards. *In situ crystallization of high performing WO_3-based electrochromic materials and the importance for durability and switching kinetics. J. Mater. Chem.*, **22**:1681716823, (2012).

[65] S. Sallard, T. Brezesinski, and B.M. Smarsly. *Electrochromic stability of WO_3 thin films with nanometer-scale periodicity and varying degrees of crystallinity. J. Phys. Chem. C*, **111**:7200–7206, (2007).

[66] M.W. Barsoum. *Fundamentals of Ceramics.* McGraw-Hill, 1997.

[67] C.G. Granqvist. *Electrochromic oxides: a bandstructure approach. Solar Energy Materials & Solar Cells*, **32**:369–382, (1994).

[68] C.G. Granqvist. *Electrochromic Materials: Microstructure, Electronic Bands and Optical Properties. Appl. Phys. A*, **57**:3–12, (1993).

[69] L. Kihlborg. *Studies on molybdenum oxide. Acta Chem. Scan.*, **13**:954–962, (1959).

[70] D.B. Migas, V.L. Shaposhnikov, and V.E. Borisenko. *Tungsten oxides. II. The metallic nature of Magnéli phases. Journal of Applied Physics*, **108**:093714, (2010).

[71] M.R. Tubbs. *MoO_3 Layers-Optical properties, colour centers and holographic recording. Phys. Status Solidi A*, **21**:253–260c, (1974).

[72] P. Gérard, A. Deneuville, and R. Courths. *Characterization of a-WO_3 thin films before and after colouration. Thin Solid Films*, **71**:221–236, (1980).

[73] A. Smakula. *über erregung und entfarbung lichtelektrisch leitender alkali-halogenide. Zeitschrift für Physik*, **59**:603–614, (1930).

[74] D.Y. Smith and G. Graham. *Oscillator strengths of defects in insulators: The generalization of Smakula's equation. Journal de Physique*, **41**:C6–80, (1980).

[75] D.L. Dexter. *Absorption of light by stoms in solids. Physical Review*, **101**:48–55, (1956).

[76] L. Melvin. *The Franck-Condon principle and its application to crystals. The Journal of chemical Physics*, **20**:1752, (1952).

[77] C. Kittel. *Introduction to Solid State Physics.* John Wiley & Sons, seventh edition edition, 1996.

[78] N.W. Ashcroft and N.D. Mermin. *Solid State Physics.* Books/Cole, 1976.

[79] J. Patterson and B. Bailey. *Solid State Physics Introduction to the theory.* Springer, 2010.

[80] A.I. Gavrilyuk. *Photochromism in WO_3 thin films. Electrochimica Acta*, **44**:3027–3037, (1999).

[81] U. Tritthart, W. Gey, and A. Gavrilyuk. *Nature of the optical absorption band in amorphous $H_x WO_3$ thin films. Electrochimica Acta*, **44**:3039–3049, (1999).

[82] A. Gavrilyuk, U. Tritthart, and W. Gey. *The nature of the photochromism arising in the nanosized MoO_3 films. Solar Energy Materials & Solar Cells*, **95**:1846–1852, (2011).

[83] B.W. Faughnan, R.S. Crandall, and P.M. Heyman. *Device Reseach Conference Session IVB Display and Printing IVB-1 The dynamics of coloring and bleaching of WO_3 amorphous electrochomic films. IEEE Transactions on electron devices*, pages 1063–1064, (1975).

[84] C.R. Ottermann, A. Temmink, and K. Bange. *Comparison of tungsten and nickel oxide electrochromism in single films and in all solid state devices. Thin Sold Films*, (1990).

[85] G.C. Allen and N.S. Hush. *Intervalence Transfer Absortion, Part 1: Qualitative Evidence for Itervalence-Transfer Absortion. Inorganic Systems in Solution and in the Solid State. Progress in Inorganic Chemistry, Interscience*, pages 357–389, (1967).

[86] N.S. Hush. *Intervalence Transfer Absortion, Part 2: Theoretical Considerations and Spectroscopic Data. Inorganic Systems in Solution and in the Solid State. Progress in Inorganic Chemistry, Interscience*, pages 391–444, (1967).

[87] W.C. Dautremont-Smith. *Tansition metal oxide electrochromic materials and displays: a review Part 1: oxides with cathodic coloration. Displays*, pages 3–22, (1982).

[88] J.V. Gabrusenoks, P.D. Cikmach, A.R. Lusis, J.J. Kleperis, and G. M. Ramans. *Electrochromic color centres in amorphous tungsten trioxide thin films. Solid State Ionics*, pages 25–30, (1984).

[89] T. He, Y. Ma, Y. Cao, P. Jiang, X. Zhang, W. Yang, and J. Yao. *Enhancement effect of gold nanoparticles on the UV-Light photochromism of molybdenum trioxide thin films. Langmuir*, pages 8024–8027, (2001).

[90] J.W. Rabalais, R.J. Colton, and A.M. Guzman. *Trapped electrons in substoichiometric MoO_3 observed by X-ray electron spectroscopy. Chemical Physics Letters*, pages 131–133, (1974).

[91] T.H. Fleisch and G.J. Mains. *An XPS study of the UV reduction and photochromism of MoO_3 and WO_3. The Journal of chemical physics*, pages 780–786, (1982).

[92] A.S. Alexandrov (editor). *Polarons in Advanced Materials*. Springer, 2007.

[93] H.J. Lipkin. *Quantum Mechanics, New Approaches to Selected Topics*. North-Holland, 1973.

[94] O.F. Schirmer, K.W. Blazey, W. Berlinger, and R. Diehl. *ESR and optical absorption of bound-small polarons in $YAlO_3$. Physical Review B*, **11**:4201–4211, (1975).

[95] D.M. Mattox. *The fundations of vacuum coating technology*. Noyes Publications, 2003.

[96] J.L. Vossen and J.J. Cuomo. *Thin Film Processes, Part II-1 Glow Discharge Sputter Deposition*. Academic Press, 1978.

[97] J. Musil. *Physical and mechanical properties of hard nanocomposite films prepared by reactive magnetron sputtering: Nanostructure science and technology*. Springer, 2006.

[98] H.H. Perkampus. *UV-VIS Spectroscopy and its applications*. Springer-Verlag, 1992.

[99] J. Sólyom. *Fundamentals of the physics of solids, Volume-1 Structure and Dynamics*. Springer-Verlag, 2007.

[100] E.C. Le Ru and P.G. Etchegoin. *Principles of surface-enhanced Raman spectroscopy and related plasmonic effects*. Elsevier, 2009.

[101] J.R. Ferraro, K. Nakamoto, and C.W. Brown. *Introductory Raman Spectroscopy*. Academic Press, 2003.

[102] G. Gauglitz and T. Vo-Dinh. *Handbook of Spectroscopy*. Wiley-VCH, 2003.

[103] E. Smith and G. Dent. *Modern Raman spectroscopy; A Practical Approach*. Wiley, 2008.

[104] Omega Optical. `http://www.omegafilters.com/applications/raman-spectroscopy/`, 2017.

[105] G. Busch and H. Schade. *Lectures on solid state physics*. Pergamon Press, 1976.

[106] J.J. Quinn and Y. Kyung-Soo. *Solid State Physics Principles and Modern Applications*. Springer-Verlag, 2009.

[107] J.P. McKelvey. *Física del estado sólido y de semiconductores*. Limusa, 1980.

[108] G. Grosso and G.P. Parravicini. *Solid State Physics*. Academic Press, 2003.

[109] J.R. Wormald. *Métodos de difracción*. Reverté, 1979.

[110] G.V. Nin and O. Echeverría. *Introducción a la microscopía electrónica aplicada a las ciencias biológicas*. Fondo de cultura económica, 2000.

[111] Y. Leng. *Materials Characterization: Introduction to microscopic and spectroscopic method*. Wiley-VCH, 2013.

[112] P. Van Der Heide. *X-ray photoelectron spectroscopy: An introduction to principles and practices*. Wiley, 2012.

[113] E. McCafferty. *Introduction to corrosion science*. Springer, 2010.

[114] B. Fultz and J. Howe. *Transmission Electron Microscopy and Diffractometry of Materials*. Springer, 2008.

[115] L. Reimer and H. Kohl. *Transmission Electron Microscopy: Physics of Image Formation*. Springer, 2008.

[116] R.F. Egerton. *Physical principles of electron microscopy: An introduction to TEM, SEM and AEM*. Springer, 2005.

[117] R. Hellborg, H. J. Whitlow, and Y. Zhang. *Ion Beams in Nanoscience and Technology*. Springer-Verlag, 2009.

[118] D. Brune, R. Hellborg, H.J. Whitlow, and O. Hunderi. *Surface Characterization*. Wiley-VCH, 1997.

[119] B. Schmidt and K. Wetzig. *Ion Beams in Materials Processing and Analysis*. Springer-Verlag, 2013.

[120] M . Mayer. *SIMNRA, A Simulation Program for the Analysis of NRA, RBS and ERDA. AIP Conference Proceedings*, **475**:541–44, (1999).

[121] S. Green. *Electrochromic Nickel-Tungsten Oxides: Optical, Electrochemical and Structural Characterization of Sputter-deposited Thin Films in the Whole Composition Range, Ph.D. Thesis*. Uppsala Universitet, 2012.

[122] S.V. Green, A. Kuzmin, J. Purans, C.G. Granqvist, and G.A. Niklasson. *AIP Conference Proceedings*,structure and composition of sputter-deposited nickel-tungsten oxide films. *Thin Solid Films*, **519**:2062–2066, (2011).

[123] M.A. Arvizu, S.A. Tomás, M. Morales-Luna, J. Santoyo-Salazar, J.O. García-Torija, and O. Zelaya-Angel. *Effect of a ZnSe Layer on the Thermochromic Properties of MoO_3 Thin Films. Int. J. Thermophys.*, **33**:20352040, (2012).

[124] Q.P. Ding, H.B. Huang, J.H. Duan, J.F. Gong, S.G. Yang, X.N. Zhao, and Y.W. Du. *Molybdenum trioxide nanostructures prepared by thermal oxidization of molybdenum. Journal of Crystal Growth*, **294**:304308, (2006).

[125] E.M. McCarron III and J.C. Calabrese. *The growth and single crystal structure of a high pressure phase of molybdenum trioxide: MoO_3-II. Journal of Solid State Chemistry*, **91**:121–125, (1991).

[126] M.F. Al-Kuhaili, S.M.A. Durrani, I.A. Bakhtiari, and A.M. Al-Shukri. *Optical constants and thermocoloration of pulsed laser deposited molybdenum oxide thin films. Optics Communications*, **283**:2857–2862, (2010).

[127] S.-H. Lee, M.J. Seong, C.E. Tracy, A. Mascarenhas, J.R. Pitts, and S.K. Deb. *Raman spectroscopic studies of electrochromic a-MoO_3 thin films. Solid State Ionics*, **147**:129–133, (2002).

[128] I.R. Beattie and T.R. Gilson. *Oxide phonon spectra. J. Chem. Soc. (A)*, **147**:2322–2327, (1969).

[129] K. Ajito, L.A. Nagahara, D.A. Tryk, K. Hashimoto, and A. Fujishima. *Study of the photochromic properties of amorphous MoO_3 films using Raman microscopy. J. Phys. Chem.*, **99**:16383–16388, (1995).

[130] C. Julien, A. Khelfa, O.M. Hussain, and G.A. Nazri. *Synthesis and characterization of flash-evaporated MoO_3 thin films. Journal of Crystal Growth*, **156**:235–244, (1995).

[131] E. Haro-Poniatowski, M. Jouanne, J.F. Morhange, C. Julien, R. Diamant, M. Fernandez-Guasti, G. A. Fuentes, and J.C. Alonso. *Micro-Raman characterization of WO_3 and MoO_3 thin films obtained by pulsed laser irradiation. Applied Surface Science*, **127-129**:674–678, (1998).

[132] P.A. Spevack and N.S. McIntyre. *Thermal reduction of molybdenum trioxide. J. Phys. Chem.*, **96**:9029–9035, (1992).

[133] D.D. Yao, J.Z. Ou, K. Latham, S. Zhuiykov, A.P. O'Mullane, and K. Kalantar-Zadeh. *Electrodeposited α- and β-Phase MoO_3 Films and Investigation of Their Gasochromic Properties. Cryst. Growth Des.*, **12**:1865–1870, (2012).

[134] Y. Hiruta, M. Kitao, and S. Yamada. *Absorption bands of electrochemically-colored films of WO_3, MoO_3, and $Mo_cW_{1-c}O_3$. Japanese Journal of Applied Physics*, **23**:1624–1627, (1984).

[135] M. Dieterle, G. Weinberg, and G. Mestl. *Raman spectroscopy of molybdenum oxides Part I. Structural characterization of oxygen defects in MoO_{3-x} by*

DR UV/VIS, Raman spectroscopy and X-ray diffraction. Phys. Chem. Chem. Phys., **4**:812–821, (2002).

[136] M. Rouhani, Y.L. Foo, J. Hobley, J. Pan, G.S. Subramanian, X. Yu, A. Rusydi, and S. Gorelik. *Photochromism of amorphous molybdenum oxide films with different initial Mo^{5+} relative concentrations. Applied Surface Science*, **273**:150–158, (2013).

[137] S.S. Tarsame and G.B. Reddy. *Optical, structural and photoelectron spectroscopic studies on amorphous and crystalline molybdenum oxide thin films. Solar Energy Materials & Solar Cells*, **82**:375–386, (2004).

[138] F. Werfel and E. Minni. *Photoemission study of the electronic structure of Mo and Mo oxides. J. Phys. C: Solid State Phys*, **16**:6091–6100, (1983).

[139] J. Baltrusaitis, B. Mendoza-Sanchez, V. Fernandez, R. Veenstra, N. Dukstiene, A. Roberts, and N. Fairley. *Generalized molybdenum oxide surface chemical state XPS determination via informed amorphous sample model. Applied Surface Science*, **326**:151–161, (2015).

[140] D.O. Scanlon, G.W. Watson, D.J. Payne, G.R. Atkinson, R.G. Egdell, and D.S.L. Law. *Theoretical and Experimental Study of the Electronic Structures of MoO_3 and MoO_2. J. Phys. Chem. C*, **114**:4636–4645, (2010).

[141] M. Vasilopoulou, A.M. Douvas, D.G. Georgiadou, L.C. Palilis, S. Kennou, L. Sygellou, A. Soultati, I. Kostis, G. Papadimitropoulos, D. Davazoglou, and P. Argitis. *The influence of hydrogenation and oxygen vacancies on molybdenum oxides work function and gap states for application in organic optoelectronics. J. American Chemical Society*, **134**:16178–16187, (2012).

[142] J. Meyer and A. Kahn. *Electronic structure of molybdenum-oxide films and associated charge injection mechanisms in organic devices. Journal of Photonic for Energy*, **1**:011109–1, (2011).